UNIVERSITÀ DEGLI STUDI DI BARI ALDO MORO

DIPARTIMENTO INTERATENEO DI FISICA "M. MERLIN"

Dottorato di ricerca in FISICA – Ciclo XXXI

Settore Scientifico Disciplinare: FIS/01

Innovative quartz-enhanced photoacoustic sensors for trace gas detection

Dottorando:

Marilena Giglio

Supervisore:

Prof. Vincenzo Spagnolo

Coordinatore:

Ch.mo Prof. Giuseppe Iaselli

ESAME FINALE 2018

Contents

Introduction

Trace gas detection finds application in a wide variety of fields: concentration levels monitoring of gas species like ammonia, nitric oxide, volatile organic compounds (VOCs), ethylene, and acetone in human breath to assist early detection of several diseases, like asthma, cancer and diabetes. Likewise, greenhouse and pollutants gases detection is fundamental for environmental monitoring, while hydrocarbons detection is employed to predict production outputs and estimate reserves in petrochemical industry. Compared to other gas sensing techniques, like gas chromatography, gas spectrometry, electrochemical sensing, which can be costly, bulky, slow time responsive or can suffer from hysteresis, laser absorption spectroscopy (LAS) techniques are cheaper and capable of long-term stability, high sensitivity, real-time measurements. LAS has been widely demonstrated in the mid-infrared (mid-IR) spectral range, containing absorption lines and bands related to molecular ro-vibrational transitions of several gas species. Photoacoustic spectroscopy (PAS) has been proved as one of the most robust and sensitive trace gas optical detection techniques, capable of performing measurements at sub-parts-per-trillion (ppt) concentration levels. PAS is based on the detection of sound waves generated by gas absorption of modulated optical radiation, detected by a microphone. In 2002, an alternative approach was proposed, employing a high-quality factor quartz tuning fork (QTF) in microphone's stead, named quartz-enhanced photoacoustic spectroscopy (QEPAS). The employment of a QTF allowed a sensible reduction of the detection module volume and immunity to environmental noise, while guaranteeing ppt detection sensitivities. For these reasons, in this thesis QEPAS was selected as the winning spectroscopic technique to detect trace gases with high sensitivity and selectivity, implementing a QTF acoustically coupled with micro-resonator (mR) tubes to enhance the signal-to-noise ratio.

In the QEPAS technique, it is critical that the laser beam entering the mR tubes does not illuminate the tubes walls and the QTF prongs, to avoid the generation of photo-thermal effects and, consequently, the rising of a fringe-like non-zero background, which strongly limits the QEPAS detection sensitivity. The beam profiles of commercially available laser sources often exhibit a multi-mode elliptical not Gaussian-like optical power distribution. The coupling with hollow-core waveguides (HCWs), properly

designed for beam delivery in mid-IR spectral range, is here proposed to spatially clean-up the beam profiles of interband cascade lasers and quantum cascade lasers. Another solution beneficial to relax alignment tolerances, without compromising detection sensitivity, is the use of custom QTFs. Since its first demonstration, QEPAS employed the commercial QTFs usually implemented in wristwatches and clocks, designed to maintain a selected resonance frequency (typically 2^{15} Hz) in a wide temperature range. A theoretical model has been developed to analyse the influence of QTF dimensions on the main physical parameters controlling its sensing performance, namely the resonance frequency, the quality factor and the electrical resistance. Based on this study, new QTFs designs have been modelled and realized, allowing, for example, the extension of QEPAS to the THz spectral range.

So far, the fine tunability of interband cascade lasers and quantum cascade lasers has been exploited in QEPAS sensors to detect absorption lines of a wide variety of gases. However, many harmful and greenhouse gases, as well as VOCs and explosives, belong to the class of broadband absorber gases, characterized by merged absorption lines or bands spreading over several tens of cm^{-1}. In this thesis two examples of QEPAS-based sensors for broadband absorbers detection are presented, exploiting the tunability range of an interband cascade laser or of a monolithic array of 32 distributed feedback-QCLs, respectively.

This thesis is organized as follows:

Chapter 1: The basic principles of photoacoustic spectroscopy and quartz-enhanced photoacoustic spectroscopy are described, as well as the laser modulation and signal detection approaches usually employed. The acoustic coupling of a quartz tuning fork with micro-resonator tubes is also dealt with, resulting in a spectrophone enhancing the QEPAS signal-to-noise ratio.

Chapter 2: A theoretical model is developed to predict the best coupling conditions of cylindrical or tapered hollow-core waveguides (HCWs) with laser sources operating in the mid-infrared spectral range to provide single-mode low losses output. The model has been experimentally validated by coupling both cylindrical and tapered HCWs with interband cascade lasers and quantum cascade lasers with emission wavelengths spanning from 3.5 μm to 7.8 μm. Finally, an example of application of an HCW in a

QEPAS-based sensor is shown, demonstrating that the beam filtering provided by an HCW enables high-performance leaks detection.

Chapter 3: The dependence of the QTFs resonance frequency and quality factor on the prongs geometrical parameters is studied. Based on the developed model, custom QTFs optimized for QEPAS sensing have been designed, realized and tested. The achieved optimized sensing performances of custom QTFs are employed to realize QEPAS-based sensors detecting methanol in THz spectral range and ethylene in mid-infrared spectral range, exploiting the QTFs fundamental or first overtone flexural mode.

Chapter 4: Many harmful and greenhouse gases can exhibit unresolved absorption bands over spectral ranges as wide as 150 cm^{-1}. A single ICL is employed as light source in a QEPAS-based sensor for methane, ethane and propane detection in a narrow spectral range centred at 2989 cm^{-1}, while a monolithic array of 32 distributed feedback QCLs is used to detect methane and nitrous oxide in 1190-1340 cm^{-1} spectral range.

Appendix: Allan variance analysis allows the determination of how long optical sensor signals can be averaged in order to increase the detection sensitivity, before noise sources begin to dominate. A LabView-based code implemented to perform the Allan-Werle variance analysis of an acquired QEPAS signal and predict the achievable minimum detection limit is described.

Chapter 1
Fundamentals and detection configurations of Quartz-Enhanced Photoacoustic Spectroscopy

One of the most robust and sensitive trace-gas optical detection techniques is photoacoustic spectroscopy (PAS), which is capable of extremely high detection sensitivities with a compact and relatively low-cost absorption detection module [1]. In 2002 A. Kosterev and F. K. Tittel developed a novel technique based on PAS, the so-called quartz-enhanced photoacoustic spectroscopy (QEPAS) [2]. In less than a decade, QEPAS has been used to obtain spectra of many gas species. Mid-, near- and far-infrared lasers, as well as optical parametric oscillators have been employed as radiation sources in QEPAS systems described in numerous publications [3]. Compared to PAS, QEPAS employs a more compact absorption detection module and record sensitivities as high as part-per-trillion concentration in volume have been achieved [4].

1.1 Basic principles of photoacoustic spectroscopy

The photoacoustic (PA) effect was discovered in 1880 by A. G. Bell while working on the development of the Photophone [5] and consists in the generation of acoustic waves due to the absorption of modulated light in a gaseous, liquid or solid sample. A typical gas sensing photoacoustic spectroscopy setup is composed of a light source, a cell containing the target gas, a mechanical resonator acting as a microphone and the readout mechanism. Therefore, PAS is based on an optical absorption process, such as other optical detection techniques, but differs in the physical phenomenon used for the detection of the absorption signal.

A schematic representation of the photoacoustic signal generation in a gas sample is shown in Fig. 1.1.

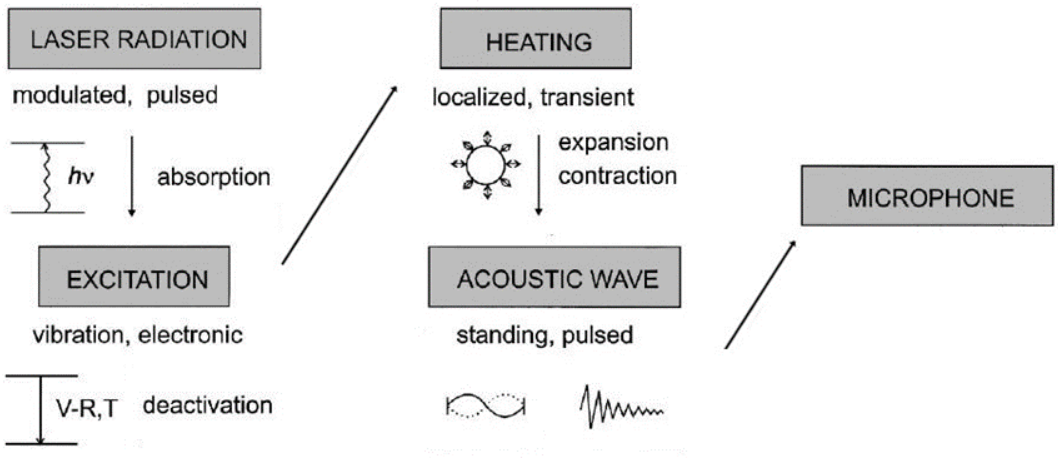

Figure 1.1 Schematic of the physical processes generating photoacoustic effect

When light at a specific wavelength is absorbed by the gas sample, the excited molecules will subsequently relax to the ground state either through emission of photons or by means of non-radiative processes. The latter produce localized heating in the gas, which in turn results in an increase of the local pressure. If the incident light intensity is modulated, the generation of thermal energy in the sample will also be periodic and a pressure wave, i.e., a sound wave, will be produced having the same frequency of the light modulation. The key advantage of this technique is that no optical detector is required and the resulting sound waves can be detected by a commercial hearing aid microphone.

The PAS signal can be amplified by tuning the modulation frequency to one of the acoustic resonances of the gas sample cell. The photoacoustic signal S can be expressed by:

$$S = CP_L\alpha\,, \tag{1.1}$$

where C is the instrumental constant, P_L is the laser power and α is the gas absorption coefficient, which can be expressed as the product of the cross section of the optical transition σ, the concentration of the target gas c and the total number of molecules per unit volume N_{tot}, $\alpha = \sigma\, c\, N_{tot}$. Therefore, the PAS signal is proportional to the sample concentration c. The minimum optical absorption coefficient α_{min} detectable with a PAS-based sensor is determined by the condition S = N, where N is the noise level, which is assumed to be independent of the optical excitation. Hence, the minimum detectable concentration c_{min} can be expressed by using Eq. (1.2) as:

$$c_{min} = \frac{\alpha_{min}}{N\sigma}\,. \tag{1.2}$$

The instrumental constant C in Eq. (1.1) depends on the cell size and geometry, the modulation frequency of the radiation, the efficiency of the transducer and the quality factor Q of the acoustic resonance defined by:

$$Q = \frac{f_0}{\Delta f}. \tag{1.3}$$

where f_0 and Δf are the resonance frequency and the full width at half maximum (FWHM) of the resonance profile, respectively. The quality factor Q and f_0 can be experimentally measured and their values typically fall in the ranges 40–200 and 1,000–4,000 Hz, respectively.

Continuous-wave single-mode diode lasers, optical parameter oscillators in the near-IR, and interband cascade lasers (ICLs) and quantum cascade lasers (QCLs) in the mid-IR have been successfully applied in PAS [1]. Compact photoacoustic gas sensors based on broadband IR sources have been also reported [6]. Resonant PAS cells and optical fiber amplifiers have been developed to enhance the PAS detection sensitivity [7].

PAS has been successfully applied to trace gas sensing applications, which include atmospheric chemistry, volcanic activity, agriculture, industrial processes, workplace surveillance and medical diagnostics. For instance, PAS has been used to monitor nitric oxide (NO) from vehicle exhaust emissions, which contributes to respiratory allergic diseases, inflammatory lung diseases, bronchial asthma and the depletion of ozone [8]. Other applications include detecting the intake of prohibited substances by athletes [9]. Low cost portable PAS sensors have been available on the market, examples of which include smoke detectors, toxic gas monitoring and oil sensors for monitoring hydrocarbons in water.

1.2 Quartz-Enhanced Photoacoustic Spectroscopy

The basic idea of QEPAS is to accumulate the acoustic energy in a sharply resonant acoustic transducer, avoiding the use of acoustic gas cells, thereby removing restrictions imposed on the gas cell design by the acoustic resonance conditions. A quartz tuning fork (QTF) is positioned in the acoustic near-field zone of the focused laser beam and the cell only serves to separate the target sample from the surrounding environment and fix and control its pressure. QTFs are perfect candidates to detect weak photoacoustic

excitation, since they are characterized by a sharp resonant acoustic profile. The sound wave generated between the two prongs causes an antisymmetric vibration of the prong in the QTF plane. A theoretical model describing in detail the QTF anti-symmetrical modes, in which case the two prongs oscillate along opposite directions, will be presented in Chapter 3. In Fig. 1.2(a) the first in-plane flexural antisymmetric mode, the so-called fundamental mode, caused by a sound wave located between the two QTF prongs is schematically represented. This vibration mode is piezoelectrically active and thus electrical charges are generated, proportional to the sound wave intensity.

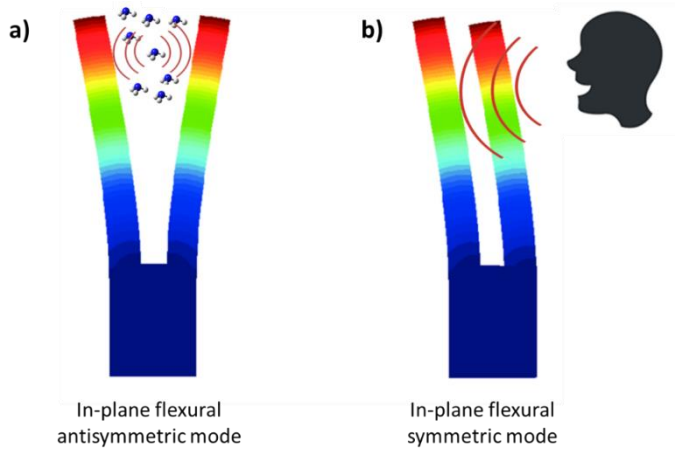

Figure 1.2 First in-plane flexural antisymmetric (a) and symmetric mode of a quartz tuning fork. The contour of the displacement field is shown in color.

When prongs of a tuning fork are in their natural oscillation motion, the stress produced along the prong can be expressed by a longitudinal tensor **σ**(x,y), where x and y identify a Cartesian plane orthogonal to the prong (aligned along the z axis). The stress induces a local polarization **p**(x,y) of quartz and charges appearing on surface can be collected by electrical contacts appropriately deposited along the QTF prongs. The polarization depends on the stress field as **p** = [**d**]**σ**, where [**d**] is the quartz piezoelectric tensor. Assuming that the QTF axes correspond to the quartz crystal axes and considering the effects of the polarization perpendicular to the tensile stress, the relation between **p** and **σ** reduces to the scalar expression $p=-d_{11}\sigma$, where d_{11} is the longitudinal piezoelectric modulus. In the elastic regime, in which there is a linear relationship between the stress and the strain field, it can be shown that σ is proportional to the second derivative of the displacement for a bent prong. By using the formulation of the displacement derived by the Euler-Bernoulli equation, the tensile stress along the prong axis is given by [10]:

$$\sigma(z) = A_n \left\{ [-cos(k_n z) - cosh(k_n z)] + \left[\frac{sen(k_n L) - senh(k_n L)}{cos(k_n L) + cosh(k_n L)} \right] [-sen(k_n z) - senh(k_n z)] \right\} \quad (1.4)$$

where the subscript n denotes different resonance mode numbers (n = 0 for the fundamental and n = 1 for the first overtone mode), A_n is the stress amplitude and L is the prong length. k_n are constant values related to the resonance mode. For the fundamental mode, k_0 = 0.11 mm^{-1}, the maximum displacement occurs at the free-end of the prong while the distribution of the strain along the prong shows the highest stress antinode at the prong-support junction. For the first overtone mode, k_1 = 0.28 mm^{-1} and two stress antinode points exist, one negative at the prong-support junction and one positive at about half of the prong length.

For gas sensing purposes, QTFs operating in the few kHz ranges can be used, since the energy transfer processes in gases occur on a μs time scale [11] and the PAS signal decreases at higher frequencies. The most convenient QTF used in electronic timing devices, such as clocks and smart-phones as frequency standards, has a resonance frequency of 32768 (2^{15}) Hz in vacuum. A 32.7 kHz-QTF was the only QTF employed in QEPAS sensor systems for the first ten years after the invention of this technique in 2002 [2].

The most important advantages of QEPAS include the following features: i) a high resonance frequency of the tuning fork (~32.7 kHz) combined with narrow bandwidth (a few hertz at atmospheric pressure) that yields a very high Q > 10000; ii) applicability over a wide range of pressure, including atmospheric pressure; iii) the capability to analyze trace-gas samples as low as few cm3 in volume; iv) a QTF is not spectrally sensitive and is practically unaffected by environmental noise. Insensitivity to environmental noise in QEPAS derives from two physical phenomena. First, a QTF is an acoustic quadrupole resonator with a Δf of a few Hz at normal pressure, so that only an insignificant number of frequency components in this narrow spectral band can produce efficient excitation of the QTF vibrations. Sound waves in air at 32 kHz have an acoustic wavelength of ~1 cm and thus, if produced by external acoustic sources, such waves tend to apply a force in the same direction on the two QTF prongs (in-plane symmetric mode, as depicted in Fig. 1.2(b)) positioned at a distance lower than 1 mm. The resulting deflection of QTF prongs is not piezoelectrically active and in contrast

with the antisymmetric vibration does not yield a detectable signal. Second, ambient noise is generally low above 10 kHz and therefore has a minimal effect on the QEPAS signal. In other words, insignificant environmental noise falls within the analyzed bandwidth. The only way to cause QTF to vibrate via the photoacoustic effect is to produce sound waves from an acoustic source located between the two QTF prongs. The standard way to realize such a condition is to focus the excitation laser beam through the gap between the prongs on the QTF crystal plane. Similar to PAS-based sensing systems, the detection sensitivities of QEPAS sensor systems are proportional to the exciting laser optical power [2,3,12]. The generation of a photoacoustic wave involves the energy transfer from internal to translational molecular degrees of freedom. If a rotational-vibrational state is excited, a collision-induced vibrational to translation (V-T) relaxation follows, with a time constant that for a particular molecule is dependent on the presence of other molecules and intermolecular interactions. When QEPAS measurements are performed at a detection frequency of ~ 32.7 kHz, the system will be more sensitive to the V-T relaxation rate compared to the conventional PAS, which is commonly performed at f_0 < 4 kHz. In case of a slow V-T relaxation with respect to the modulation frequency, the thermal waves in the gas cannot follow fast changes of the laser induced molecular vibration excitation. Thus, the generated photoacoustic wave is weaker than it would be in case of a fast V-T energy equilibration [13]. The photoacoustic signal S is related to the relaxation time as follows [14]:

$$S = \frac{Q \cdot P_L \cdot \alpha}{\sqrt{1+(2\pi f_0 \tau_{V-T})^2}}, \tag{1.5}$$

where $\tau_{V\text{-}T}$ is the V-T relaxation time. $S_0 = QP_L\alpha$ is the photoacoustic signal as it would be for an instantaneous relaxation ($\tau_{V\text{-}T}$ = 0). To enhance the energy relaxation rate, relaxation promoters (typically H_2O or SF_6) are added to the gas sample mixture [3]. Using this approach, enhancements of two orders of magnitude in the QEPAS signal have been reported [15,16]. This requires accurate measurements of the promoter concentration and additional sensor calibration.

1.2.1 On-beam QEPAS and spectrophones

The best way to excite the QTF first in-plane flexural antisymmetric mode in a QEPAS sensor is to focus the excitation laser beam on the QTF axis, i.e., through the gap between the prongs without illuminating them. This configuration is referred to as on-beam QEPAS and is schematically depicted in Fig. 1.3(a).

Significant enhancements of the QEPAS signal-to-noise ratio have been obtained as a result of the implementation of micro-resonators (mR). A mR is composed by one or two thin tubes and, in on-beam QEPAS configuration, the QTF is positioned between the tube(s) to probe the acoustic vibration excited in the gas contained inside the tubes [17]. The system composed of the QTF and the mR tube(s) is called spectrophone, as shown in Fig. 1.3(b).

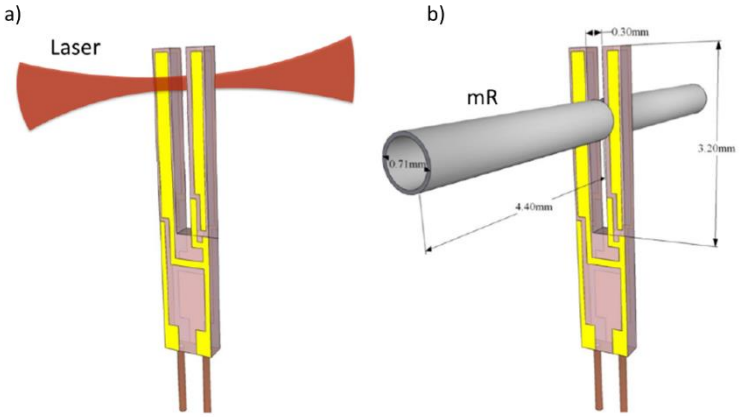

Figure 1.3 On-beam QEPAS configuration (a) and dual mR tubes spectrophone (b).

In all QEPAS sensor configurations it is critical to avoid that photoacoustic exciting radiation hits the spectrophone, otherwise an undesirable background signal that can be several times larger than the QTF thermal noise level arises, with a shifting fringe-like interference pattern shape, which limits the detection sensitivity [18].

The effect of tubes is to amplify the sound wave generated within the absorbing gas. As discussed in previous sections, a QTF is a high-Q resonator with a narrow bandwidth. A resonator tube is a low-Q acoustic element. When the air-filled mR tube and the QTF are acoustically coupled to form a spectrophone, resonance properties are affected: the resonance frequency is slightly shifted, and the quality factor is reduced, suggesting that QTF losses energy via interaction with the low-Q acoustic tube(s) [17]. A qualitative representation of the impact of tubes on the resonance frequency and quality factor of a bare QTF is given in Fig. 1.4.

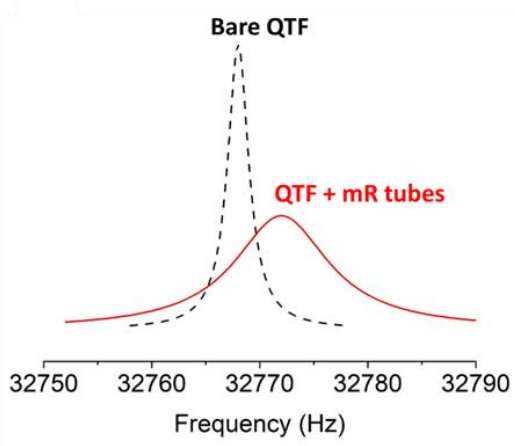

Figure 1.4 Resonance curve of a bare QTF (black dashed line) and of a QTF acoustically coupled with a pair of resonator tubes (solid red line). The impact of the resonator tubes is to shift the resonance frequency and increase the FWHM value.

The influence of the spectrophone design parameters on QEPAS performance, when a 32.7 kHz-QTF is employed, has been investigated in [3,17]. The first parameter to be optimized is the position of both tubes along the QTF axis. The acoustic source can be supposed to be located between the prongs. A simplified model is described in [3] which considers the total momentum of a pressure force acting on the two prongs of the QTF. The main assumptions are: (i) two prongs, which radiate as point sources and create divergent spherical-shaped sound waves (monopole approximation); (ii) the intensity of the pressure wave decreases as the inverse of the distance and is assumed to be constant along the thickness of each prong; (iii) the acoustic coupling between two oscillating prongs can be neglected (small oscillations approximation). The theoretical model predicts the experimentally observed optimal vertical position of the laser beam, occurring on the QTF axis, ~ 0.3 mm far from the QTF top. A more detailed and detailed theoretical model for the determination of the beam position of the laser beam that maximizes the QEPAS signal was proposed in Ref [19]. The model consists of three stages. First, an explicit formula was derived for the acoustic pressure wave by using the cylindrical symmetry of the laser beam and a narrow width of the tuning fork resonance to reduce the inhomogeneous wave equation to a Bessel equation. The model shows that the amplitude of the pressure wave is proportional to the laser modulation frequency. Then, the Euler-Bernoulli equation was employed to model the resonant vibration of the prongs of the QTF. Finally, the well-known electromechanical relationships for QTFs was used to calculate the piezoelectric current generated by the

mechanical vibration. In spite of these simplifying assumptions, an excellent agreement between theory and experiments was found and the optimal vertical position of the focused laser beam occurs on QTF axis, at y ~ 0.3 mm, equal to the result of simplified mechanical model.

When QTF is coupled with a pair of mR tubes, the geometrical parameters influencing the sensor performance are the internal diameter ID and the length l of the two tubes together with the spacing between the tube and the surface of the QTF. The length of two tubes is correlated with the sound wavelength, given by $\lambda_s = v_s/f$, where v_s is the speed of the sound (343 m/s in air). For f = 32,786, λ_s is 10.5 mm. Assuming that the left and right tubes can be considered as a single tube neglecting the gap, each tube should be cut to a $\lambda_s/4$ length (l = 2.63 mm) to form a half-wave resonator. Instead, if the gap between the tubes is big enough to make them almost independent, the tube length should be $\lambda_s/2$ (l = 5.25 mm). Experimental studies showed that l = 4.4 mm (internal diameter of 0.6 mm and external one of 0.9 mm) yields the highest SNR (~2,700), which is ~30 times higher than that of a bare 32.7 kHz-QTF at atmospheric pressure [17]. Thus, the optimal tube length falls between $\lambda_s/4$ and $\lambda_s/2$, because of the interaction of two resonator tubes and their acoustic coupling with the QTF. This observation is supported by a decrease of the Q-factor from ~14,000 (bare QTF) to 3,400. The Q-factor provides also a measure of the acoustic coupling between the QTF and tubes, since a high-Q QTF loses energy primarily via coupling to the low-Q tubes [20]. The QEPAS SNR is dependent on the tube length l and variations as small as 0.6 mm reduce this ratio to ~1,900. The choice of the optimal ID can be related to the QTF prongs spacing. When the tube diameter is larger than the prongs spacing, the gap between two tubes becomes less important and the tubes are acoustically coupled with the QTF. With an internal diameter of 0.84 mm (~3 times the prongs spacing) the optical length is 3.9 mm (SNR ~2,400), closer to a $\lambda_s/4$ length with respect to the case with l = 4.4 mm, confirming the above assumption. Consequently, a large decrease of the Q-factor was also observed (from ~3400 to ~1,700). When the tube diameter becomes comparable with the prongs spacing, the acoustic coupling is reduced and the SNR decreases. For an ID = 0.41 mm, the Q-factor increased up to ~7,500 and the SNR was reduced to ~2,400 [17]. The gap size between the QTF and the tubes is a difficult parameter to be controlled during the spectrophone assembly and has a significant effect on the final QTF performance. With a large gap, the diverging flow from the two tubes

ends cannot efficiently push against the QTF prong. Therefore, the gap should not be wider than 50 μm; when the gap is reduced from 50 to 25 μm and the SNR increases by 13% [17].

1.2.2 Off-beam QEPAS

Acoustic micro-resonator tubes are important components that are acoustically coupled with QTFs to improve the performance of QEPAS sensors. Even if on-beam alignment represented the most convenient configuration in terms of signal-to-noise enhancement for a QEPAS sensor, several configurations have been proposed in last few years. Indeed, the on-beam QEPAS configuration suffers minimal disadvantages, such as: (i) the resonant acoustic wave condition was not exactly obtained; (ii) the open-ended tubes introduce sound energy-losses; (iii) the gap between the 32.7 KHz-QTF prongs is only ~300 μm wide, which limits the inner diameter of the mR and thus the size of the laser beam that passes through the tubes. Off-beam QEPAS was first reported in [21]. A sketch of the off-beam QEPAS configuration is reported in Fig. 1.5.

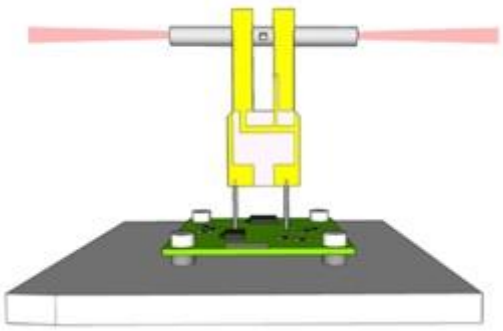

Figure 1.5 Schematic of an off-beam QEPAS configuration. A single tube with a small slit is placed alongside the QTF.

In off-beam-QEPAS, a single mR is placed alongside the QTF which senses the pressure in the micro-resonator through a small aperture. Thus, the mR tube length is determined by the first longitudinal mode of the acoustic wave at f_0. For this mode, the resonant acoustic pressure antinode is located at the center of the mR. Hence, a small slit is cut in the middle of the mR and the QTF is coupled to the mR by placing it laterally to the mR tube close to the centrally located slit. The off-beam-QEPAS configuration results in certain technical advantages as it facilitates the optical alignment and allows more flexibility in the selection of QTF dimensions. As in the on-

beam configuration, the acoustic oscillations of the gas are excited in the mR by the intensity modulation induced by the laser source. The photoacoustic signal amplitude S in the mR can be expressed as $S=C_G(f)\alpha P_L$ where $C_G(f)$ is a geometrical parameter which describes the characteristics of the mR at a given frequency f. The acoustic oscillations in the mR give rise to sound waves radiated via a slit at its center and are detected by the QTF placed outside the mR close to the slit. To maximize sound energy coupling, the distance between the mR and the QTF must be carefully chosen, since a long distance will decrease the acoustic coupling between mR and QTF, while a too short distance will dampen the QTF vibration, because of viscous drag effects. Liu et al. [21] have shown that the close proximity of the QTF to mR results in optimum acoustic coupling. At the same time, viscous drag in the air layer between the QTF and mR reduces the Q factor. Consequentially, the SNR increases by enlarging the gap up to a value of 5 μm and then decreases for wider QTF gaps. At atmospheric pressure, Q factors from 13,000 to 8,000 are achieved indicating relatively weak mR coupling to the QTF compared to the on-beam configuration, where the Q changes from 13,000 to as low as 1,380. A maximum off-beam-QEPAS signal was obtained when the mR slit was positioned between 1 and 1.5 mm below the QTF opening, as observed in the case of the on-beam QEPAS configuration. In [22], Liu et al. performed an experimental investigation of the dependence of the off-beam QEPAS signal as a function of the mR length and inner diameter. They observed that the inner diameter-to-optical length ratio linearly increases with the inner diameter. Once the inner diameter is chosen for a specific application, the optimal ratio can be determined. In addition, for efficient coupling of the acoustic signal from the mR to the QTF via a slit, it is also necessary to optimize the slit size. A small slit size limits the coupling of the acoustic energy, while a large slit size disperses the output sound energy. Varying the tube length, the resonant frequency of the mR shifts and the QTF operates as a fixed-frequency probe. By using the theory of finger-holes in woodwind instruments it is possible to find a relation between the tube length and the mR resonance. According to this theory, the tube length corresponding to f_0 = 32,750 Hz is l = 7.56 mm. Liu et al. found experimentally an optimal slit width of ~ 0.15 mm with a length of ~ 0.4 mm, for a mR with an outer diameter of 0.7 mm, an inner diameter of 0.45 mm and a length of 8 mm [22]. For these optimal conditions, a photoacoustic signal of ~15.7 times higher than that corresponding to a QEPAS system using a bare QTF is obtained. Compared to the on-beam design, the

SNR is reduced by a factor of ~1.7 at atmospheric pressure. However, off-beam-QEPAS is more flexible in terms of the QTF geometry employing custom-made QTFs, with a smaller gap between the prongs without complications related to using an optimized excitation laser pump beam. An off-beam QEPAS spectrophone is also technologically easier to assemble and align. A theoretical model of an off-beam QEPAS-based sensor was proposed in [23]. By deriving the acoustic impedances of the mR at two ends and the side slit in the middle in the model, a formula for numerically calculating the optimal mR parameters of off-beam QEPAS-based sensor was obtained. The model was used to calculate the optimal mR length and inner diameter with respect to the resonance frequency of the QTF as well as the acoustic velocity inside mR, finding a close match with experimental data. A low-cost UV-LED has been employed as the light source in an off-beam QEPAS setup for ozone detection and a detection limit of 1.27 ppm corresponding to a NNEA parameter of $3.02 \cdot 10^{-8}$ $cm^{-1}W/Hz^{-1/2}$ was achieved [24].

1.3 Laser modulation and QEPAS signal detection techniques

The combination of single mode emission and fast tunability makes semiconductor lasers extremely attractive for sensitive trace-gas detection. When these features are combined with modulation techniques, high detection sensitivities can be achieved [25,26].

Two approaches can be employed to modulate the target gas absorption and generate a sound wave with a frequency matching the natural frequency of the resonator. In wavelength modulation (WM) approach, the laser injection current is modulated by an external dither, typically a sine waveform, in order to modulate the emission wavelength of the laser. In amplitude modulation (AM) approach, the laser is switched on and off at the resonator natural frequency. Such a condition can be accomplished by setting a chopper between the laser source and the gas cell or by applying an external square waveform signal to the laser injection current.

1.3.1 Wavelength modulation and dual-frequency detection

In wavelength modulation (WM), the frequency of the laser light is modulated with a periodic function, typically a sine wave. One important advantage of WM is that only the noise centred at the detection frequency and within the detection bandwidth will affect trace-gas measurements. The interaction between the chemical species to be detected and the modulated light leads to the generation of signals at the modulation frequency and its harmonics. Each harmonic of the analytical WM signal can be detected coherently with phase-sensitive detection electronics based on a lock-in amplifier. For gas sensing techniques based on cavity-enhanced and multi-pass absorption cell, the choice of modulation frequency is often limited by the detector bandwidth. The detection band should be high enough in order to limit *1/f* laser noise. However, exceeding 100 kHz is not convenient because the noise levels off [27]. In QEPAS, the modulation frequency should match the resonance frequency of the quartz tuning fork (QTF) or its sub-harmonics. When the laser injection current $i(t)$ is modulated at an angular frequency $\omega=2\pi f$, $i(t) = i_0 + \Delta i \cdot cos\omega t$, the light intensity (or optical power) $I(t) = I_0 + \Delta I \cdot cos\omega t$ and the instantaneous laser frequency $\nu(t) = \nu_0 + \Delta\nu \cdot cos(\omega t + \psi)$ are simultaneously modulated, as schematically depicted in Fig. 1.6(a). The lock-in amplifier output records the variation of the amplitude (the envelope) of a selected harmonic of the modulation frequency. Higher harmonics are generated due to the nonlinearity in the absorption coefficient $\alpha[\nu(t)]$ at the center frequency ν_0. For $\Delta\nu$ << FWHM of the absorption profile, all harmonics can be extracted from a Taylor-series expansion of the absorption-line-shape $\alpha[\nu(t)]$ at ν_0 and the expression for the *1f*-signal I_{1f} at a frequency $f=\omega/2\pi$ becomes [3, 28-30]:

$$I_{1f} = \Delta I cos(\omega t) - \Delta I \alpha(\upsilon_0) L_p cos(\omega t) - I_0 \alpha'(\upsilon_0) \Delta\upsilon cos(\omega t + \psi) L_p \quad (1.6)$$

where L_p is the length of the optical path. The first term is the background signal, which is independent of the gas concentration and intensity I_0, but depends on how ΔI varies with Δi. The second term is an absorption-dependent contribution and the third term is the first derivative signal arising from wavelength modulation. The phase of the first derivative contribution is shifted by ψ from the second term. Thus, even for a small

amplitude and frequency modulation, the *1f*-signal profile is not a true first derivative of the line-shape but is distorted by the presence of the second term. The I_{1f} trend as a function of the laser frequency across a Lorentzian absorption line is reported in Fig. 1.6(b). The *2f*-signal I_{2f} has the form:

$$I_{2f} = -\Delta I \alpha'(v_0)\Delta v cos(\omega t)cos(\omega t + \psi)L_p + \frac{1}{4} I_0 \alpha''(v_0)\Delta v^2 cos[2(\omega t + \psi)]L_p \quad (1.7)$$

In this case, the first term is due to the residual amplitude modulation (RAM) and is proportional to the first derivative of the absorption, whereas the second term represents the second-derivative term, arising from the wavelength modulation (with a phase difference of ψ between the terms). Hence, the *2f*-signal profile is not a true second derivative of the absorption line-shape, even for a small Δv, but is distorted by a contribution originating from the RAM which unbalances the two minima (see Fig. 1.6(c)). Hence, the detection at twice the applied modulation frequency (*2f*-detection) is preferred. The acquired signal will show a background-free second harmonic derivative line-shape and the effect of RAM appears only as a distortion of the line-shape.

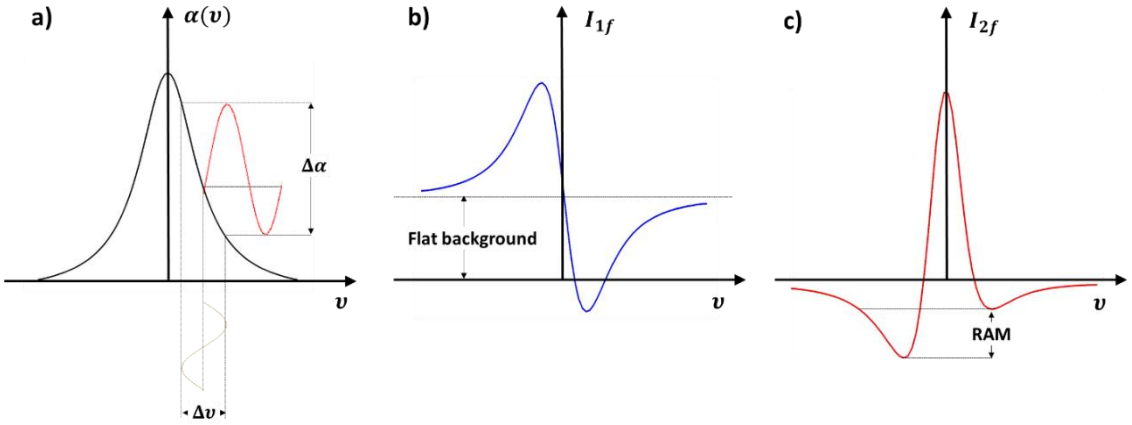

Figure 1.6 (a) Wavelength Modulation (WM) based on a Lorentzian absorption line-shape. (b) Absorption profile in WM and 1f-detection: the profile resembles the first derivative of a Lorentzian absorption line-shape with a flat background. (c) Absorption profile in WM and 2f-detection: the 2f-signal profile is not a true second derivative of a Lorentzian absorption line-shape, but it is distorted by a contribution originating from the residual amplitude modulation which unbalances the two minima.

When WM technique is combined with QEPAS, the laser light is modulated at a half of the QTF resonance frequency, $f_0/2$ and QEPAS signal is demodulated at f_0. In this case,

the QTF detects sound oscillations at the second harmonic of the modulation frequency caused by the double intersection of the absorption line by the laser line during a modulation period.

1.3.2 Amplitude modulation for broadband absorbers detection

When operating in WM, a strong background signal was observed for the *1f*-detection, originating from stray light ending up on the walls of the acoustic detection module [3]. This is confirmed by the observation that the amplitude of this offset strongly increases with a misalignment of the laser beam in lateral directions so that the beam wings touch the QTF. Instead, it was experimentally observed that the *2f*-detection is background-free. Distortions in the demodulated signal displaying an asymmetry on both sides of the spectrum around the peak can be associated to an amplitude intrinsic modulation contribution, which is introduced by current modulation. Vibrational spectra of most molecules consisting of more than five atoms are so dense that infrared absorption spectra of such polyatomic molecules consist of 100–200 cm^{-1} broad bands. Spectroscopic identification of these species requires laser excitation sources with a wide spectral coverage. However, distributed feedback (DFB) or Fabry-Perot (FP) QCLs cannot be wavelength modulated with a sufficient spectral tuning coverage for broadband absorption features. Thus, QEPAS detection of such molecules will require amplitude modulation (AM) of the laser radiation. The laser intensity is modulated at f_0 by means of square wave amplitude current modulation and the QEPAS signal is detected by a lock-in amplifier at the same f_0 frequency. Unlike WM QEPAS, AM QEPAS is not background free. Residual absorption of laser radiation by the cell windows as well as scattered radiation absorbed inside the gas cell produce a sound at the QTF resonance frequency, thus generating a coherent background. However, this background can be stable over several hours, which allows background subtraction. Typically, for every spectral point, both signal and background components normalized to the laser power are acquired. In post-processing, the in-phase and the quadrature components of the demodulated photoacoustic signal were acquired and by vector subtraction it is possible to remove the background signal [31,32].

References

[1] A. Elia, P.M. Lugarà, C. di Franco, V. Spagnolo, Photoacoustic Techniques for Trace Gas Sensing Based on Semiconductor Laser Sources, Sensors 9 (2009) 9616–9628.

[2] A.A. Kosterev, Y.A. Bakhirkin, R.F. Curl, F.K.Tittel, Quartz-enhanced photoacoustic spectroscopy, Opt. Lett. 27 (2002) 1902–1904.

[3] P. Patimisco, G. Scamarcio, F.K. Tittel, V. Spagnolo, Quartz-Enhanced Photoacoustic Spectroscopy: A Review, Sensors 14 (2014) 6165-6206.

[4] V. Spagnolo, P. Patimisco, S. Borri, G. Scamarcio, B. E. Bernacki, J. Kriesel, Part-per-trillion level SF6 detection using a quartz enhanced photoacoustic spectroscopy-based sensor with single-mode fiber-coupled quantum cascade laser excitation, Opt. Lett. 37 (2012) 4461-4463.

[5] A. Bell. On the production and reproduction of sound by light. American Journal of Science, 20 (1880) 305.

[6] J. Fonsen, V. Koskinen, K. Roth, J. Kauppinen, Dual cantilever enhanced photoacoustic detector with pulsed broadband IR-source, Vib. Spectrosc. 50 (2009) 214–217.

[7] M.E. Webber, M. Pushkarsky, C.K.N. Patel, Fiber-Amplifier-Enhanced Photoacoustic Spectroscopy with Near-Infrared Tunable Diode Lasers, Appl. Opt. 42 (2003) 2119–2126.

[8] A. Berrou, M. Raybaut, A. Godard, M. Lefebvre, High-resolution photoacoustic and direct absorption spectroscopy of main greenhouse gases by use of a pulsed entangled cavity doubly resonant OPO, App. Phys. B 98 (2010) 217–230.

[9] C. Fischer, R. Bartlome, S.W. Sigrist, The potential of mid-infrared photoacoustic spectroscopy for the detection of various doping agents used by athletes, J. Appl. Phys. B 85 (2006) 289–294.

[10] F.K. Tittel, A. Sampaolo, P. Patimisco, L. Dong, A. Geras, T. Starecki, and V. Spagnolo, Analysis of overtone flexural modes operation in quartz-enhanced photoacoustic spectroscopy, Opt. Express 24 (2016) A682-A692.

[11] W. H. Flygare, Molecular relaxation, Accounts of Chem. Res. 1 (1968) 121-127.

[12] A. A. Kosterev, F. K. Tittel, D. Serebryakov, A. L. Malinovsky, I. Morozov, Applications of Quartz Tuning Forks in Spectroscopic Gas Sensing, Rev. Sci. Instr. 76 (2005) 1-9.

[13] G. Wysocki, A. A. Kosterev, F. K. Tittel, Influence of molecular relaxation dynamics on quartz-enhanced photoacoustic detection of CO2 at $\lambda = 2$ μm. Appl. Phys. B 85 (2006) 301-306.

[14] A. A. Kosterev, Y. A. Bakhirkin, F. K. Tittel, S. McWhorter, B. Ashcraft, QEPAS methane sensor performance for humidified gases, Applied Physics B 92 (2008)103-109.

[15] V. Spagnolo, A.A. Kosterev, L. Dong, R. Lewicki, F.K. Tittel, NO trace gas sensor based on quartz-enhanced photoacoustic spectroscopy and external cavity quantum cascade laser, Appl. Phys. B 100 (2010) 125–130.

[16] L. Dong, V. Spagnolo, R. Lewicki, F.K. Tittel, Ppb-level detection of nitric oxide using an external cavity quantum cascade laser based QEPAS sensor, Optics Express 19 (2011) 24037-24045.

[17] L. Dong, A. A. Kosterev, D. Thomazy, F. K. Tittel, QEPAS spectrophones: design, optimization, and performance, Appl Phys B 100 (2010) 627-635.

[18] V. Spagnolo, P. Patimisco, S. Borri, G. Scamarcio, B.E. Bernacki, J. Kriesel, Mid-infrared fiber-coupled QCL-QEPAS sensor, Appl. Phys. B 112 (2013) 25–33.

[19] N. Petra, J. Zweck, A.A. Kosterev, S.E. Minkoff, D. Thomazy, Theoretical analysis of a quartz-enhanced photoacoustic spectroscopy sensor, Appl. Phys. B 94 (2009) 673–680.

[20] D.V. Serebryakov, I.V. Morozov, A.A. Kosterev, V.S. Letokhov, Laser microphotoacoustic sensor of ammonia traces in the atmosphere, IEEE J. Quantum Electron. 40 (2010) 167–172.

[21] K. Liu, X. Guo, H. Yi, W. Chen, W. Zhang, X. Gao, Off-beam quartz-enhanced photoacoustic spectroscopy, Opt. Lett. 34 (2009) 1594–1596.

[22] K. Liu, H. Yi, A.A. Kosterev, W. Chen, L. Dong, L. Wang, T. Tan, W. Zhang, F.K. Tittel, X. Gao, Trace gas detection based on off-beam quartz enhanced photoacoustic spectroscopy: Optimization and performance evaluation, Rev. Sci. Instrum. 81 (2010) 103103:1–103103:6.

[23] H. Yi, K. Liu, S. Sun, W. Zhang, X. Gao, Theoretical analysis of off beam quartz-enhanced photoacoustic spectroscopy sensor, Opt. Commun. 285 (2012) 5306-5312.

[24] S. Bottger, M. Koehring, U. Willer, W. Schade, Off-beam quartz-enhanced photoacoustic spectroscopy with LEDs, Appl. Phys. B 113 (2013) 227–232.

[25] J. Hodgkinson, R. P. Tatam, Optical gas sensing: a review, Meas. Sci. Technol. 24 (2013) 012004:1-012004:59.

[26] B. W. M. Moeskops, S. M. Cristescu, F. J. M. Harren, Sub-part-per-billion monitoring of nitric oxide by use of wavelength modulation spectroscopy in combination with a thermoelectrically cooled, continuous-wave quantum cascade laser, Opt. Lett. 31 (2006) 823-825.

[27] D. S. Bomse, A. C. Stanton, J. A. Silver, Frequency modulation and wavelength modulation spectroscopies: comparison of experimental methods using a lead-salt diode laser, Appl. Optics 31 (1992) 718-731.

[28] P. Patimisco, A. Sampaolo, Y. Bidaux, A. Bismuto, M. Scott, J. Jiang, A. Muller, J. Faist, F.K. Tittel, V. Spagnolo, Purely wavelength- and amplitude-modulated quartz-enhanced photoacoustic spectroscopy, Opt. Express 24 (2016) 25943-25954.

[29] P. Patimisco, S. Borri, A. Sampaolo, H.E. Beere, D.A. Ritchie, M.S. Vitiello, G. Scamarcio, V. Spagnolo, A quartz enhanced photo-acoustic gas sensor based on a custom tuning fork and a terahertz quantum cascade laser, Analyst 139 (2014) 2079-2087.

[30] Y. Bidaux, A. Bismuto, P. Patimisco, A. Sampaolo, T. Gresch, G. Strubi, S. Blaser, F.K. Tittel, V.Spagnolo, A. Muller, J. Faist, Mid infrared quantum cascade laser operating in pure amplitude modulation for background-free trace gas spectroscopy, Opt. Express 24 (2016) 26464-26471.

[31] R. Lewicki, G. Wysocki, A.A. Kosterev, F.K. Tittel, QEPAS based detection of broadband absorbing molecules using a widely tunable, cw quantum cascade laser at 8.4 μm, Opt. Express 15 (2007) 7357–7366.

[32] M.D. Wojcik, M.C. Phillips, B.D. Cannon, M.S. Taubman, Gas-phase photoacoustic sensor at 8.41 μm using quartz tuning forks and amplitude-modulated quantum cascade lasers, Appl. Phys. B 85 (2006) 307–313.

Chapter 2
Hollow-Core waveguides for single-mode low-losses mid-infrared delivery

Hollow-core waveguides (HCWs) are optical fibers which guide light through a low-index core (air) surrounded by high-index cladding layers. HCWs were implemented in gas spectroscopic sensor systems to improve the spatial quality of laser beams, that can affect the ultimate performance of gas sensors.

In this chapter cylindrical and tapered HCWs will be described, as well as their fabrication procedures. A theoretical model predicting both the optical coupling of HCWs with lasers emitting in the mid-infrared spectral range and the transmission losses will be presented. Low-losses and single mode delivery in the mid-infrared spectral range will be demonstrated by employing both cylindrical and tapered HCWs. Finally, an example of application of an HCW in a QEPAS-based sensor will be shown, employing an HCW with 300 μm bore diameter.

2.1 Cylindrical and tapered hollow waveguides

Hollow-core waveguides transmit light within a hollow region contained in a tube with walls composed of metallic/dielectric high-reflective layers. Typically, these types of HCWs consist of a fused silica cylindrical capillary tube of fixed bore size with a reflective silver (Ag) film deposited on the inner surface. A thin film of silver iodine (AgI) is deposited on the silver layer. The fabrication technique used to realize such a fiber and deposit high quality Ag and silver iodide AgI films on the capillary bore is known as a dynamic liquid deposition phase [1]. The fused silica capillary inner surface is synthetized to improve the quality of the silver film to be deposited and reduce the time needed for this procedure. A metallic coating is successively deposited by flowing a silver solution through the capillary. Finally, an iodine solution is pumped through the coated waveguide, which reacts with the metallic substrate, resulting in the conversion of the Ag into AgI. All the fabrication steps are performed by using a peristaltic pump and a flow rate selected to guarantee a high coating uniformity.

Fabrication steps and HCW cross section are showed in Fig. 2.1.

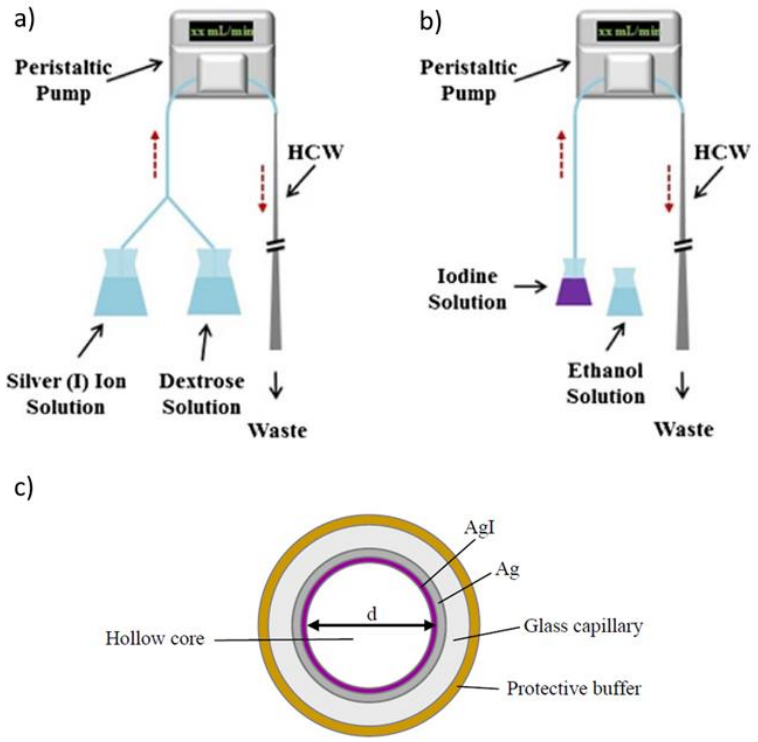

Figure 2.1 Silver film deposition (a), iodization procedures (b) and HCW circular cross section.

Recently, tapered HCWs, i.e., with the diameter linearly varying along the HCW length, have been proposed as a clever way to provide single-mode operation and facilitate the optical coupling alignment using the larger bore size as input [2,3]. Fabrication steps of tapered HCWs resemble the ones used for HCWs with constant diameter circular cross section, but some constraints on the optimum flow rate appear [3]. The dynamic bore size of the tapered samples limits the overall possible volumetric flow rate of the system to rates commonly used for smaller bore waveguides, with a necessity to flow solutions in the direction of increasing bore size so as to prevent further fluid pressure increases that would occur in the case of fluid flow along the direction of decreasing bore size. Therefore, fluid pressure buildup poses a pronounced challenge in small bore waveguides, and due to the largely length-dependent bore size profile of the tapered structures, it proves to impose an additional challenge for the tapered HGWs.

In Fig. 2.2 a comparison of the longitudinal section of a cylindrical and a tapered HCW is reported.

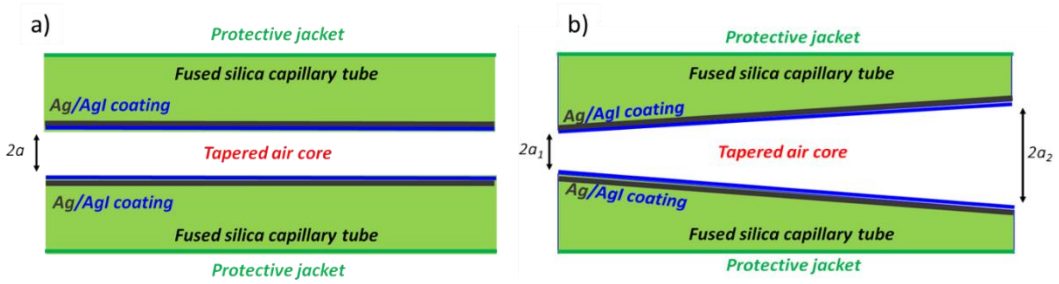

Figure 2.2 Longitudinal sectin of a cylindrical HCW (a) and a tapered HCW (b).

The hollow-core waveguides dielectric film thickness and quality determines the optical response of the fiber, leading to the design of an optimized structure for a desired spectral range of operation [1]. Propagation losses and output beam quality are mainly determined by the HCW diameter and the coupling conditions [2,3] and play a critical role in their operation [4].

As a general guide, single-mode beam profile output can be obtained when the bore diameter is up to 50 times larger than the light wavelength [5]. As an example, silica-based cylindrical HCWs with a constant bore diameter of 300 μm have been reported that can deliver optical guidance in the spectral range 7.6-11 μm with a single spatial mode at the output [6,7].

In the next section, theoretical calculations are reported on the dependence of HCWs performance, in terms of optical losses and single-mode fiber output, on the optical coupling conditions. In particular, guidelines are provided on the selection of the focal length of the coupling lens into cylindrical or tapered HCWs for lasers emitting in different spectral ranges.

2.2 Theoretical model of optical coupling with laser sources and infrared light transmission

The propagation losses and the quality of the HCW output-beam are strongly influenced by the laser-HCW optical coupling conditions. The selection of the focal length of the coupling lens is mainly determined by the laser beam diameter as well as the wavelength and the HCW bore diameter [2]. However, a single focusing lens cannot guarantee optimal coupling conditions for a wide wavelength range. When optical coupling between a collimated laser beam and the HCW is obtained by using a focusing

lens, the propagation losses and the beam quality at the waveguide exit are affected by the input laser beam quality, the size as well as the focal length of the coupling lens. The propagation of the guided light within an HCW can be treated by the ray-optics model, assuming that an optical beam can be guided by zig-zag reflections at the guiding walls. The model is based on tracking consecutive reflections of a bundle of optical rays within a cone at the waveguide entrance and propagating through the waveguide [3]. Such a model allows the determination of both the number of reflections at the waveguide wall and the angle of incidence for each reflection. However, to determine how the coupling conditions are correlated to waveguide losses and to the output-beam quality, a theoretical model based on Maxwell's equations and Gaussian optics assumptions is presented. Considering a diffraction-limited collimated Gaussian beam with a radius *w* illuminating a lens with a focal length *f* and radius of curvature *R*, the waist radius w_0 at the focal plane is given by:

$$w_0 = \frac{w}{\sqrt{1+\left(\frac{\pi w^2}{\lambda R}\right)^2}} \tag{2.1}$$

and the focal length *f* at different laser wavelengths λ is given by:

$$f = \frac{R}{1+\left(\frac{\lambda R}{\pi w^2}\right)^2}. \tag{2.2}$$

Hence, by measuring the size of the collimated beam, it is possible to estimate the waist radius at the waveguide entrance. When a Gaussian beam is focused into a hollow waveguide, the fiber HE_{nm} hybrid modes are excited. The HE_{11} mode is the lowest order mode having a circularly-symmetric, Gaussian spatial profile. The best coupling condition is obtained by maximizing the input laser mode coupling into the HE_{11} waveguide hybrid mode, providing the lowest theoretical losses and characterized by a Gaussian-like optical power distribution [8-10]. Spatial profiles of HE_{1m} waveguide modes can be approximated by the zero order Bessel functions $J(u_{1m}\, r/a)$, where *a* is the bore radius and u_{1m} is the *m-th* root of the zero-order Bessel function. If a Gaussian beam is focused to a waist w_0 at the fiber input plane, the intensity distribution is given by:

$$G(r) = G_0 e^{-\frac{r^2}{w_0^2}} \tag{2.3}$$

and the amount of the optical power coupled with the *m-th* waveguide mode can be expressed in terms of the power coupling efficiency defined as:

$$\eta_{1m} = \frac{\left|\int_0^a G(r) J\left(u_{1m}\frac{r}{a}\right) r dr\right|^2}{\int_0^a G^2(r) r dr \int_0^a J^2\left(u_{1m}\frac{r}{a}\right) r dr}. \tag{2.4}$$

Hence, the η_{1m} coefficients depend on w_0/a. The highest coupling efficiency to the HE_{11} mode is obtained for w_0/a = 0.64 [2]. Values significantly lower than 0.64 guarantee low propagation losses, but cannot ensure single-mode output conditions, since a significant fraction of the input power is coupled to higher order modes that can propagate to the waveguide exit, whereas operating at $w_0/a > 0.64$ leads to higher losses but the HCW output beam remains single-mode [2]. For a collimated beam diameter w = 2 mm, the η_{11} coupling efficiency was calculated as a function of the laser wavelength by using Eqs. (2.1)-(2.4), considering two different values for a as input bore radius, a_1= 100 μm and a_2= 130 μm. The results are shown in Fig. 2.3 considering coupling lenses with focal lengths f = 25 mm, 50 mm and 75 mm.

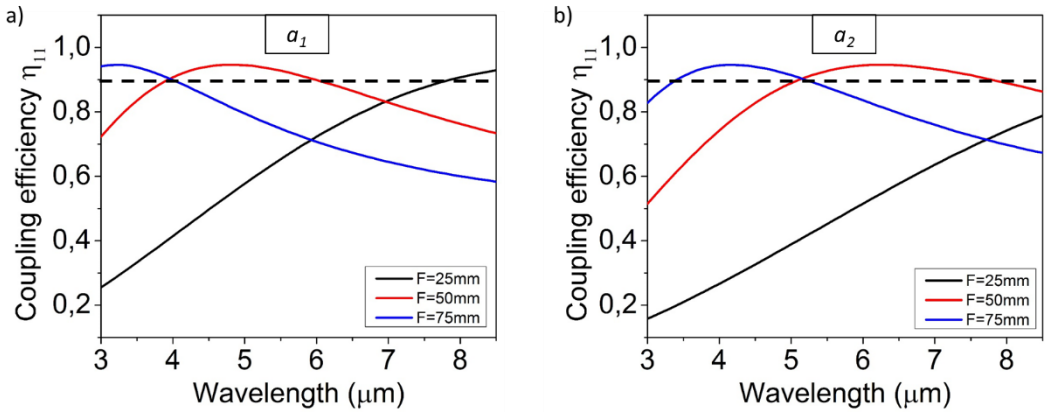

Figure 2.3 Coupling efficiency as a function of the laser wavelength, when the laser is coupled into a HCW having input bore $a=a_1$ (a) or $a=a_2$ (b) using a coupling lens with f = 25 mm (black solid line), 50 mm (red solid line) or 75 mm (blue solid line). The black dashed lines correspond to a 90% coupling efficiency.

When coupling the laser beam through a bore radius a_1, i.e. measuring 100 μm, a coupling efficiency higher than 90% (represented by a dashed line in Fig. 2.3) can be obtained in the investigated spectral range by employing a lens with f =75 mm for wavelengths lower than 3.9 μm, f=50 mm for wavelengths in the range 3.9-6 μm and f

=25 mm for wavelengths greater than 7.8 μm. When using HCW a_2 input bore radius, η_{11} can be kept >90% with f =75 mm for wavelengths in the range 3.4-5.2 μm and f =50 mm for wavelengths in the range 4.9-7.8 μm.

While propagating in the waveguide, each m^{-th} HCW mode undergoes an attenuation, depending on the waveguide length L, the optical properties of the metallic and dielectric HCW layers and the u_{1m} coefficient. To estimate the propagation losses, the equation derived by Miyagi and Kawakami in Ref. 11 to determine the attenuation coefficients α_{1m} for the HE_{1m} waveguide modes can be employed:

$$\alpha_{1m} = \left(\frac{u_{1m}}{2\pi}\right)^2 \frac{\lambda^2}{a(z)^3} \frac{n}{n^2+k^2} \frac{1}{2}\left(1+\frac{n_d^2}{\sqrt{n_d^2-1}}\right)^2 = K\frac{u_{1m}^2\lambda^2}{a(z)^3} \ , \tag{2.5}$$

with

$$K = \left(\frac{1}{2\pi}\right)^2 \frac{n}{n^2+k^2} \frac{1}{2}\left(1+\frac{n_d^2}{\sqrt{n_d^2-1}}\right)^2 . \tag{2.6}$$

Here, n and k are the real and imaginary parts of the complex index of the metallic layer, while n_d is the refractive index of the dielectric film.

The theoretical propagation losses can be calculated by using the following expression [9]:

$$L_p(dB) = -10Log_{10}\left(\sum_m \eta_{1m} \exp\left(-2\int_0^L \alpha_{1m}(z)dz\right)\right). \tag{2.7}$$

For a cylindrical HCW with $a(z)$ constant along the z direction, by combining Eqs. (2.5)-(2.7), L_p can be written as:

$$L_p(dB) = -10Log_{10}\left(\sum_m \eta_{1m} \exp\left(-2Ku_{1m}^2\lambda^2\frac{L}{a}\right)\right). \tag{2.8}$$

Using Eq. (2.8), we calculated L_p values as a function of the wavelength when coupling a laser with a cylindrical HCW having length L=50 cm and bore radius measuring $a=a_1$ or $a=a_2$, respectively. Three coupling lens focal lengths, f = 25 mm, f = 50 mm and f = 75 mm, were investigated and results are reported in Figs. 2.4(a)-(b). In Figs. 2.4(c)-(d) we reported the corresponding w_0/a_i ratios. For the wavelength dependence of n, k and n_d we used relations as reported in Ref. 12.

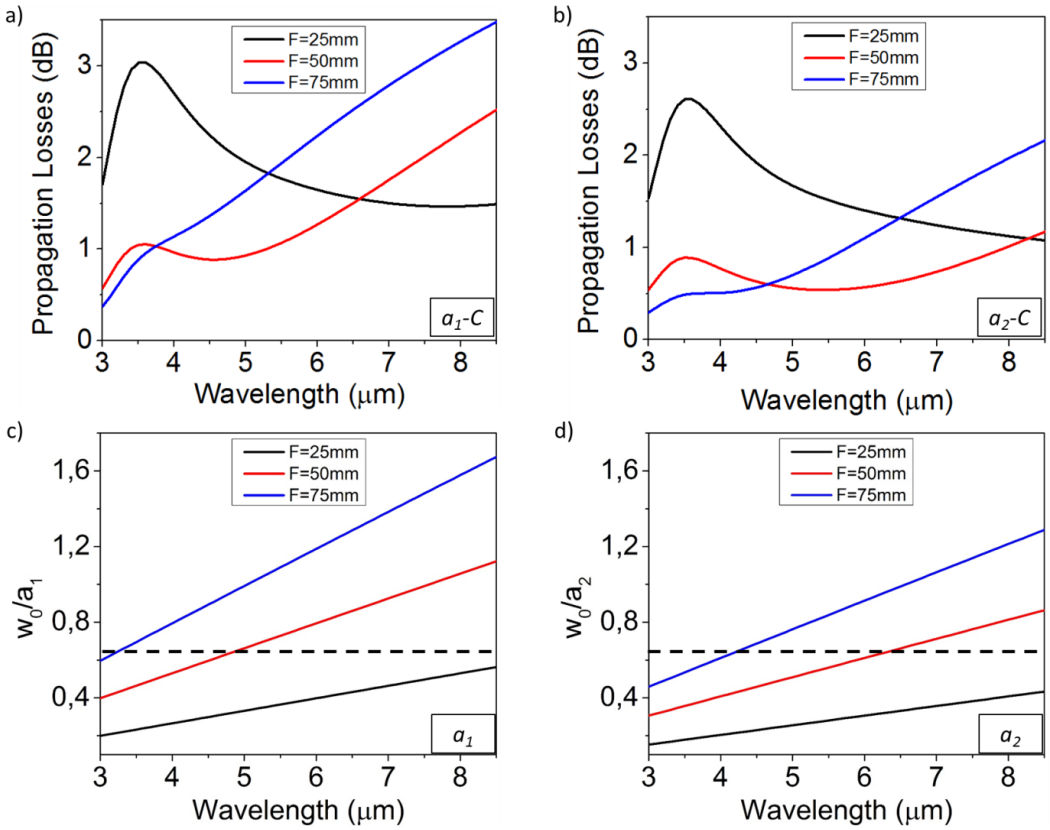

Figure 2.4 Propagation losses (a-b) and w_0/a_i parameters (c-d) as a function of the laser wavelength, when the laser is coupled with a cylindrical HCW having bore radius $a=a_1$ or $a=a_2$, using a coupling lens with f = 25 mm (black solid line), f = 50 mm (red solid line) or f = 75 mm (blue solid line). The black dashed lines correspond to a w_0/a value of 0.64. The label *C* indicates ligth propagation through a cylindical HCW.

The theoretical results in Fig. 2.4 show that with a cylindrical HCW having a bore radius of 100 μm, propagation losses of ≈1 dB and single mode output can be obtained for wavelengths in the 3 μm – 5.5 μm spectral range by properly selecting the coupling lens focal length. For this wavelengths range, larger bore radius, a_2 =130 μm, allows slight lower losses and w_0/a values less spreading around the optimum value. However, such a radius cannot guarantee single mode output for longer wavelengths, where a bore radius of 100 μm is needed, even if higher losses are expected.

For cylindrical HCWs, the bore radius *a(z)* is constant along the *z* direction, while, in the more general case of a tapered HCW, the inner core radius *a*(z) varies linearly along the waveguide as:

$$a(z) = \frac{a_{output} - a_{input}}{L} z + a_{input} \tag{2.9}$$

where a_{input} and a_{output} are the bore radii at the HCW input and output, respectively.

For a tapered HCW as described by Eq. (2.9), L_p turns out to be:

$$L_p(dB) = -10Log_{10}\left(\sum_m \eta_{1m} \exp\left(-2Ku_{1m}^2 \lambda^2 L \frac{a_{input} + a_{output}}{2a_{input}a_{output}}\right)\right). \quad (2.10)$$

In the case of a tapered HCW, while the attenuation coefficients do not change whether a_1 or a_2 are selected as the input core size, the propagation losses L_p are affected by which HCW side is chosen, since the coupling efficiency depends on the w_0/a_i ratio. These dependences cannot be extracted by the standard ray-optics model, for which propagation losses are not dependent on input tapered HCW bore radius [3]. For a tapered HCW 50 cm long with bore radii a_1 and a_2, using Eqs. (2.9) and (2.10), we calculated L_p values as a function of the wavelength with f = 25 mm, f = 50 mm and f = 75 mm, respectively, as reported in Figs. 2.5(a)-(b).

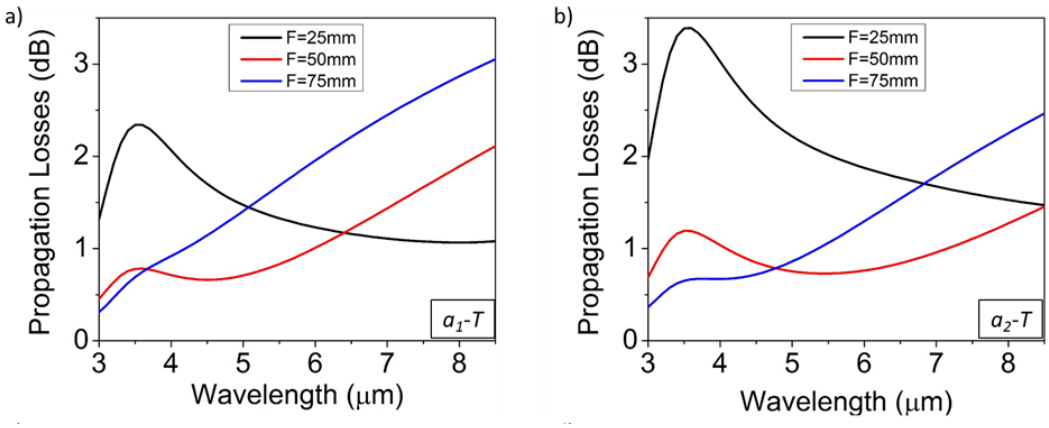

Figure 2.5 Propagation losses through the a_1 (a) or the a_2 (b) tapered HCW input side, using a coupling lens with a coupling lens with f = 25 mm (black solid line), f = 50 mm (red solid line) or f = 75 mm (blue solid line). The label T indicates ligth propagation through a tapered HCW.

The simulation results reported in Fig. 2.5 show that with a tapered hollow-core waveguide propagation, losses ≤1 dB and a single mode output beam can be obtained in the whole investigated spectral range by properly selecting the focal length of the coupling lens and the bore radius, a_1 or a_2, to be employed as the tapered HCW input side.

2.3 Propagation through cylindrical hollow-core waveguides in the 3.7-7.3 µm spectral range

Three HCWs with a cylindrical bore, having a cross-section radius $a = a_1 = 100$ µm and lengths of 15 cm, 30 cm, and 50 cm, produced by Opto-Knowledge Systems, Inc. (OKSI), were used in this work. The HCWs AgI coating was designed to provide low propagation losses in the mid-infrared spectral range from 3.5 µm to 12 µm, as confirmed by the absorbance profile shown in Fig. 2.6.

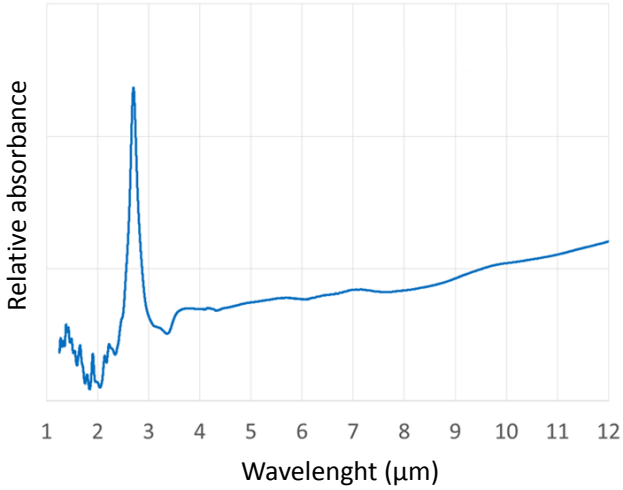

Figure 2.6 Hollow-core waveguide (HCW) relative absorbance measured in the range 1–12 µm using a FTIR spectrometer.

The optical coupling between the QCL and the HCW was carried out by employing the experimental setup schematically represented in Fig. 2.7.

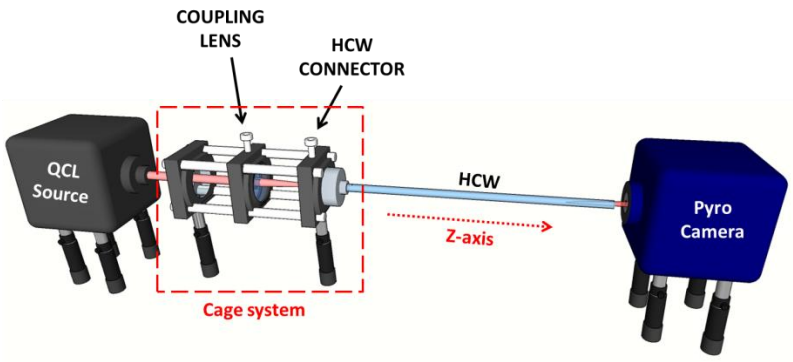

Figure 2.7 Schematic of the experimental setup used to optically couple quantum cascade laser (QCL) sources and the HCWs. A ZnSe lens is used to focus the collimated beam exiting from the QCL onto the waveguide entrance. An infrared pyrocamera detects the profile of the beam exiting from the HCW.

In order to investigate the beam guiding properties of HCWs in a wide mid-infrared spectral range, we employed four commercial tunable external cavity QCLs (Pranalytica) operating at 3.7 μm (model MONOLUX 38), 4.5 μm (model MONOLUX 45), 4.9 μm (model MONOLUX 53), and 7.3 μm (model MONOLUX 74), respectively. All Monolux QCLs are equipped with custom-designed ZnSe aspherical collimating lenses, which are optimized to provide low output beam divergence. In order to realize fine adjustments of the optical coupling between the laser beam and the HCW, we developed a cage system, which includes a mount that allows a fine adjustment of the coupling lens position in the x–y planes and a fiber connector mounting to hold the HCW, as shown in Fig. 2.7. The lens has a diameter of 1/2", and the cage system allows fine adjustments to the distance between the lens and the HCW entrance along the optical z-axis. The HCW connector allows changes of the HCW position entrance with respect to the focused laser spot. With such an optomechanical system, both the azimuthal and polar angles of the waveguide entrance with respect to the laser beam direction can be precisely adjusted. The far field mode profile of the laser beam exiting the HCW was recorded by means of an infrared pyro-camera (Pyrocam III, Ophir Spiricon, 124 × 124 pixels, spatial resolution of 100 μm), positioned at a distance of 2 cm from the HCW exit. The optical power of the laser beam exiting from the HCW was measured by replacing the pyrocamera with an infrared power meter detector.

The QCLs beam profiles were recorded by positioning the infrared pyro-camera 7 cm away from the QCL exit and are shown in Figs. 2.8(a)–(d). Based on the theoretical model presented in Section 2.2, for our experiments, a lens with focal length f = 50 mm was selected for the QCL operating at 7.3 μm and f = 75 mm for the other three QCLs. We coupled the QCL beams into the waveguide by positioning the focusing lens 7 cm from the QCL output. The best coupling conditions were obtained by maximizing the HCW output power [13].

In Table 2.1, measured w beam radius and calculated waist radius w_0 at the focal plane are listed, as obtained using Eq. (2.1), based on the coupling lens selected for each QCL source.

Table 2.1 w values calculated by using the second-order moments method; w_0 values calculated from Equation (2.1) when a coupling lens with a focal length f is employed.

	7.3-μm QCL	4.9-μm QCL	4.5-μm QCL	3.7-μm QCL
w (mm)	2.51	2.05	1.92	1.99
f (mm)	50	75	75	75
w_0 (μm)	69	59	54	54

Figures 2.8(e)–(m) show the beam profiles obtained at the exit of a 15-cm- and 30-cm-long HCW in straight positions for the QCL emitting at 7.3 μm (Figs. 2.8(e) and (k)), at 4.9 μm (Figs. 2.8(f) and (j)), 4.5 μm (Figs. 2.8(g) and (l)), and 3.7 μm (Figs. 2.8(h) and (m)). To collect the beam profile, we positioned the pyro-camera 2 cm far from the waveguide exit.

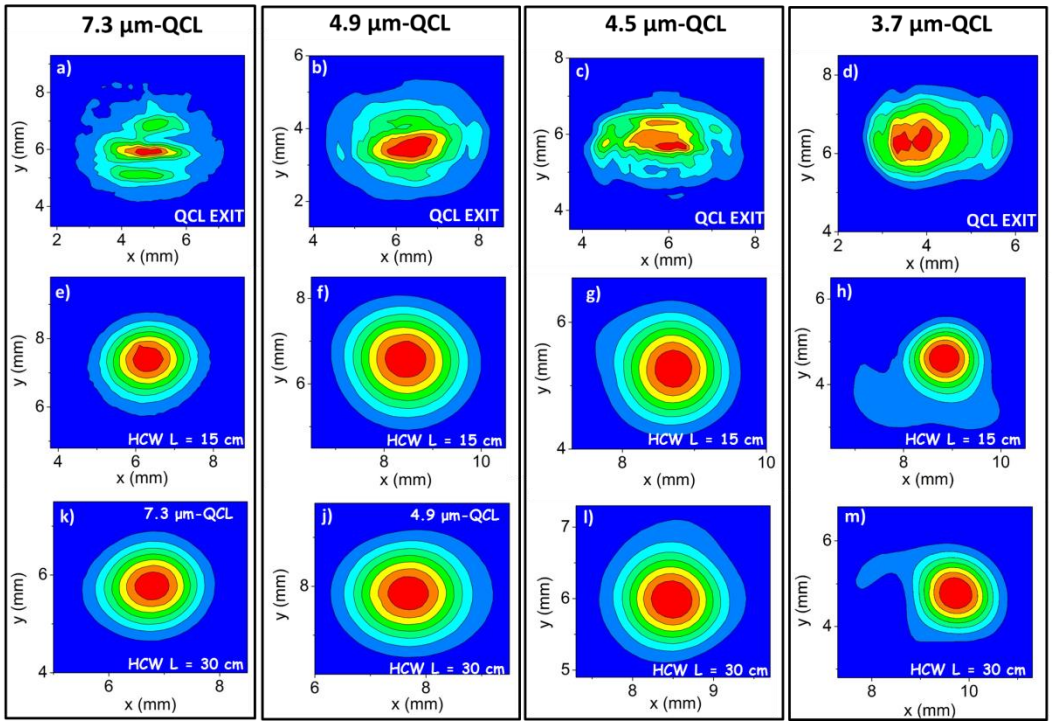

Figure 2.8 Beam profiles of the QCL at 7.3 μm (a), at 4.9 μm (b), at 4.5 μm (c), and at 3.7 μm (d), recorded by positioning the infrared pyro-camera 7 cm away from the QCL exit. (e–m) The HCW output beam profiles were measured for the 15-cm- (e–h) and 30-cm-long (k–m) waveguides. The focusing lens was positioned at a distance of 7 cm from the QCL output, and the pyrocamera was located at ~2 cm from the HCW exit.

The measured profiles demonstrated that, despite the low quality of the input laser beam, cylindrical HCWs with a core size as small as 200 μm (bore radius 100 μm) allow single-mode output with a Gaussian-like beam profile down to a wavelength of 4.5 μm. Indeed, the QCLs mode are perfectly matched to the HE_{11} guided mode, as shown by the circular-symmetric beam output [14]. Similar single-mode results were

obtained for the 50-cm-long HCW. For the shorter wavelength QCL emitting at 3.7 μm, the acquired profiles show a Gaussian-like pattern with small tails. However, only <3% of the total power is contained in the beam tails, which can be removed using a pinhole. A similar profile was also observed for the 50-cm-long fiber.

The HCWs output beam spatial quality can be quantified by calculating the parameter M^2 which compares the laser beam angular divergence in the two transverse directions with a diffraction-limited Gaussian beam, which has $M^2 = 1$. For the beam exiting from the QCLs, the M^2 value can be defined as:

$$M_{QCL}^2 = \frac{\theta_{QCL}}{2} \frac{\pi w}{\lambda},$$

(2.11)

where $\lambda/(\pi w)$ is the beam divergence half-angle of a diffraction-limited Gaussian beam and θ_{QCL} is the divergence half-angle of the QCL beam. The M^2 value of the beam exiting from the HCWs can be defined as the ratio between the half-angle beam divergence of the beam and the theoretical half-angle beam divergence:

$$M_{HCW}^2 = \frac{\theta_{HCW}}{2} \frac{2\pi a}{2.4048\,\lambda},$$

(2.12)

where $2.4048 \cdot \lambda/(2\pi a)$ is the theoretical half-angle divergence, calculated by assuming that only the HE_{11} guided mode exits from the waveguide. For both, the QCLs and the waveguide outputs, half-angle beam divergences of the real beam can be calculated by extracting the beam widths *w* from the beam profiles acquired at different distances using the experimental approach reported in [15]. Results obtained for the output of all four QCLs together with results for the same beams after exiting the 15-cm-long HCW are listed in Table 2.2.

Table 2.2. Divergence angles and M^2 values for four QCLs and the 15-cm-long cylindrical HCW.

	7.3-μm QCL	4.9-μm QCL	4.5-μm QCL	3.7-μm QCL
θ_{QCL} (mrad)	2.1	1.8	1.9	1.2
M^2_{QCL}	4.44	4.74	4.62	4.07
θ_{HCW} (mrad)	30.62	22.36	22.14	20.20
M^2_{HCW}	1.14	1.18	1.27	1.42

The calculated M^2 values confirm that the laser beam exiting from the L = 15 cm HCW shows a substantial improvement in spatial quality with respect to the input laser beam. Similar M^2 values were obtained for the 30 cm and 50 cm long HCWs.

Experimental values of the HCW total losses can be calculated from the ratio between the power at the waveguide entrance I_0 and that measured at the fiber exit I_S as:

$$Losses(dB) = 10\log_{10}\left(\frac{I_0}{I_S}\right) \tag{2.13}$$

Figure 2.9 shows the total losses measured for the 15-cm-, 30-cm- and 50-cm-long HCWs, using QCLs emitting at 7.3 μm (Fig. 2.9(a)), 4.9 μm (Fig. 2.9(b)), 4.5 μm (Fig. 2.9(c)), and 3.7 μm (Fig. 2.9(d)), for their respective best coupling conditions. Figure 2.9 also includes the theoretical losses, calculated by using Eq. (2.9), as a function of the HCWs length and assuming that the waveguide modes HE_{1m}, with *m* ranging from 1 to 5, propagate inside the waveguide.

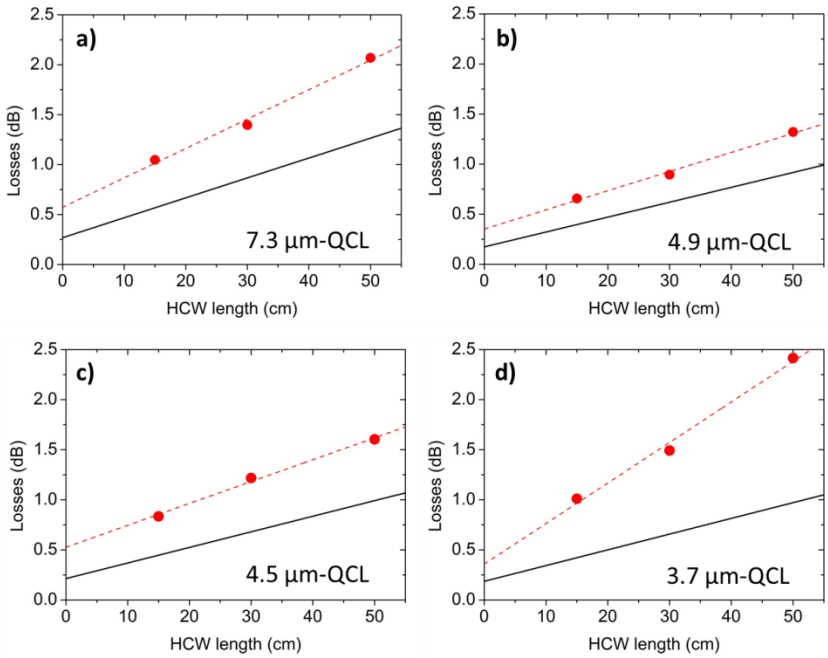

Figure 2.9 Total losses (red dots) measured when coupling the 7.3-μm- (a), 4.9-μm- (b), 4.5-μm- (c) and 3.7-μm-QCL (d) beams into the HCWs having lengths of 15, 30, and 50 cm, plotted as a function of the HCW length. Dashed lines are linear fits to the data. Solid lines are the theoretical losses calculated by using Eq. (2.8).

Measured optical losses are higher than the calculated ones. These discrepancies can be attributed to the poor spatial laser beam quality, which impacts: (i) the estimation of theoretical coupling efficiencies (calculated by assuming a perfect two-dimensional Gaussian elliptical profile for the laser beam) and the consequent propagation losses;

and (ii) the beam waist sizes at the waveguide entrance. From the intercept of the linear fit in Fig. 2.9, we extracted the coupling efficiency values η_{exp}, reported in Table 2.3, together with the theoretical values calculated by using Eqs. (2.3) and (2.4). A very good data agreement (<7% discrepancy) was obtained.

Table 2.3. Theoretical coupling efficiencies into the lowest-order mode η_1 and experimental η_{ext} values.

	7.3-μm QCL	4.9-μm QCL	4.5-μm QCL	3.7-μm QCL
η_1	0.94	0.96	0.95	0.96
η_{exp}	0.88	0.92	0.89	0.92

In Fig. 2.10, the total losses are plotted as a function of the lasers wavelength for all three HCW lengths.

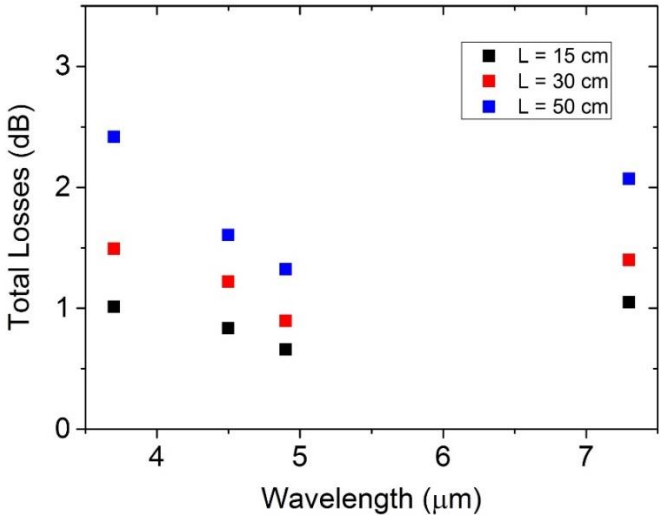

Figure 2.10 Total losses as a function of the QCLs emitting wavelengths for HCWs with L = 15 cm (black squares), 30 cm (red squares), and 50 cm (blue squares).

This graph clearly shows that, for all investigated HCW lengths, the measured loss changes are less than 1 dB when the laser wavelengths span from 3.7 to 7.3 μm, confirming that the internal coatings enhance the HCW spectral response to 3.7 μm. Moreover, the losses remain ≤1 dB in the investigated wavelength range for the 15-cm-long HCW.

The $1/a(z)^3$ dependence (Eq. (2.5)) predicts a strong increase in HCW losses as the fiber bore diameter is reduced. As shown in Fig. 2.4(d), a large bore diameter cannot ensure a single-mode profile at the waveguide output. From Eqs. (2.5) and (2.8), we can see that for large bore sizes α_n is small and higher-order modes have lower losses with respect to

those obtained for small bore sizes, for which α_n is larger. Thus, there is significantly less mode mixing at the HCW output in waveguides with reduced bore size. Mode mixing can be reduced by increasing the fiber length at the expense of larger optical losses. The spatial quality of the input laser beam must also be taken into account, since it influences the input power percentage coupled into the guided modes (see Eq. (2.4)). The larger the amount of input power coupled into the high-order modes, the larger their contributions to total propagation losses will be. As a result, an HCW with a small bore size can exhibit a single-mode output profile, but with optical losses significantly higher than those theoretically predicted. To investigate the influence of the HCW bore size on optical losses and output beam profile, we coupled a 100-μm- and a 150-μm bore radius HCW, both having a length of 15 cm, with a Daylight Solution external cavity QCL (DLS-QCL) emitting at 7.6 μm. The beam profile at the DLS-QCL exit is shown in Fig. 2.11(a). The DLS-QCL was coupled with a 100 μm bore radius HCW by using a coupling lens with a focal length of 25 mm, selected by using then theoretical model in Section 2.2. For the 150 μm bore radius HCW, a focal length of 50 mm was used. The output profiles of the 100 μm and 150 μm bore radius HCWs (both with L = 15 cm) are shown in Fig. 2.11(b) and 2.11(c), respectively.

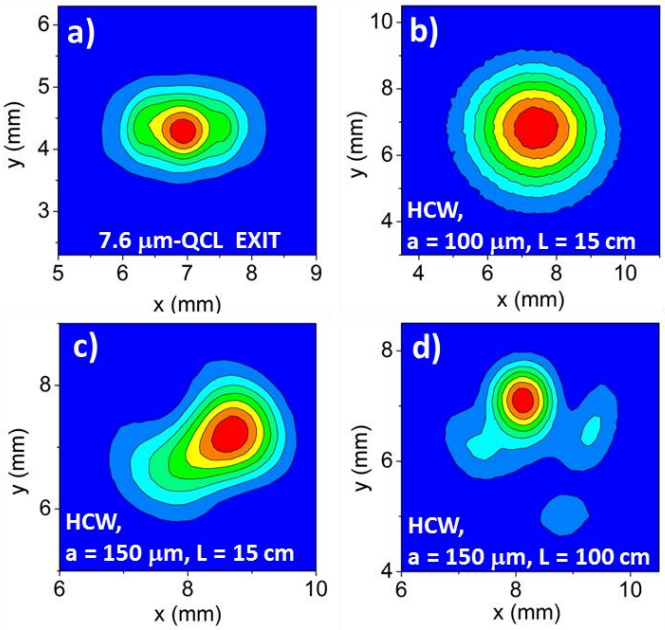

Figure 2.11 Beam profile at the exit of DLS-QCL emitting at 7.6 μm(a). Beam profiles with a 100 μm bore radius and 15-cm-long HCW (b); 150 μm bore radius and 15 cm length HCW (c); and 100 μm bore radius and 100 cm length HCW (d) exits. The focusing lens was positioned at a distance of 5 cm from the QCL output and the pyrocamera was located at ~2 cm from the HCWs exit.

The intensity distribution at the output of the 100 μm bore radius and 15 cm-long HCW, shown in Fig. 2.11(b), is single mode. At the HCW exit, optical losses of 0.74 dB were measured, slightly higher than those theoretically predicted (0.65 dB) by using Eqs. (2.5) and (2.8). This confirms that the quality of the laser beam influences the total losses, but not the output beam profile. Conversely, the intensity distribution is multimodal for the 150 μm bore radius and 15 cm long HCW, as shown in Fig. 2.11(c). We measured losses as high as 1.14 dB, 0.56 dB higher than the theoretical value. This discrepancy is largely due to the propagation of higher-order modes, which have greater losses than the lowest-order HE_{11} mode. To verify whether the contribution to higher-order modes at the 150 μm bore radius HCW exit can be suppressed by increasing the fiber length, we coupled the DLS-QCL with a 100 cm long, 150 μm bore radius HCW. The coupling conditions were the same as used for 150 μm bore radius and 15 cm long HCW. The acquired output beam profile is reported in Fig. 2.11(d). Clearly, the profile is still multimodal, with optical losses of 3.45 dB (1.62 dB are the theoretical losses), demonstrating that the only way to achieve single-mode beam delivery in the spectral range of 4.5–7.6 μm is to use HCWs with a bore radius as small as 100 μm. For this condition, a length as short as 15 cm is sufficient to provide a single-mode output, even if the spatial quality of the input laser beam is not good. For longer fibers, single-mode output is ensured but optical losses increase. For the spectral range 8–11 μm, both 100 μm and 150 μm bore radii can guarantee single-mode beam delivery [16], but it is preferable to employ a bore radius of 150 μm, since it provides lower optical losses.

2.4 Tapered hollow-core waveguides for light delivery in the 3.5-7.8 μm spectral range

In this section, the properties of a tapered HCW with the bore diameter linearly increasing from $2a_1$ = 200 μm to $2a_2$ = 260 μm for a L = 50 cm fiber length are investigated. The dielectric layer thickness of the tapered HCW was designed to optimize the fiber performance in the 4 μm -10 μm spectral range [17]. The 50 cm-long fiber used for the studies reported here was cut from a coated fiber that was originally 2.5 meters long. Figure 2.12 shows the FTIR absorption spectrum measured in the 2.5 μm - 8.5 μm spectral range for a 7 cm long tapered fiber segment cut from the same

longer stock fiber near the small side of the HCW, and is thus a good representation of the spectral absorption of the fiber used in this work.

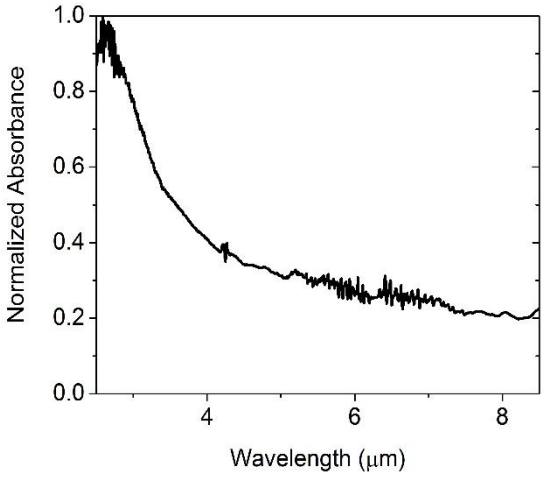

Figure 2.12 Absorbance profile of a 7 cm-long tapered HCW segment. The diameter of this tapered HCW segment ranges from ~190 – 200 μm over its length of 7 cm. The thickness of the dielectric layer is optimized for wavelengths > 5 μm.

The measured absorbance changes slightly from 8 μm to 5 μm, while it increases rapidly at shorter wavelengths. Therefore, higher losses are expected to occur at wavelengths < 5 μm. The performance of the tapered 50 cm-long HCW was experimentally investigated by employing three mid-IR Distributed Feedback Quantum Cascade Lasers (DFB-QCLs), one mid-IR External Cavity Quantum Cascade Laser (EC-QCL) and one Interband Cascade Laser (ICL), emitting at wavelengths of 7.8 μm (Corning, DFB-QCL), 6.2 μm (Daylight, EC-QCL), 5.2 μm (Hamamatsu, DFB-QCL), 4.6 μm (AdTech, DFB-QCL) and 3.5 μm (Nanoplus, ICL). Figure 2.13 shows the beam profiles acquired at a distance of 7 cm from the output of these lasers using the Spiricon pyro-camera.

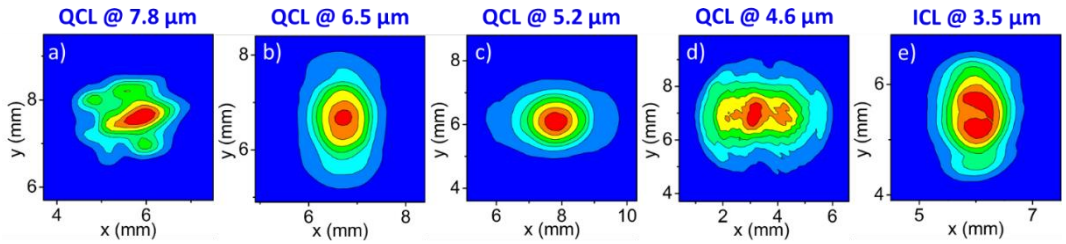

Figure 2.13 Beam profiles acquired by positioning the pyrocamera 7 cm from the output of the 7.8 μm-QCL (a), 6.2 μm-QCL (b), 5.2 μm-QCL (c), 4.6 μm-QCL (d) and 3.5 μm-ICL (e).

The five lasers exhibit low spatial beam qualities with asymmetric far field optical power distributions. In particular, the beam profiles of the QCLs emitting at 7.8 μm and at 4.6 μm and of the ICL at 3.5 μm show the presence of multiple lobes. For this reason, we calculated the second-order moment of the intensity distribution along both *x* and *y* directions, as reported in Ref. 16, to extract the beam diameters. For the five lasers, an average value for the beam diameter of w = 2 mm was estimated. The employed laser sources were optically coupled with the tapered HCW by using as the input a_1 or a_2.

The optical coupling setup is similar to the one shown in Fig. 2.7 for cylindrical HCWs. A ZnSe coupling lens with an AR coating in the spectral range 3-12 μm was used to focus the collimated laser beams into the tapered HCW. We selected lenses with f = 25 mm, 50 mm and 75 mm. For each focal length, we used the theoretical model described in Section 2.2 to evaluate the coupling efficiency and the w_0/a_i ratios when the laser beams are coupled to the a_1 or a_2 HCW sides. In Table 2.4, for each wavelength, we reported the focal length providing the best coupling conditions, i.e., highest coupling efficiencies η_{11} and w_0/a_i ratios as close as possible to the optimum value of 0.64.

Table 2.4. Focal lengths f providing the best coupling conditions for each laser source and corresponding η_{11} and w_0/a_i values, using a_1 or a_2 as fiber input side.

		7.8 μm QCL	6.2 μm QCL	5.2 μm QCL	4.6 μm QCL	3.5 μm ICL
a_1	f	25 mm	50 mm	50 mm	75 mm	75 mm
	η_{11}	89.6%	88.6%	94.0%	83.6%	93.8%
	w_0/a_1	0.52	0.82	0.69	0.91	0.70
a_2	f	25 mm	50 mm	75 mm	75 mm	75 mm
	η_{11}	72.2%	94.6%	89.9%	93.6%	91.1%
	w_0/a_2	0.40	0.63	0.80	0.70	0.54

Theoretically it is possible to reach coupling efficiencies with the HE_{11} waveguide mode > 89%, by selecting the right input side.

The laser beam profiles, acquired with the pyrocamera located 4 cm from the tapered HCW output, at the coupling conditions reported in Table 2.4, are shown in Figs. 2.14(a)-(e) and (f)-(j), respectively when a_1 or a_2 is used as fiber input side.

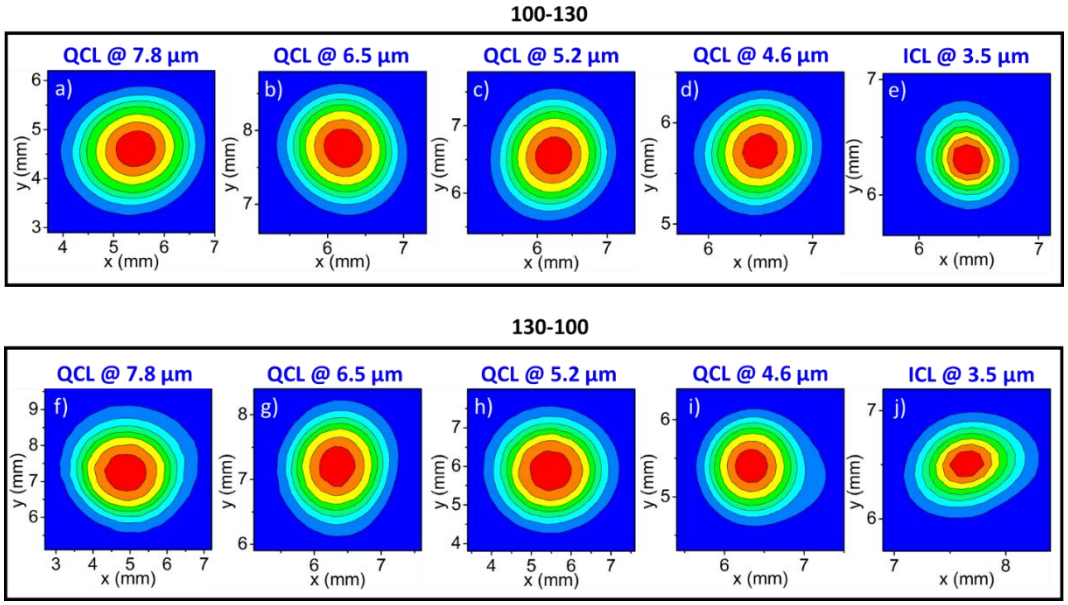

Figure 2.14 (a-e) Beam profiles of the five lasers acquired 4 cm from the tapered HCW exit when a_1 is used as input side. (f-j) Beam profiles of the five lasers acquired 4 cm from the tapered HCW exit when a_2 is used as input side. The coupling conditions are reported in Table 2.4.

Despite the low spatial quality and, in some cases, multimodal intensity distribution of the input laser beams, the tapered HCW provides single-mode circular-symmetric Gaussian-like outputs in the 3.5 µm - 7.8 µm investigated spectral range, whenever using a_1 or a_2 as fiber input side. Thereby, the selection of the input side giving the best coupling conditions requires the investigation of the related optical losses. As reported in Section 2.3, the spatial quality of the laser beam coming out the waveguide exit can be quantified by calculating M^2 parameter. In Table 2.5 we reported both the half-angle beam divergence and the calculated M^2_{HCW} values.

Table 2.5 Half-angle beam divergences and related M-squared values, for each laser coupled by using a_1 or a_2 as fiber input side.

		7.8 µm QCL	6.2 µm QCL	5.2 µm QCL	4.6 µm QCL	3.5 µm ICL
a_1	θ	34.3 mrad	27.7 mrad	22.3 mrad	18.7 mrad	15.3 mrad
	M^2_{HCW}	1.15	1.16	1.12	1.06	1.14
a_2	θ	26.6 mrad	20.2 mrad	16.4 mrad	14.5 mrad	18.7 mrad
	M^2_{HCW}	1.16	1.10	1.07	1.07	1.38

Apart from the 3.5 µm-ICL coupled by using a_2 as fiber input side, M^2 values in the range 1.06 – 1.16 were obtained, confirming the achievement of a single mode output close to a pure Gaussian beam at the waveguide exit.

We calculated the total losses L_t for each laser source, by measuring the optical power at the input and at the output of the tapered HCW at the coupling conditions reported in Table 2.4. The results are shown in the histogram in Fig. 2.15, where it is compared the measured losses when a_1 (red bars) or a_2 (blue bars) are selected as input side.

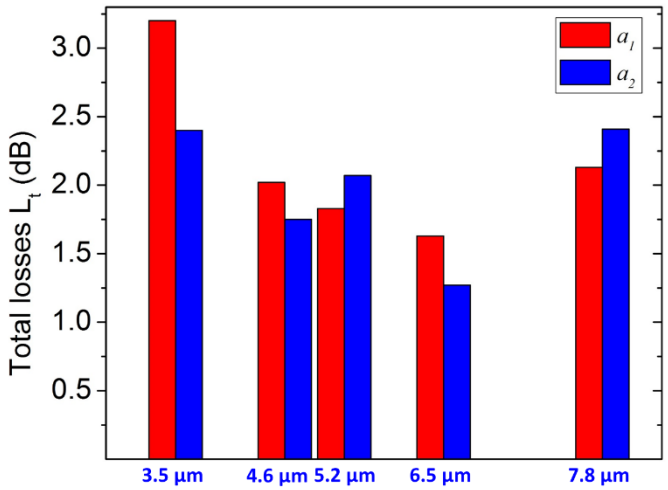

Figure 2.15 Total losses L_t measured for each laser source, when a_1 (red bars) or a_2 (blue bars) was used as the HCW input side.

In agreement with the FTIR absorbance measurements reported in Fig. 2.11, the total losses increase at 3.5 µm. It is worth noting that, for each laser source we reached lower losses when the tapered HCW is coupled using the input side giving the larger coupling efficiency η_{11} in Table 2.4.

In Table 2.6, for each laser source are summarized the best single-mode coupling conditions, i.e., coupling lens focal length f, input side a_i, coupling efficiency η_{11}, w_0/a_i ratio and theoretical propagation losses L_p, as well as corresponding measured total losses L_t.

Table 2.6 Coupling lens focal length f, average beam diameter $2w$, input HCW side radius a_i, theoretical coupling efficiency η_{11}, theoretical w_0/a_i ratio, theoretical propagation losses L_p and measured total losses L_t, at the corresponding best coupling conditions for each investigated laser source.

	7.8 µm QCL	**6.2 µm QCL**	**5.2 µm QCL**	**4.6 µm QCL**	**3.5 µm ICL**
f	25 mm	50 mm	50 mm	75 mm	75 mm

2w	1.9 mm	2.3 mm	2.8 mm	3.5 mm	1.9 mm
a	a_1	a_2	a_1	a_2	a_2
η_{11}	89.6%	94.6%	94.0%	93.6%	91.1%
w_0/a	0.52	0.63	0.69	0.70	0.54
L_p **(dB)**	0.98	0.8	1.52	0.74	0.65
L_t **(dB)**	2.13	1.27	1.83	1.75	2.4

In the 4.6 μm - 7.8 μm spectral range, discrepancies between the losses L_t -L_p < 1.1 dB were obtained. At 3.5 μm, this discrepancy increases up to 1.75 dB. These results suggest that Eq. (2.10) provides a reliable estimation of L_t for wavelengths > 4.6 μm, while at shorter wavelengths additional contributions to the losses should be taken into account. The overall losses underestimation can be ascribed to the low spatial quality of the laser beams. Indeed, in the theoretical model we assumed a pure Gaussian optical power distribution of the laser beams at the HCW input. For not-Gaussian input beam profiles the amount of the optical power coupled with the higher-order HCW modes increases, giving rise to higher total losses. The larger discrepancy observed at 3.5 μm is due to a dielectric layer for this wavelength that is thicker than optimal and this effect is visible in Fig. 2.12.

2.5 HCW-coupled QEPAS sensor for gaseous leak detection

In the previous sections we demonstrated the capability of hollow-core waveguides to act as an efficient, mid-IR spatial modal beam filter with single-mode Gaussian-like beam output. Thanks to these characteristics HCWs can find application in many imaging and sensing systems, where a good laser beam quality with circular symmetry, as close as possible to the fundamental transverse TEM_{00} mode, and essentially diffraction-limited low beam divergence with M^2 values in the range 1.0–1.3 are required.

In this section the implementation of a cylindrical HCW in a QEPAS-based sensor for gaseous leak detection is reported. Such a sensor was implemented into a vacuum-seal

test station for mechanical valves and sulfur hexafluoride (SF_6) was selected as leak tracer, because it is a stable, heavy, inert, nontoxic and nonflammable gas [18].

The experimental apparatus used for QEPAS detection of SF_6 is shown in Fig. 2.16 and is similar to that used in [19, 7]. The light source is an external-cavity quantum cascade laser emitting at ~ 10.56 µm. The radiation is focused into a hollow core waveguide with an internal diameter of 300 µm by using a ZnSe lens (focal length f = 40 mm and diameter of 1 inch). The light exiting the HCW is focused into an Acoustic Detection Module (ADM) by a focusing system [7]. The ADM contains a standard 32 kHz-QTF, two micro-resonator tubes for acoustic amplification, two ZnSe windows, and is connected to the input gas line. The ADM volume is ~ 2 cm^3. The use of an HCW improves the QCL beam profile by filtering out higher order modes and providing a single-mode Gaussian-like laser beam output, allowing an optimal focalization of the laser beam through the two micro resonator tubes and between the QTF prongs. The interaction between the radiation and the SF_6 molecules generate sound waves, which excite the vibration of the QTF prongs. The light exiting from the ADM is re-collimated using another ZnSe lens (f=40 mm, diameter of 1 inch) and passes through a reference cell, filled with a 0.1% mixture of SF_6 in N_2.

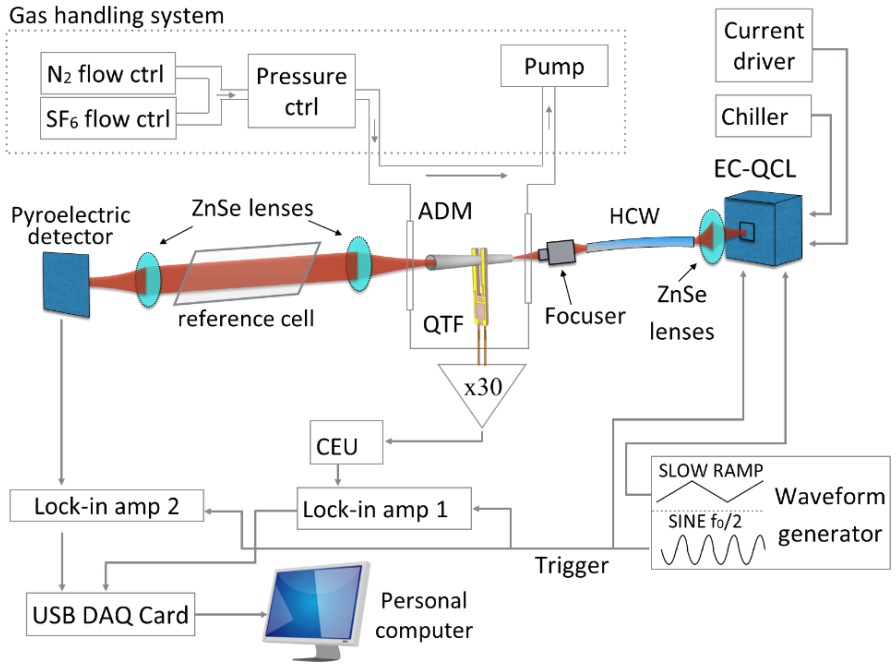

Figure 2.16 Block diagram of the experimental apparatus. ADM = Acoustic detection module; QTF = Quartz tuning fork; HCW = Hollow core waveguide; EC-QCL = external cavity quantum cascade laser; CEU = Control electronics unit; DAQ = Data acquisition.

A pyroelectric detector measures the light absorption and provides a useful spectral reference for the identification of the SF_6 absorption lines. This part of the experimental setup serves only for the QEPAS sensor calibration and validation and was removed in the final leak test station in order to reduce the sensor system size.

The QTF is transduced and amplified by a transimpedance amplifier (with a 10 MΩ feedback resistor) and then processed by a Control Electronics Unit (CEU). The CEU determined the main QTF parameters: resistance R, quality factor Q, and resonant frequency f_0. The CEU is also used to transfer the signal coming from the transimpedance amplifier to the lock-in amplifier. A wavelength modulation (WM) technique was implemented by applying a sinusoidal dither to the laser current at half of the QTF resonance frequency ($f_0/2$) and detecting the QTF response at f_0 by means of a lock-in amplifier. WM QEPAS spectral scans were performed by slowly varying the laser wavelength using a piezoelectric amplifier. The output signal from the lock-in amplifier is digitalized by a National Instruments DAQ card (USB 6008), connected to a personal computer. The temporal evolution of both the piezoelectric signal and the response of the pyroelectric detector are obtained by means of LabVIEW based software. A trace gas standard generator is used to produce SF_6 concentrations in the range 0–10 ppm, using pure or humidified N_2 as the diluting gas, starting from a certified 10 ppm SF_6 in N_2 mixture. The pressure and flow rate of the gas mixture are controlled using a pressure controller (MKS Instruments Type 640) and two flow controllers (Brooks Instruments 5850S). The flow of the gas mixture was set at a constant rate of 0.67 mbar·l/s (0.67 scc/sec = 40 scc/min).

SF_6 has its strongest absorption band in the 10.5-10.6 μm (943-952 cm^{-1}) spectral region [20,21]. In Ref. [14] simulated absorption spectra for a gas mixture of standard air and 10 ppm of SF_6 at 75 Torr pressure is reported in the range 947-950 cm^{-1}, using HITRAN database [22]. For the sensor operation, the strongest line centered at 947.93 cm^{-1} with absorption strength of $1.4 \cdot 10^{-20}$ cm/mol was selected, which is well separated from the only feature potentially interfering in this range: a H_2O absorption band centered at 948.26 cm^{-1}. The laser power was set at 25 mW. The time constant of the lock-in amplifier 1 was set at 100 ms and a signal integration-time of 300 ms was selected using the LabVIEW-based acquisition program. The optimum operating condition in terms of gas pressure P and laser modulation voltage were identified. The conditions providing the highest signal-to-noise ratio are: gas pressure P = 75 Torr and peak-to-peak laser

amplitude modulation voltage of 4.2 V. At these operating conditions, we performed a series of QEPAS spectral scans by varying the SF_6 concentration in the gas mixture. The QEPAS signal was measured at different SF_6 concentration levels, ranging between 132 parts per billion (ppb) and 10 ppm. Figure 2.17(a) shows a selection of QEPAS scans, and in Fig. 2.17(b) the measured peak signals as a function of the SF_6 concentration in the gas mixture are reported. The error bars associated with the SF_6 concentration in Fig. 2.17(b) result from the sensitivity of the flow controllers, while the error bars on the QEPAS signal were determined by the related 1σ noise.

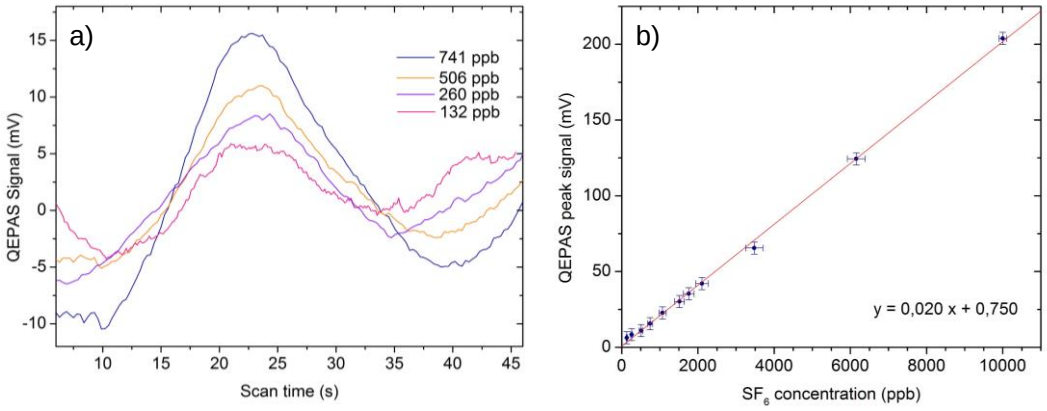

Figure 2.17 QEPAS scans of the absorption line centered at 947.93 cm^{-1} measured for SF_6 concentrations of 741, 506, 260 and 132 ppb (a). The frequency of the voltage ramp used to scan the laser wavelength across the absorption line is 10 mHz. QEPAS peak signals as a function of the SF_6 concentration (b). The straight line is a linear fit of the experimental points.

A linear fit of the experimental data points in Fig. 2.17(b) yields a slope of a = 0.020 mV/ppb and an intercept of b = 0.750 mV. The b value represents the resulting QEPAS background noise level. The R-squared value equals 0.999, which verifies the linearity of the QEPAS signal versus SF_6 concentration. Furthermore, we performed an Allan-Werle variance analysis (see Appendix) to determine the achievable minimum detection limit (MDL) of the QEPAS sensor by acquiring the QEPAS signal when pure N_2 flows in the ADM for a period of 3 hours. The Allan-Werle deviation plot is depicted in Fig. 2.18.

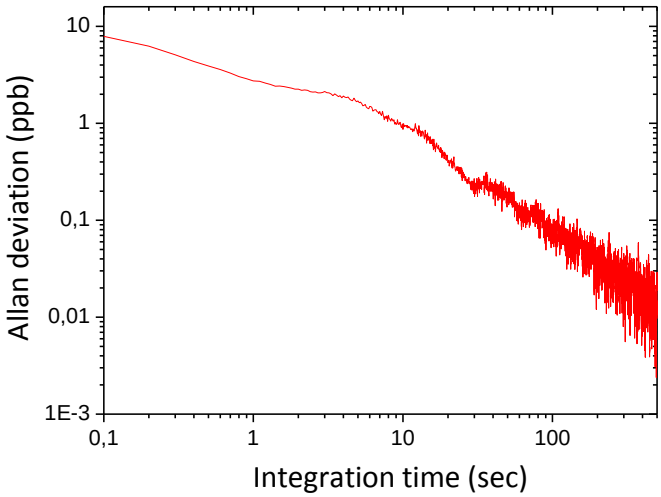

Figure 2.18 Allan-Werle deviation in ppb of the QEPAS signal as a function of the integration time.

For an integration time of 1 s (i.e. a detection bandwidth of 0.16675 Hz), we achieved a MDL value of 2.75 ppb.

The described sensor was implemented in a leak test station intended to detect and quantify leaks in mechatronics systems and components, such as vacuum-valves and diesel injectors, which must operate at high pressures. Figure 2.19 shows the schematic diagram of the QEPAS leak-test station, which includes two pressure meters, a pressure and a flow controller as well as a certified leak inserted in a test chamber for system validation.

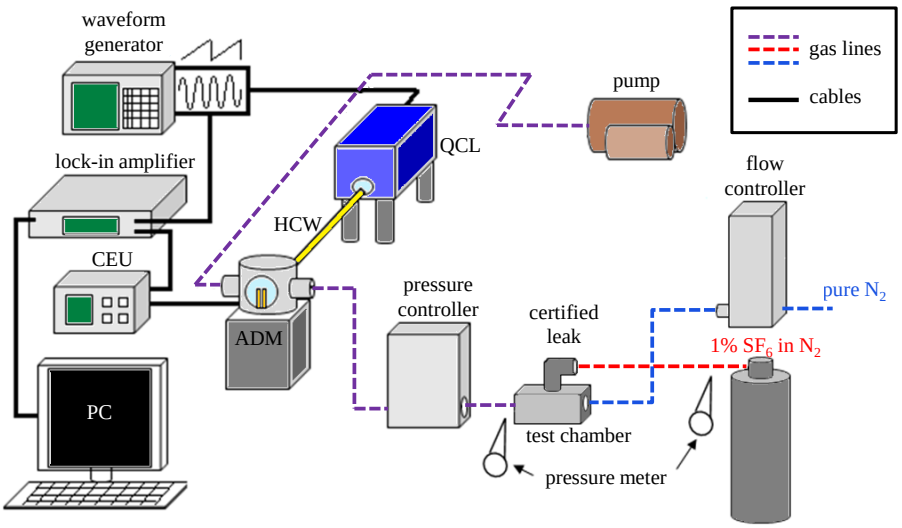

Figure 2.19 Block diagram of the leak-test station. ADM = Acoustic detection module; HCW = Hollow core waveguide; QCL = quantum cascade laser; CEU = Control electronics unit; PC = Personal Computer. The dashed lines mimic the gas lines. Solid lines are electrical connections.

A calibrated leak (ATEQ, model L1147AQ-N) was used to validate the test station. A picture of this leak and the test chamber is shown in Fig. 2.20(a). In order to perform the validation, pure N_2 was passed through the test chamber at a level of 0.67 mbar·l/s, while an overpressure of 1% SF_6:N_2 was applied to the certified leak. A part of this mixture flows through the leak in the test chamber, due to the differential pressure (ΔP) between the test chamber and the SF_6:N_2 mixture. Thus, the gas sample coming out from the test chamber contains a SF_6 concentration, which depends on the leak size. A pressure controller allows the gas mixture to pass through the ADM at a fixed pressure of 75 Torr. In this manner, it is possible to determine the resulting SF_6 concentration using the QEPAS sensor operating in the locked mode, i.e. with the EC-QCL frequency set to the center of the selected SF_6 absorption line. The ΔP was varied between 100 mbar and 1000 mbar for validation of the QEPAS leak-test station. The resulting leak flow FL can be calculated from the following expression:

$$F_L = \frac{F_C \cdot (S - b)}{a \cdot C_{SF_6} - (S - b)} \tag{2.14}$$

where F_C is the N_2 gas carrier flow (0.67 mbar·l/s), S is the QEPAS peak signal recorded for each ΔP considered and C_{SF6} is the certified concentration of SF_6 in N_2 used as leak tracer (C_{SF6} = 0.01 in our experiments). The lock-in amplifier constant time was set at 100 ms and the extracted leak flux as a function of the selected differential pressure is reported in Fig. 2.20(b). The results were compared with the calibration data provided for the certified leak and a very good correlation was obtained. The discrepancies observed for differential pressures < 500 mbar are due to limitations in the differential pressure detector used for calibration, since is approaching its minimum range of leak flux detection.

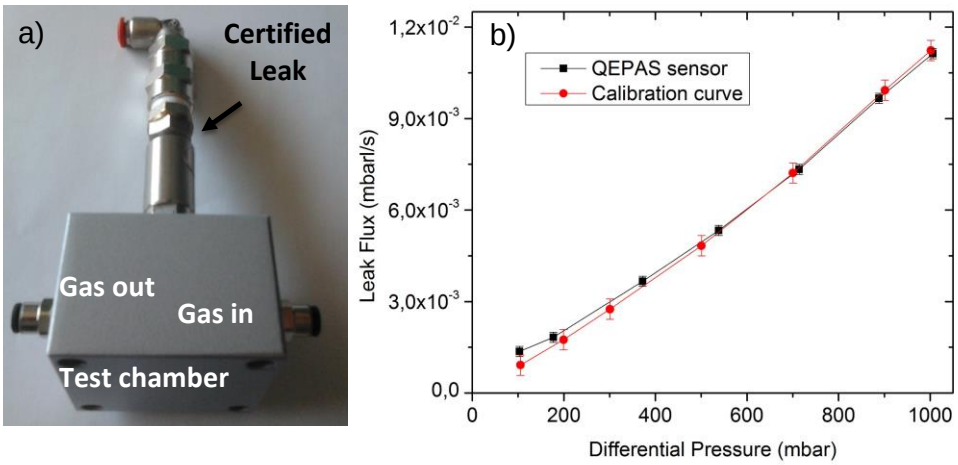

Figure 2.20 Photo of the certified leak inserted in the test chamber (a). The gas-in and gas-out connectors are also visible. Leak flows measured as a function of differential pressure ΔP using the QEPAS sensors (black squares), compared with the calibration data (red circles) provided for the certified leak (b).

The response time of the test station is determined by the flow rate and the length of the gas line connecting the test chamber to the ADM. Considering the ADM volume (~2 cm^3), a 20 cm long connecting tube with a 1.6 mm internal radius and a flow rate of 0.67 mbar·l/s, the response time of the sensor should be lower than 6 s. However, we observed a response time of ~10 s. This response time increase is due to resistance to flow introduced by tube connections and the pressure controller positioned between the test chamber and the ADM. Faster response time can be obtained by increasing the gas flow rate, however values above 1.7 mbar·l/s (100 ssc/min) should be avoided, otherwise noise components due to gas flow turbulences may arise [23].

Once validated, the leak test station was tested with real vacuum-valve samples. Photos of the investigated valves and of their operating principles are shown in Fig. 2.21.

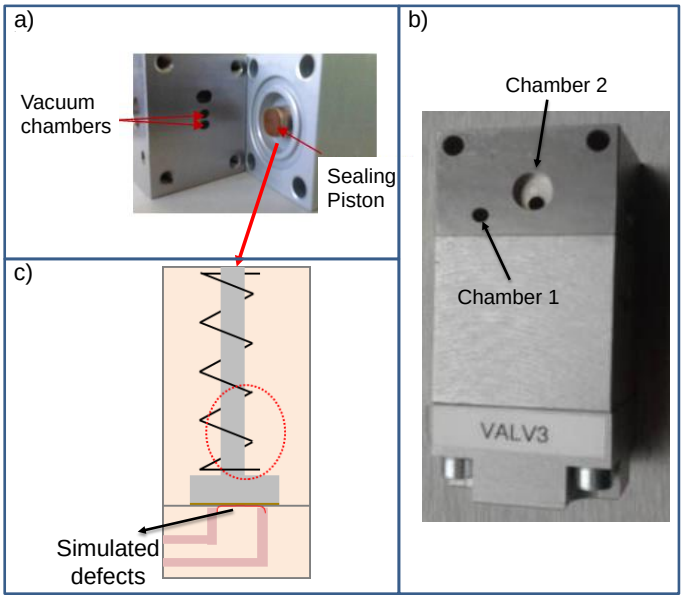

Figure 2.21 Photo of the internal part of the investigated valves (a). The internal holes connected to the two valve chambers are marked by the red arrows. The sealing piston used to close the two holes is visible in the right side. Photo of valve 3 (b). The entrances to the two valve chambers used to inject the test gases are marked by black arrows. Schematic of the valve operation principle (c). The sealing piston pushes over the two internal holes to isolate them. Defects of the valves were simulated by inserting a small wire (small red line in the picture) between the two holes, as marked by the black arrow.

The vacuum valves contain two separated chambers with internal (see Fig. 2.21(a)) and external (see Fig. 2.21(b)) connecting holes. A sealing piston, pushed by a pressure of 5 bars, closes the two internal holes and isolates the two chambers. Pure N_2 flows into valve chamber 1 (see Fig. 2.21(b)), while an overpressure of 1% SF_6:N_2 is created in chamber 2 via the related external holes. In absence of any defect, the sealing piston is able to isolate the two chambers, avoiding contamination of the pure N_2 flow from SF_6 leak tracer gas. We investigated valves with and without simulated defects. These defects were realized by inserting small metallic wires between the two internal holes, as schematically depicted in Fig. 2.21(c). In this way, the wires allow SF_6 contamination into chamber 1. Wires of different diameters, ranging from 20 µm to 170 µm were inserted between the internal holes. Figure 2.22 depicts a picture and a schematic of the test station with a valve under test. The gas delivery system used to connect the two chambers with pure N_2 and the SF_6:N_2 leak gas tracer is also shown. During the valve test, a flux of 0.67 mbar·l/s of N_2 flows through chamber 1, while chamber 2 is filled with the 1% SF_6:N_2 mixture at an overpressure of 400 mbar.

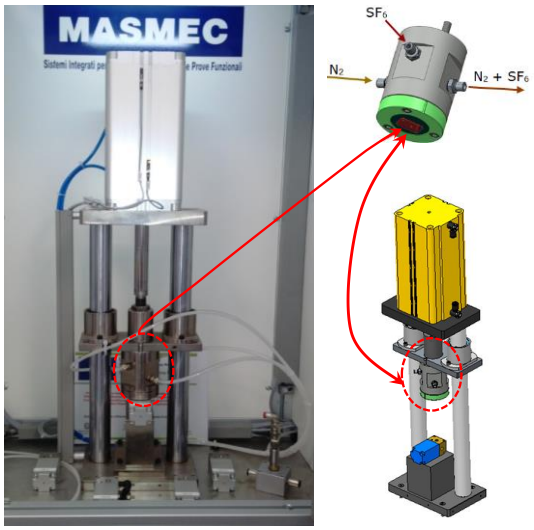

Figure 2.22 Photo and schematic of the valve-seal test station and of the gas delivery system used to connect the two valve chambers. The red dashed circles mark the position of the gas delivery system in the test station.

The QEPAS sensor is operated in the scan mode. The concentration of the resulting SF_6 trace contamination is extracted using the calibration curve reported in Fig. 2.17(b). The spectral scans obtained for the valve without defect and four valves with defects of different size are shown in Fig. 2.23.

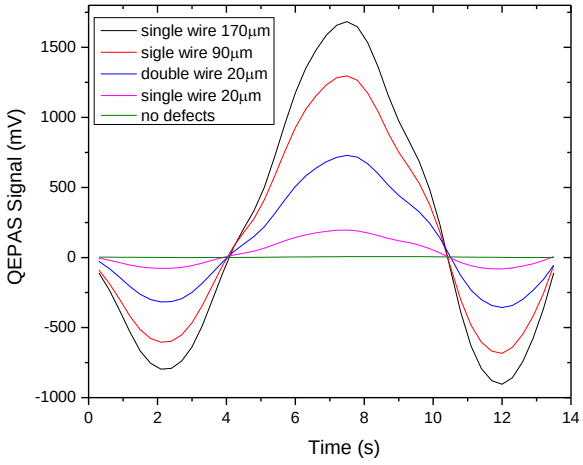

Figure 2.23 QEPAS scans of the absorption line centered at 947.93 cm^{-1} measured for five different valve samples. The frequency of the voltage ramp used to scan the laser wavelength across the SF_6 absorption line is 25 mHz. The related types of defects are reported in the legend.

The leak flows for each valve were calculated using Eq. (2.14) starting from the corresponding QEPAS peak signal S. The obtained leak flow values for the five valves are listed in Table 2.7.

Table 2.7 QEPAS peak signals and related leak flows calculated using Eq. (2.14) for a valve without defects (valve1) and four valves incorporating different defects. The corresponding SF_6 contaminations (in ppm) in the N_2 flow are also reported and were extracted using the calibration curve reported in Fig. 2.17(b).

Valve (type of defect)	QEPAS peak Signal (mV)	Leak flows (10^{-3} mbar·l/s)	SF_6 contamination (ppm)
valve1 (no-defects)	1.10	$3.3 \cdot 10^{-3}$	0.02
valve2 (20 µm wire)	201.11	0.67	10.02
valve3 (20 µm double-wire)	734.69	2.45	36.70
valve4 (90 µm wire)	1299.66	4.36	64.94
valve5 (170 µm wire)	1684.86	5.66	84.21

For valve 1 (without defects), as expected, only noise level leaks were measured, while the valve with the biggest defect (valve5) generates a leak flow of $5.66 \cdot 10^{-3}$ mbar·l/s. This value is close to the minimum detectable leak for a differential pressure detector. The leak detected for the smallest defect was $6.7 \cdot 10^{-4}$ mbar·l/s, measured for valve2. However, the corresponding SF_6 trace-gas concentration (10.02 ppm) is three orders of magnitude higher than the QEPAS sensor MDL value. Starting from a QEPAS sensor noise-equivalent concentration of 2.75 ppb at 1 s integration time and considering a N_2 gas carrier flow of 0.67 mbar·l/s, it is possible to estimate the minimum detectable leak at these conditions, using Eq. (2.14). This results in a leak of ~ $4.5 \cdot 10^{-7}$ mbar·l/s, which can be decreased to ~ $4.5 \cdot 10^{-9}$ mbar·l/s if pure SF_6 is used as leak test gas. A further decrease of the minimum detectable leak could be obtained by reducing the pure N_2 flux. However, values below ~ 0.17 mbar·l/s (10 scc/min) are not practical, since the time needed for the SF_6 leak trace to reach the QEPAS sensor would exceed several tens of seconds. Note that, leak-test station operations do not necessarily require QEPAS spectral scans. Leaks detection can be also performed by kept fixed the laser wavelength on the selected SF_6 absorption line and measure the QEPAS signal evolution versus time.

Figure 2.24 depicts a comparison of the QEPAS leak detector performance obtained in this investigation with other reported gas leak-detection methods sensitivities in the literature [24-27].

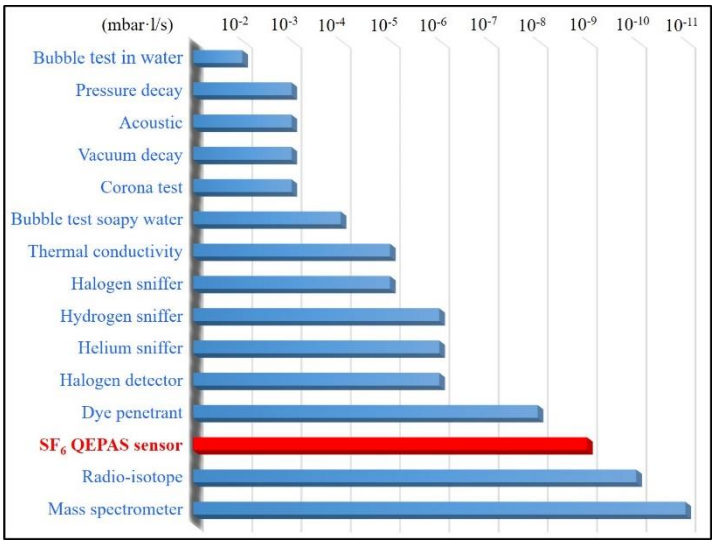

Figure 2.24 Sensitivity ranges in mbar·l/s of the main leak detection methods.

Our optical leak station is competitive with state-of-the-art techniques, reaching sensitivity level obtainable only with radioisotope and mass spectroscopy systems, and with the advantages of lower cost, compact size and weight, faster response time and not requiring radioactive materials.

References

[1] J. A. Harrington, *Infrared Fibers and Their Applications*, SPIE, 2004.

[2] R. Nubling and J. A. Harrington, Launch conditions and mode coupling in hollow glass waveguides, Opt. Eng. 37 (1998) 2454.

[3] C. M. Bledt, J. E. Melazer, and J. A. Harrington, Theoretical and experimental investigation of infrared properties of tapered silver/silver halide-coated hollow waveguides, Appl. Optics 52 (2013) 3703.

[4] C. M. Bledt, J. A. Harrington, and J. M. Kriesel, Loss and modal properties of Ag/AgI hollow glass waveguides, Appl. Opt. 51 (2012) 3114.

[5] A. Sampaolo, P. Patimisco, J. M. Kriesel, F. K. Tittel, G. Scamarcio, and V. Spagnolo, Single mode operation with mid-IR hollow fibers in the range 5.1-10.5 μm, Opt. Express 23 (2015) 195.

[6] M. Siciliani de Cumis, S. Viciani, S. Borri, P. Patimisco, A. Sampaolo, G. Scamarcio, P. De Natale, F. D'Amato, and V. Spagnolo, Widely-tunable mid-infrared fiber-coupled quartz-enhanced photoacoustic sensor for environmental monitoring, Opt. Express 22 (2014) 28222.

[7] V. Spagnolo, P. Patimisco, S. Borri, G. Scamarcio, B. E. Bernacki, and J. Kriesel, J. Mid-infrared fiber-coupled QCL-QEPAS sensor, Appl. Phys. B 112 (2013) 25.

[8] E. A. J. Marcantili and R. A. Schmeltzer, Hollow metallic and dielectric waveguides for long distance optical transmission and lasers, Bell Syst. Tech. J. 43 (1964) 1783.

[9] Y. Matsuura and M. Miyagi, Hollow optical fibers for ultraviolet and vacuum ultraviolet light, IEEE J. Sel. Top. Quant. 10 (2004) 1430.

[10] C. Dragone, Attenuation and radiation characteristics of the HE11 mode, IEEE T. Microw. Theory 28 (1980) 704.

[11] M. Miyagi and S. Kawakami, Design theory of dielectric-coated circular metallic waveguides for infrared transmission, J. Lightwave Technol. 2 (1984) 116.

[12] R. George and J. A. Harrington, Infrared transmissive, hollow plastic waveguides with inner Ag-Agl coatings, Appl. Opt. 44 (2005) 6449.

[13] P. Patimisco, A. Sampaolo, L. Mihai, M. Giglio, J. Kriesel, D. Sporea, G. Scamarcio, F. K. Tittel, and V. Spagnolo, Low-Loss Coupling of Quantum Cascade Lasers into Hollow-Core Waveguides with Single-Mode Output in the 3.7–7.6 μm Spectral Range, Sensors 16 (2016) 533.

[14] P. Patimisco, V. Spagnolo, M.S. Vitiello, A. Tredicucci, G. Scamarcio, C.M. Bledt, J.A. Harrington, Coupling external cavity mid-IR quantum cascade lasers with low loss hollow metallic/dielectric waveguides. Appl. Phys. B 108 (2012) 255–260.

[15] P. Patimisco, V. Spagnolo, M.S. Vitiello, A. Tredicucci, G. Scamarcio, C.M. Bledt, J.A. Harrington, Low-Loss Hollow Waveguide Fibers for Mid-Infrared Quantum Cascade Laser Sensing Applications. Sensors 13 (2013) 1329–1340.

[16] P. Patimisco, A. Sampaolo, M. Giglio, J. M. Kriesel, F. K. Tittel, and V. Spagnolo, Hollow core waveguide as mid-infrared laser modal beam filter, J. Appl. Phys. 118 (2015) 113102.

[17] M. Giglio, P. Patimisco, A. Sampaolo, J. M. Kriesel, F. K. Tittel, and V. Spagnolo, Low-loss and single-mode tapered hollow-core waveguides optically coupled with interband and quantum cascade lasers, Opt. Eng., 57 (2018) 011004.

[18] M. Maiss, and C.A.M. Brenninkmeijer, Atmospheric SF6: trends, sources, and prospects. Environ. Sci. Technol. 32, 20 (1998) 3077-3086.

[19] V. Spagnolo, P. Patimisco, S. Borri, G. Scamarcio, B. E. Bernacki, and J. Kriesel, Part-per-trillion level SF_6 detection using a quartz enhanced photoacoustic spectroscopy-based sensor with single-mode fiber-coupled quantum cascade laser excitation, Opt. Lett. 37 (2012) 4461.

[20] H. R. Carlon, Infrared absorption coefficients (3–15 μm) for sulfur hexafluoride (SF_6) and Freon (CCl_2F_2), Appl. Opt. 18 (1979) 1474–1475.

[21] D. M. Cox and A. Gnauk, Continuous wave CO_2 laser spectroscopy of SF_6, WF_6 and UF_6, J. Mol. Spectrosc. 81 (1980) 205–215.

[22] Available online: http://www.hitran.com

[23] P. Patimisco, G. Scamarcio, F.K. Tittel, V. Spagnolo, Quartz-Enhanced Photoacoustic Spectroscopy: A Review, Sensors 14 (2014), 6165-6205.

[24] A. Roth, Vacuum Technology (Elsevier Science Publishers, 1990).

[25] J.F. O'Hanlon, An Users Guide to Vacuum Technology (John Wiley & Sons, 1989).

[26] J.M. Lafferty, Foundations of Vacuum Science and Technology (John Wiley & Sons, 1998).

[27] A. Pregelj, M. Drab, M. Mozetic, Leak Detection Methods and Defining the Sizes of Leaks, 4th International Conference of Slovenian Society for Nondestructive Testing - Ljubljana, Slovenia (1997).

Chapter 3
Custom quartz tuning forks for quartz-enhanced photoacoustic spectroscopy

Apart from timing and frequency stabilization applications, QTF crystals are employed as electro-acoustic transducers in quartz-enhanced photoacoustic spectroscopy (QEPAS). Since 2002, for more than 10 years, QEPAS sensors implemented as acoustic resonators QTFs usually used in clocks and wristwatches, optimized to maintain a selected resonance frequency (typically 2^{15} Hz ~ 32.7 kHz) in a wide temperature range. However, the relatively high resonance frequency and the small dimension of such *standard* 32 kHz QTFs can limit their sensing applications, impeding the detection of slow relaxing gases or exhibiting non-zero background noise due to fraction of laser light hitting the prongs. These issues paved the way for design and realization of custom QTFs optimized for QEPAS applications. By properly selecting the prong geometrical parameters, the first resonance mode can be lowered down to less than 3 kHz while keeping the quality-factor high. As a consequence, the laser modulation matching the QTF resonance frequency allows slow gases to relax the excess thermal energy after each modulation pulse. Moreover, by reducing the frequency of the first resonance mode, also third resonance mode can be exploited for QEPAS.

In this chapter, a detailed study on the influence of QTFs size and geometry on their resonance frequencies and related quality factor is dealt with. Resonators operated both at the first and at the third flexural mode are investigated, with an experimental validation supporting the theoretical model. Several examples of custom QTF-based QEPAS sensors will be presented and discussed.

3.1 Quartz tuning forks vibrating at in plane first flexural mode

A QTF acoustic resonator can be modelled as two vibrating homogenous cantilevers connected at one end to the support. In the first demonstration of on-beam QEPAS, the

standard QTF vibrates at its first flexural mode, usually referred to as fundamental mode. When vibrating at the fundamental in-plane flexural mode, the QTF prongs bend symmetrically respect to the QTF longitudinal axis. This mechanical deformation causes a stress field generated along the prongs. The simulations of the QTF prongs deformation and the stress field generated along the prongs performed by employing COMSOL MultiPhysics are shown in Fig. 3.1.

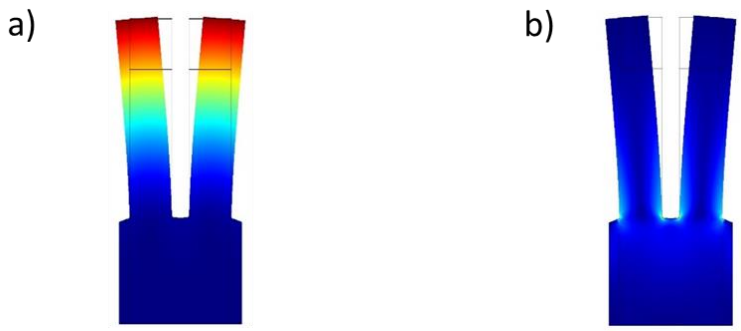

Figure 3.1 COMSOL MultiPhysics simulation of the displacement (a) and the stress field (b) of a QTF vibrating at the fundamental mode.

Each prong can be represented by a single point-mass on the prong tip, having effective mass m_e corresponding to about 1/4 of the mass of one of the prongs [1,2]. The mechanics of the prong oscillation can be thus described as the dynamics of an effective harmonic oscillator with mass m_e located at the top (1/4) of the prong. As the bound end, the basis of the prong exhibits the most intense stress field when the prong oscillates, as shown in Fig. 3.1(b). Since quartz is a piezoelectric material, a mechanical stress can be converted to an electrical signal and vice versa. In terms of elastic modelling, each prong can be described as a single harmonic oscillator, neglecting the coupling with the other one. For small amplitude oscillations, the motion of each prong can be described using a one-dimensional model and the resonance frequencies in vacuum are given by [3]:

$$f_{n,vac} = \frac{\pi T}{8\sqrt{12}\,L_p^{\,2}}\sqrt{\frac{E}{\rho}}\nu_n^2\,, \tag{3.1}$$

where ρ = 2650 kg/m^3 is the density of quartz, E = 72 GPa is the component of the quartz Young's modulus in the vibrating plane of the QTF. The sizes L_p and T are

shown in Fig. 3.2, $\nu_{n=0} = 1.194$ for the lowest flexural mode of oscillation (fundamental mode) and $\nu_{n=1} = 2.988$ for the first overtone mode.

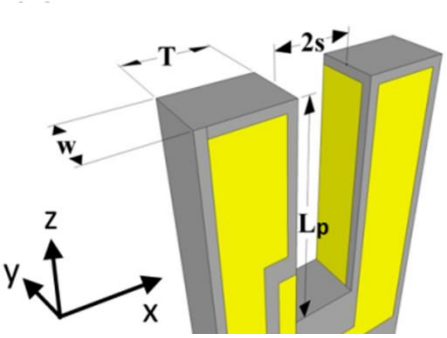

Figure 3.2 Schematic view of QTF dimensions (a).

In the fundamental mode, each prong vibrates with an antinode at the tip and a node at the QTF base. The average absorbed power is maximum at the fundamental frequency f_0 given by:

$$f_0 = \frac{1}{2\pi}\sqrt{\frac{k_0}{m_e}}, \tag{3.2}$$

where $m_e = 0.24267\rho L_p T w$ [4] is the effective mass of one prong and w is the prong thickness (see Fig. 3.2). The spring constant (or stiffness) k_0 of the fundamental mode of a prong is determined by its geometrical parameters and Young modulus as [5]:

$$k_0 = 0.2575\frac{T^3 w E}{L_p^{\,3}}. \tag{3.3}$$

It is convenient to introduce a QTF quality factor, Q, defined as the ratio of f_0 to the full width at half-maximum (FWHM) value of the resonance curve Δf. Due to the quartz piezoelectric effect, vibrations of the prongs create a current proportional to the speed of the prong top $I(t) = a \cdot dx/dt$, where the proportionality constant a, also called fork constant, is given by [6]:

$$a = 3d_{11}E\frac{Tw}{L_p} \tag{3.4}$$

where $d_{11} = 2.31 \cdot 10^{-12}$ m/V or C/N is the longitudinal piezoelectric modulus of quartz. The QTF can be modelled both as a mechanical oscillator and as an RLC circuit, the relations between mechanical and electric characteristics being given by: $R = 2m_e\Delta f/a^2$, $L = 2m_e/a^2$ and $C = a^2/2k_0$ [7]. Accordingly, the fork constant can be rewritten as:

$$a = \sqrt{\frac{2m_e\Delta f}{R}}. \tag{3.5}$$

The QTF current can be written as $I(t) = I_a sin(2\pi ft) + I_b cos(2\pi ft)$, where I_a and I_b are the in-phase and out-of-phase current components, respectively, which are both functions of the driving frequency f [7]:

$$I_a = \frac{I_M (\Delta f)^2 f^2}{(\Delta f)^2 f^2 + \left(f^2 - f_{0,vac}^2\right)^2},$$

$$I_b = \frac{f I_M \Delta f \left(f^2 - f_{0,vac}^2\right)}{(\Delta f)^2 f^2 + \left(f^2 - f_{0,vac}^2\right)^2} \quad (3.6)$$

where I_M is the maximum current value at the resonant frequency $f_{0,vac}$.

3.1.1 Design and electrical characterization of QTFs for model validation

With the aim of determining the dependence of the QTF parameters and performance on their relevant dimensions and identifying the optimal design for optoacoustic gas sensing, a set of QTFs with different values of spacing between the prongs, their length and thickness, and crystal thickness were designed and realized [8]. The schematics of the designed custom QTFs, together with the standard QTF, are shown in Fig. 3.3.

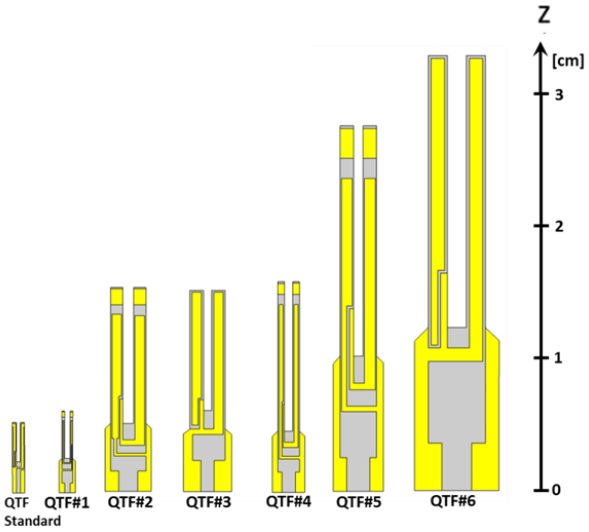

Figure 3.3 Schematic x-z plane view of standard and custom designed tuning forks.

A z-cut quartz wafer with a 2° rotation along the x-axis, which provides stable frequency at room temperature, was selected for the realization of the custom QTFs. The z-cut is the dominant low frequency (up to 50 KHz) crystal-cut, which provides

thermally stable flexural vibrational modes frequencies. Standard photolithographic techniques were used to etch the QTFs. Cr and Au patterns are photolithographically defined on both sides of the wafer. A three-dimensional crystal structure is generated by chemical etching in a hydrogen fluoride solution, and finally side electrodes are applied by means of shadow masks. The gap between center electrode and side electrode is 50 µm. A photograph of the realized custom QTFs is shown in Fig. 3.4.

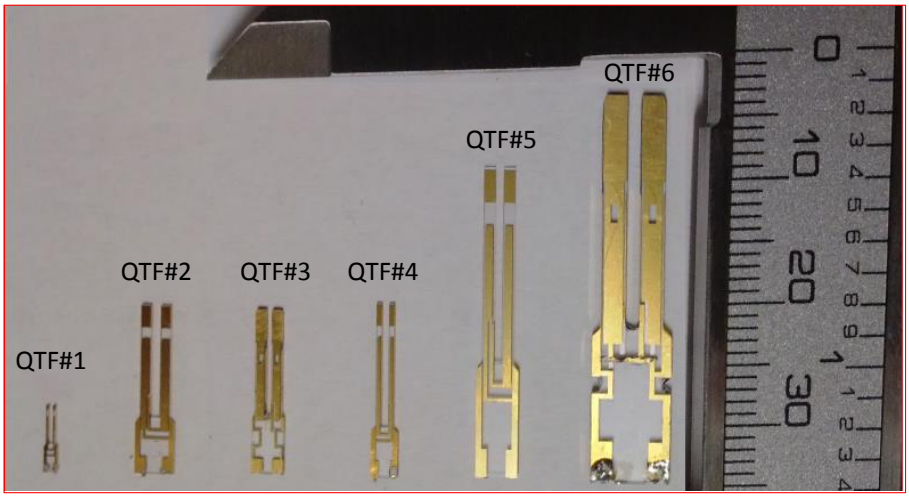

Figure 3.4 Picture showing the produced custom tuning forks. The size scale in mm is shown on the right.

The dimensions and the prongs' effective mass of the investigated QTFs are listed in Table 3.1

Table 3.1 Dimensions and prong effective mass m_e of the standard and custom tuning forks: L_p (QTF prong length), T (thickness of the prong), w (thickness of the quartz crystal) and $2s$ (spacing between prongs).

Parameters	QTF standard	QTF #1	QTF #2	QTF #3	QTF #4	QTF #5	QTF #6
L_p (mm)	3.0	3.5	10.0	10.0	11.0	17.0	20.0
w (mm)	0.34	0.25	0.25	0.5	0.25	0.25	0.8
T (mm)	0.35	0.2	0.9	1.0	0.5	1.0	1.4
2s (mm)	0.3	0.4	0.8	0.5	0.6	0.7	1
m_e (mg)	0.230	0.113	1.447	3.216	0.884	2.733	12.102

The electrodes geometry defines the way in which the deformation occurs when an electric field is applied. In our case, the electric field is applied along the x-axis of the QTFs (see Fig. 3.2).

The geometry of the golden pattern deposited on the QTF also defines the way how the charges due to crystal deformation are collected. For the set of custom QTFs shown in Fig. 3.3, two patterns for the electrodes were employed. For QTF#3 and QTF#6 the same gold pattern of the QTF standard was used, while for the remaining QTFs the gold pattern was slightly modified in order to collect charges generated in all internal side wafer surfaces when the QTFs vibrate at the fundamental flexural mode. The two designs for the gold contact pattern, both enhancing the first fundamental flexural mode, are shown in Fig. 3.5.

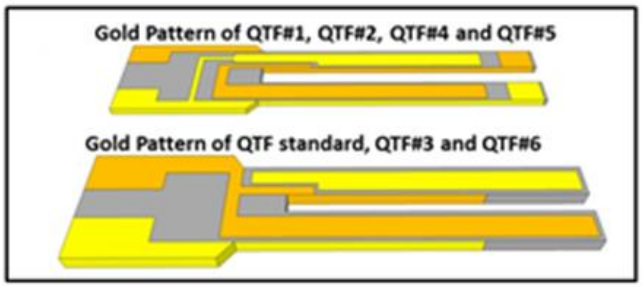

Figure 3.5 Surface and side view of the two different designed gold patterns for electrical charge collection. The grey areas stand for uncovered quartz, while the yellow and gold-yellow area represent the two electrodes of each pattern.

The electro-elastic properties of the set of QTFs shown in Fig. 3.4 were determined by using the experimental setup depicted in Fig. 3.6.

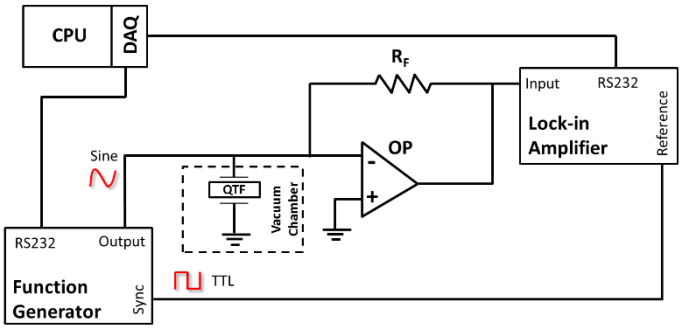

Figure 3.6 Circuit diagram for QTF characterization. The excitation sine voltage is supplied by a high-resolution waveform generator, which also provides the reference TTL signal for the lock-in amplifier. The QTF current output is converted to a voltage by means of a transimpedance amplifier with a feedback resistor of R_F = 10 MΩ. The QTF is mounted inside a vacuum chamber allowing low gas pressure measurements. OP: operational amplifier.

A function generator (Tektronix model AFG3102) with a resolution of 2 mHz was used to provide a sinusoidal voltage to the QTFs. The in-phase (I_a) and out-of-phase (I_b) components of the current pass through a current-to-voltage converter using an operational amplifier. The output voltage is measured by a lock-in amplifier (Stanford Research Model SR830). To determine the resonance properties of the QTFs, the frequency of the function generator was varied and processed by the lock-in output via a data acquisition (DAQ) card and a computer (CPU). The QTFs resonance curves were fitted using Eq. (3.6) to determine I_M, f_0 and Δf. The frequency responses of the investigated QTFs, obtained at a pressure of 50 Torr in standard air and with an excitation voltage level of V_0 = 0.5 mV are shown in Fig. 3.7. For each QTF, both the experimental in-phase (I_a) and out-of-phase (I_b) components were measured and the related best fit were obtained by using Eq. (3.6).

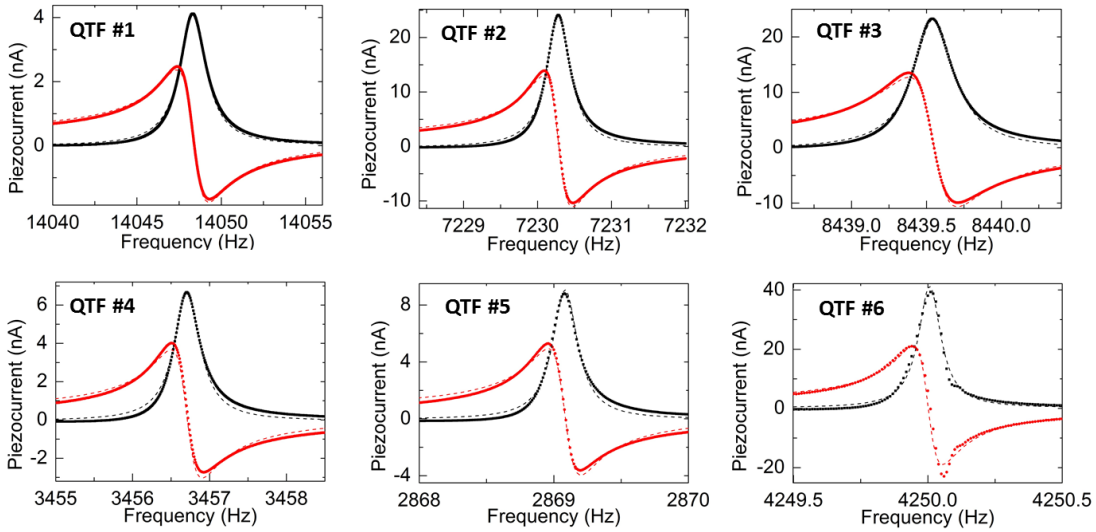

Figure 3.7 Resonance curves for in-phase I_a (black dots) and out-of-phase I_b (red dots) components of the QTF current measured at a fixed excitation level V_0 = 0.5 mV and at a pressure of 50 Torr in standard air for custom QTFs near the fundamental oscillation mode. The dashed lines indicate the best-fit curves using Eq. (3.6).

The small left-right asymmetry for I_a with respect to the curve peak and the different asymptotic values for I_b are due to parasitic currents caused by stray capacitance between the two pins of the QTF, which dominated away from the resonance frequency. From the data of Fig. 3.7 the resonance frequency of the fundamental flexural mode $f_0^{(exp)}$, the current amplitude I_M at the resonant frequency, the FWHM of the resonant curve Δf, the quality factor Q and the spring constants ($k_0^{(exp)}$) were extracted by using Eq. (3.2). In Table 3.2 the obtained parameters are reported, together with the

corresponding theoretical resonant frequencies $f_{0,vac}$ and spring constants (k_0), calculated for vacuum condition by using Eq. (3.1) and Eq. (3.3), respectively.

Table 3.2 Experimental and calculated physical parameters for the investigated QTFs: $f_0^{(exp)}$ (resonance frequency of the fundamental oscillation mode), Δf (the full width at half-maximum value of the QTF resonance curve), Q (quality factor) and $k_0^{(exp)}$ (QTF spring constant of the fundamental oscillation mode). The calculated $f_{0,vac}$ and k_0 are also listed.

	$f_0^{(exp)}$ (Hz)	$f_{0,vac}$ (Hz)	Δf (Hz)	Q	$k_0^{(exp)}$ (N/m)	k_0 (N/m)
QTF standard	32762.84	32743.61	2.02	16206.63	9720.01	9718.33
QTF #1	14049.20	13746.59	1.89	7323.49	838.81	839.65
QTF #2	7230.27	7577.81	0.39	18654.18	3277.21	3280.50
QTF #3	8439.51	8419.79	0.54	25484.95	9033.05	9000.00
QTF #4	3456.69	3479.25	0.41	8388.12	422.19	422.61
QTF #5	2869.07	2913.42	0.24	11901.88	914.76	915.94
QTF #6	4250.01	4176.48	0.11	37712.74	8620.62	8333.33

A good agreement between the experimental and theoretical f_0 and k_0 values was obtained, confirming that these two parameters can be predicted with good accuracy. The small discrepancies (< 5%) between experimental and theoretical values are due to the damping of the gas, additional weight of the electrode gold layers, dependence of the elasticity modulus of quartz on the crystallographic axes' orientation and deviations in geometry between the modelled and the real QTFs [3]. From the resonance characteristics measured as a function of the excitation voltage amplitude V_0, it is possible to determine the electrical resistance $R = V_0/I_M$, since at resonance the QTF performs as a pure resistor. The measured I_M versus V_0 are shown in Fig. 3.8.

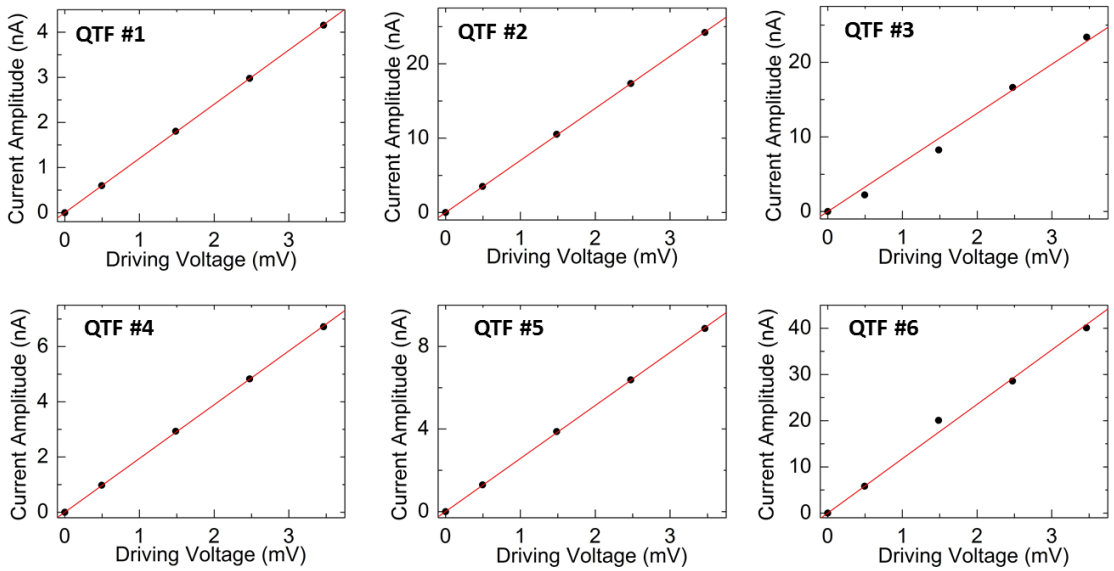

Figure 3.8 Results of the peak current amplitude I_M (black dots) at the QTF resonance frequency f_0 of the fundamental oscillation mode as a function of the applied voltage, for QTF#1-6. The solid lines are the best linear fits.

The resistance R was extracted from a linear fit of the QTF electrical characteristics. From these data the QTF fork constant $a^{(exp)}$ was estimated by using Eq. (3.5) and compared the results with the theoretical values $a^{(theo)}$ calculated by using Eq. (3.4). In addition, the capacitance $C = 1/(2\pi Q R f_0^{(exp)})$ and inductance $L = QR/(2\pi f_0^{(exp)})$ can be calculated. The results are listed in Table 3.3.

Table 3.3 Measured electro-elastic parameters for standard and custom QTFs: R (QTF electrical resistance), $a^{(exp)}$ (fork constant), C (electrical capacitance) and L (electrical inductance). Calculated fork constant values $a^{(theo)}$ are also listed.

	R (kΩ)	$a^{(exp)}$ (μC/m)	$a^{(theo)}$ (μC/m)	C (fF)	L (kH)
QTF standard	79.70	19.79	17.11	3.76	6.28
QTF #1	831.86	7.128	3.61	1.86	69.05
QTF #2	142.78	11.23	14.05	8.27	58.66
QTF #3	151.87	24.95	24.08	4.88	73.02
QTF #4	513.49	5.67	5.97	10.70	198.42
QTF #5	389.01	7.34	9.23	11.99	256.97
QTF #6	84.93	33.87	28.15	11.70	120.01

Theoretically, R is related to geometrical parameters, since R ~ $L_p^2/W\sqrt{T}$ [9], measured R values vs $L_p^2/W\sqrt{T}$ are reported and in Fig. 3.9.

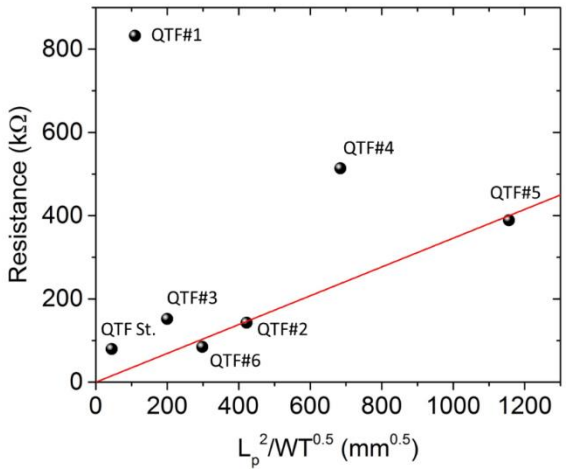

Figure 3.9 Dependence of the QTF resistance (black dots) versus the ratio $L_p^2/w\sqrt{T}$. QTF St. is the QTF standard. The red solid curve is the best linear fit considering only the QTF standard (QTF St.) and QTF#2,3,5,6, using the function $R=n\cdot L_p^2/w\sqrt{T}$, with n= 0.346 kΩ/√mm.

As expected, a linear correlation is observed, except for QTF#1 and QTF#4. However, in an actual device other factors contribute to determine the electrical resistance, such as the generated charge collection efficiency determined by the gold contacts QTF pattern. The large *R*-values for QTF#1 and QTF#4 could be attributed to a reduced gold coverage of the prongs (< 50% for QTF#1 and <75% for QTF#4) and consequently a reduced charge collection and consequently a reduced I_M. Consistently, a good agreement (within 20% discrepancy) was obtained between experimental and theoretical QTF fork constant values, except for QTF#1 and QTF#4, where a 50% difference can be attributed to an overestimation of *R*.

The *Q*-factor was determined by the two main losses mechanisms, extrinsic and intrinsic. The extrinsic losses are due to interactions with the surrounding medium, while the intrinsic losses include different contributions, i.e. support losses (interactions with its support structure), surface and volume losses and thermo-elastic losses. All these loss contributions can be theoretically estimated [10]. The calculated Q-factor values may significantly differ from the actual ones due to additional factors such as processing anisotropy, crystal quality and gold patterning. However, comparing the measured Q-factor versus the fork constant (see Fig. 3.10), a proportionality is evident.

This result indicates the feasibility to empirically predict the Q-factor from a calculation of the fork constant *a*.

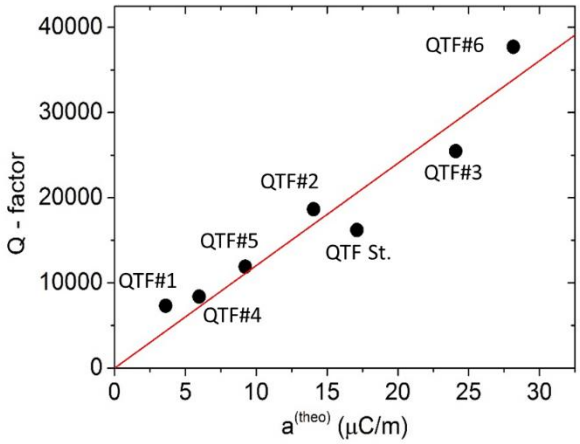

Figure 3.10 Dependence of the QTF quality factor *Q* (black dots) versus the theoretical fork constant $a^{(theo)}$ values. The red solid curve is the best linear fit, using the function $Q=m\cdot a$, with $m=$ 1203 m/μC.

Under vacuum conditions, no gas damping phenomena are present, while when the QTF operates in a viscous fluid, the effective mass increases and the resonance frequency decreases. The complete mechanical, electrical and hydro-dynamical model of the tuning fork is described in detail in Ref. [3]. The resonance frequency scales linearly with the pressure *P* of the surrounding gas as:

$$f_0 = f_{0,vac} - k_p P \tag{3.7}$$

where $k_p = f_{0,vac}\cdot u/(2\rho_g wT)$, *u* is the added mass due to the presence of a fluid and ρ_g is the fluid density. In addition, fluid damping reduces the resonance quality factor *Q*, since the reaction force due to the presence of the gas acts on the vibrating body and causes energy dissipation. A fluid damping parameter can be introduced, which is proportional to the density ρ_g and the viscosity η of the fluid. Assuming that $P \propto \rho_g$ and η does not noticeably change with *P*, the influence of the fluid damping on *Q* can be expressed in terms of the energy loss *1/Q(P)* at the gas pressure *P*, and *Q(P)* can be defined as:

$$Q(P) = \frac{Q_0}{1 + Q_0 b P^c} \tag{3.8}$$

where Q_0 is the quality factor of the QTF under vacuum, including all the intrinsic losses mechanisms, and *b* and *c* are parameters related to the QTF geometry and

surrounding fluid viscosity. In fact, QTFs are used for density, viscosity and velocity measurement of fluids [7,11]. In order to investigate the damping effects induced by the environmental gas (air in our experiments) on the quality factor and the resonant frequency, the in-phase I_a and out-of-phase dispersion component I_b of the QTF output current were measured, at a fixed excitation level, V_0 = 0.5 mV, as a function of the air pressure (see Fig. 3.11).

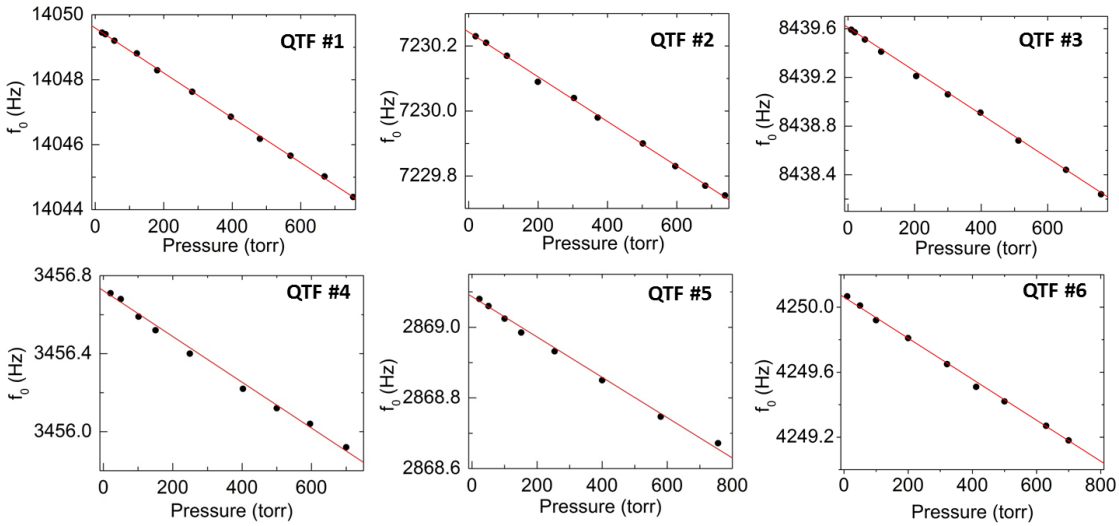

Figure 3.11 QTF resonance frequency f_0 (black dots) measured as a function of the standard air pressure for all six custom QTFs. Red solid lines are the linear fit of the data. The related slopes are reported in Table 3.4.

According to Eq. (3.7), f_0 shows a linear dependence from the gas pressure in the investigated range of pressures (10 Torr - 760 Torr). The intercept with the vertical axis yields the resonant frequency $f_{0,vac}$. Similarly, the quality factor as a function of the pressure for all the investigated custom QTFs and the best fit obtained by using Eq. (3.8) are reported in Fig. 3.12.

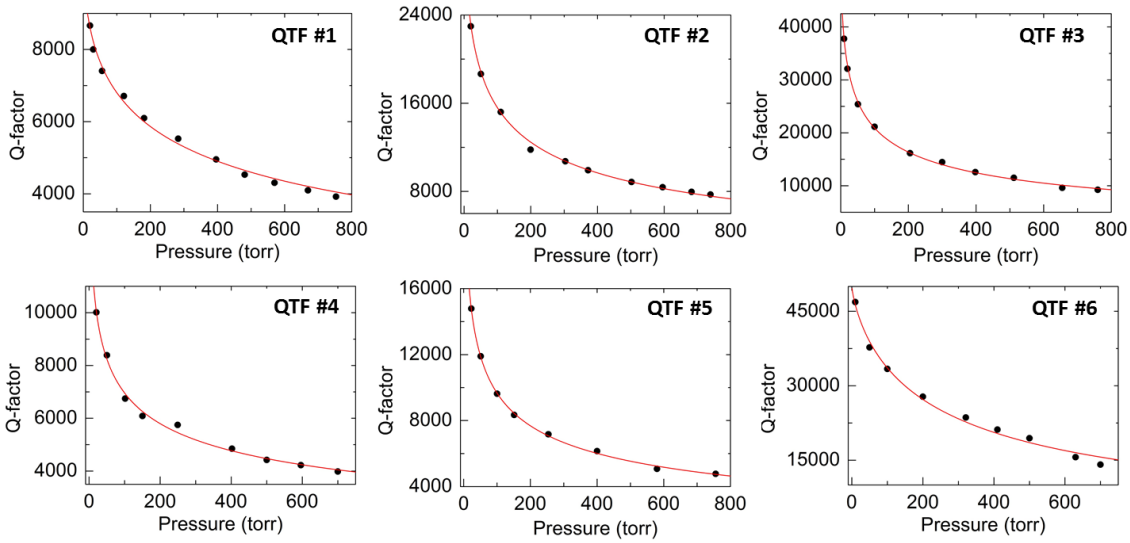

Figure 3.12 Quality factor *Q* (black dots) measured as a function of the standard air pressure for the six custom QTFs. Red solid curves are the best fit obtained using Eq. (3.8). The related fit parameters are reported in Table 3.4.

The *Q*-factor shows a large pressure dependence, as predicted, and rapidly decreases with gas pressure. The parameters obtained by the fitting procedures are listed in Table 3.4.

Table 3.4 Values extracted from the best fits of the dependence of the resonance frequency (see Fig. 3.11) and the quality factor (see Fig. 3.12) of the fundamental flexural mode from the surrounding gas pressure, for the six custom QTFs. The values obtained for the standard QTF are also reported.

	$f_{0,vac}$ (Hz)	k_p (mHz/torr)	Q_0	b ($torr^{-0.5}$)	c
QTF standard	32763.31	9.26	88718.69	8.02×10^{-5}	0.47
QTF #1	14049.60	6.93	10862.49	5.17×10^{-5}	0.51
QTF #2	7230.24	0.69	36563.52	3.31×10^{-5}	0.52
QTF #3	8439.61	1.78	47020.06	2.68×10^{-5}	0.53
QTF #4	3456.72	1.17	23282.04	1.89×10^{-5}	0.36
QTF #5	2869.09	0.57	34800.37	9.82×10^{-6}	0.44
QTF #6	4250.06	1.26	50129.89	2.80×10^{-7}	0.77

3.1.2 QTF#5 implementation in a Terahertz QEPAS sensor for methanol detection

The realization of custom-made QTFs, with larger prong spacing respect to the standard QTF, made possible the extension of QEPAS in the Terahertz (THz) range (3 cm^{-1} - 200 cm^{-1} or 0.1 - 6 THz). Since the standard QTF prongs spacing is comparable with the wavelength of THz sources, larger size QTFs are mandatory to operate in the THz range, to allow beam focusing between the QTF prongs without illuminating them. Terahertz (THz) research applies in an increasingly wide variety of applications, such as information and communications technology, medical sciences, global environmental monitoring, homeland security, quality and process controls. Many harmful gases, explosives, narcotics and toxic gases, as hydrogen cyanide, hydrogen sulfide, methanol, ammonia, hydrogen fluoride, hydroxide, hydrogen peroxide, have spectral absorption "fingerprints" in this range, due to rotational-translational transitions between molecular energetic levels. Such transitions are strong and up to three order of magnitude faster with respect to vibrational-translational, mid-IR transitions. THz spectroscopy is thus particularly suitable for the QEPAS technique. Indeed, the fast relaxation times characteristic of THz transitions allow low-pressure operation, providing high QTF resonance Q-factors, and thereby large QEPAS signals [12]. Moreover, QEPAS permits overcoming some issues traditionally associated with THz spectroscopy, such as the use of cryogenic systems for the detection of THz radiation and complex signal analysis processes.

In this section a QEPAS THz sensor targeting a methanol (CH_3OH) absorption line falling at 3.93 THz and having a line-strength of 4.28×10^{-21} cm/mol is reported. Methanol is widely used as a solvent, detergent, or even denaturant additive for industrial ethanol, and its ingestion can be fatal due to its toxicity. The employed custom QTF is the QTF #5 as reported in Section 3.1.2, operated at the fundamental flexural resonance mode.

The CH_3OH QEPAS sensor scheme is depicted in Fig. 3.13. A single-mode 250 μm wide, 1.5mm long bound-to continuum Fabry-Perot QCL fabricated in a single plasmon configuration and emitting at 3.93 THz (76.3 μm), mounted on the cold finger of a continuous-flow cryostat equipped with polymethylpentene (TPX) windows (~ 70%

transmission) and kept at a heat sink temperature of 6K, while driven in CW mode, was employed.

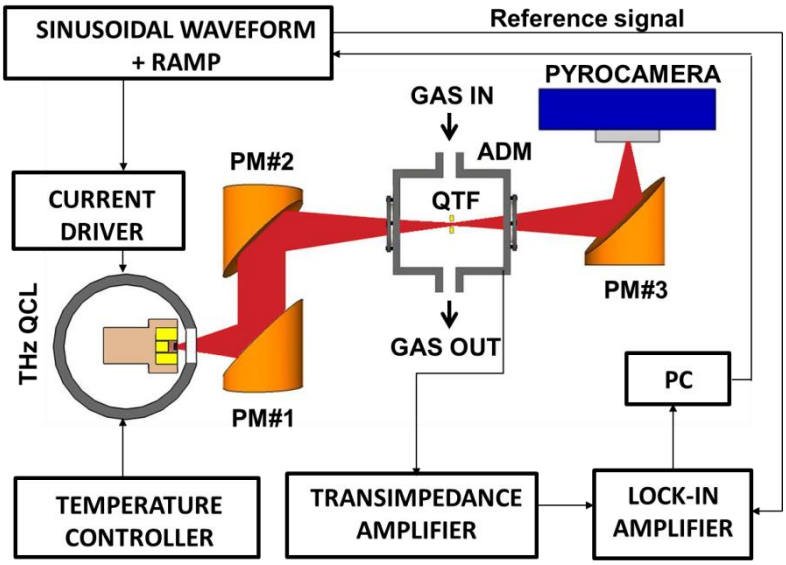

Figure 3.13 Schematic of the QEPAS trace gas sensor using a THz Quantum Cascade Laser (THz QCL) as the excitation source. PM – Parabolic Mirror; ADM – Acoustic Detection Module; QTF – Quartz Tuning Fork; PC – Personal Computer.

The THz laser beam was focused between the QTF prongs by using two off-axis paraboloidal aluminum reflectors (PM#1 with f-number = 2 and PM#2 with f-number = 5). The QTF is fixed on a mounting structure and housed in an acoustic detection module (ADM), with TPX input and output windows. An optical power of 40 μW was measured between the prongs of the QTF by means of a pyroelectric detector. The THz laser beam exiting the ADM was re-focused onto the Spiricon pyroelectric camera by means of an additional aluminum parabolic mirror (PM#3 with f-number = 2). QEPAS measurements were performed by applying a sinusoidal waveform provided by a function generator (Tektronix model AFG3102) at the QTF fundamental resonance frequency f_0 (2869.09 Hz) to the current driver while demodulating the QTF response at f_0 by using a lock-in amplifier (Stanford Research Model SR830). Both instruments were controlled by LabView-based software. A slow voltage ramp allows scanning of the THz laser wavelength through the selected methanol absorption line for spectral line-shape acquisition.

Figure 3.14 depicts the observed 2D laser beam profiles after mirror PM#3. First the profile is measured with the focused laser beam positioned out of the QTF (Fig. 3.14(a))

and then between the QTF prongs (Fig. 3.14(b)). A comparison between the two beam profiles clearly indicated that the THz beam is not blocked by the QTF, when it is focused between its prongs. The total image intensity was measured by summing all pixel values for both beam profiles, from which it was estimated that 96.4% of the light intensity passes between the prongs. Hence, a prong spacing of 2s = 700 μm should not significantly affect the noise level of the QEPAS signal.

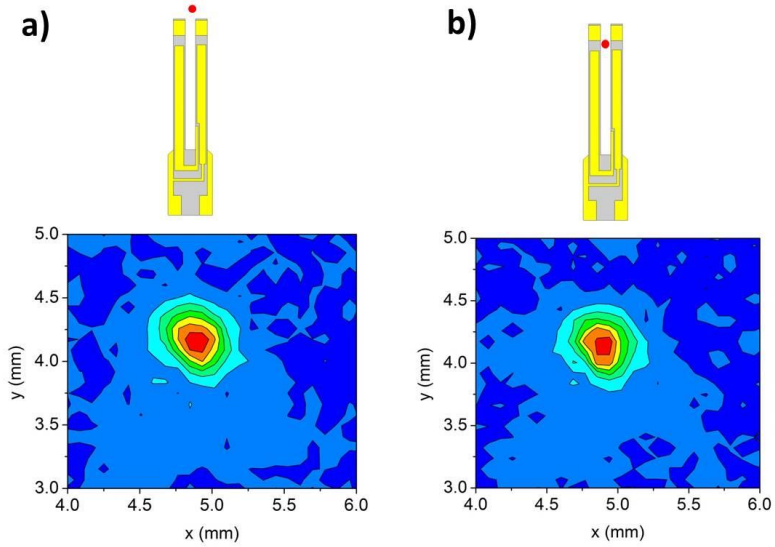

Figure 3.14 Two-dimensional beam profile of the THz-QCL acquired by means of an IR pyrocamera after mirror PM#3 (see Fig. 3.13) when the beam is focused out the QTF (a) or between the two prongs (b). Both beam profiles are shown together with an illustration representing the position of the focused THz beam (red spot) with respect the QTF.

The sensor calibration was performed by using a trace gas standard generator. Starting from a certified 100 part per million (ppm) CH_3OH in N_2 mixture, lower methanol concentrations were produced using pure N_2 as the diluting gas. A laser modulation amplitude of 600 mV was employed in the QEPAS experiments. High-resolution QEPAS scans of a CH_3OH:N_2 calibrated mixtures with different concentrations are shown in Fig. 3.15(a), together with a spectral scan acquired when pure N_2 flows inside the ADM. The lock-in integration time was set to 3 seconds for all measurements.

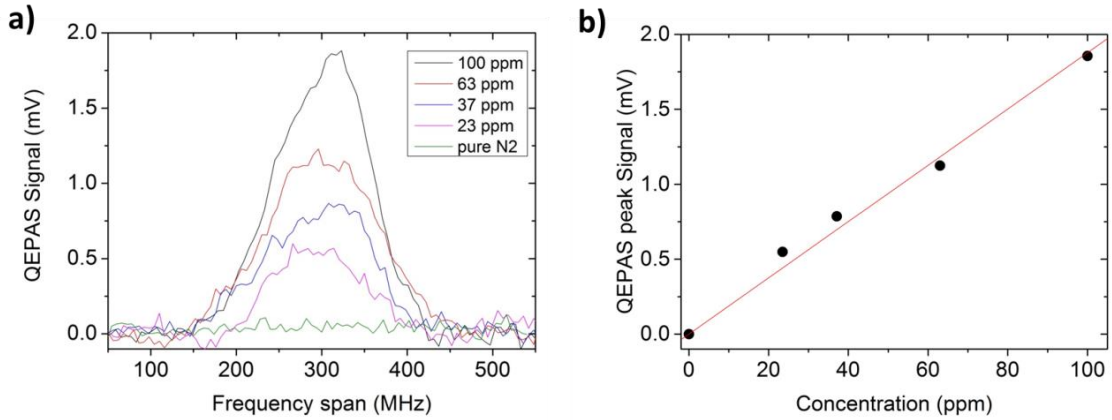

Figure 3.15 QEPAS spectral scans of gas mixture containing different concentrations of methanol in N_2 at gas pressure of 10 Torr acquired with 3 seconds lock-in integration time (a). The spectral scan obtained for pure N_2 under the same operating conditions is also depicted. Calibration curve (solid red line) obtained from the linear fit of measured QEPAS peak signals (black dots) vs methanol concentrations (b).

The calibration curve shown in Fig. 3.15(b) was obtained using CH_3OH concentrations derived from the gas mixture generator and the QEPAS peak signals acquired from the related scans. These results confirm that the QEPAS signal is proportional to the methanol concentration. The noise fluctuations (1σ-value) are ±30μV, corresponding to a 1-σ minimum detection limit (MDL) of 1.7 ppm at 3 seconds lock-in integration time. An Allan-Werle variance analysis (see Appendix) was performed in order to determine the best achievable sensitivity of the THz QEPAS sensor. The QEPAS signal at zero CH_3OH concentration (pure N_2 at 10 Torr) was measured and averaged and the obtained the Allan-Werle deviation in ppm is shown in Fig. 3.16.

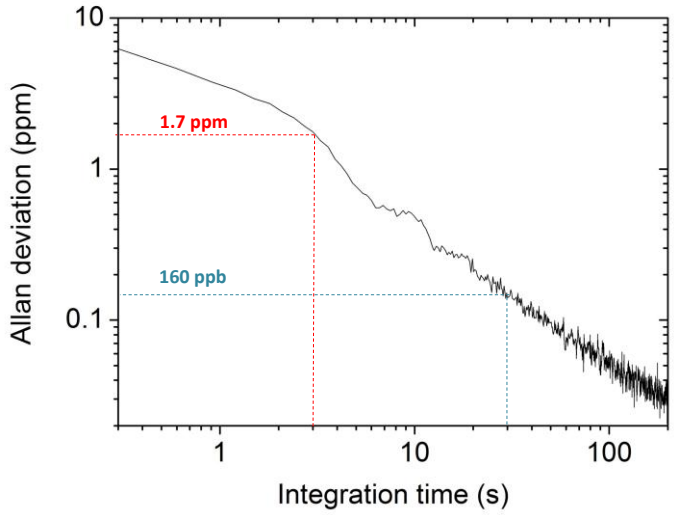

Figure 3.16 Allan-Werle deviation in ppm as a function of the lock-in integration time for the QEPAS sensor. The curve was calculated by analyzing 120 minutes-long acquisition periods of the signal measured for pure N_2 at 10 Torr and setting the lock-in integration time at 100 ms.

For a 30 seconds averaging time, a detection sensitivity of 160 part per billion (ppb), corresponding to a NNEA=3.75 · 10^{-11} $cm^{-1}W/Hz^{½}$ was achieved, which represents a new record value for QEPAS trace gas sensing. These results clearly demonstrate that the QTF geometry provides better sensor system performances with respect to the standard geometry. An even higher sensitivity can be expected by increasing the QTF crystal thickness w; however, chemical etching for crystal of w > 1 mm cannot guarantee sharp edge profiles.

3.1.3 New geometries custom QTFs

The dependence of the resonance frequency and related quality factor on the QTF relevant dimensions has been investigated in Section 3.1.2. This study showed that resonance frequencies of in-plane flexural modes can be well predicted by using the Euler-Bernoulli equation, leading to a dependence $f_n \propto T/L^2$ as reported in Eq. (3.1). The Q-factor depends on all the energy dissipation mechanisms occurring in a vibrating prong of a QTF. The main contributions are due to damping by the surrounding fluid, the interaction of the prong with its support and thermo-elastic damping [13]. For the fundamental mode, the support losses can be neglected and the overall quality factor can be phenomenologically related to the prong sizes as $Q = 3.78 \cdot 10^5$ wT/L.

Therefore, the overall quality factor of the fundamental mode can be increased by reducing the prong length and increasing both thickness and crystal width. However, the resonance frequency of the fundamental flexural mode, which increases as the ratio between the prong thickness and its squared length, must not exceed the non-radiative gas absorption relaxation rates.

When the crystal thickness is fixed, the quality factor scales linearly as the ratio T/L and the quality factor becomes $Q = 9.45 \cdot 10^4$ T/L, for w = 0.25 mm, at atmospheric pressure. A MATLAB-based software was realized to relate the quality factor and the resonance frequency at different prong geometries. For each fixed prong geometry (T, L), the software calculates the resonance frequency and the related Q-factor, and plots ordered points on the x- (frequencies, f) and y- (Q-factors) axis of the coordinate plane. By

ranging L from 3 mm to 20 mm and T from 0.2 mm to 3.0 mm, while keeping at a fixed w = 0.25 mm value, the calculated ordered points (Q, f) are shown in Fig. 3.17.

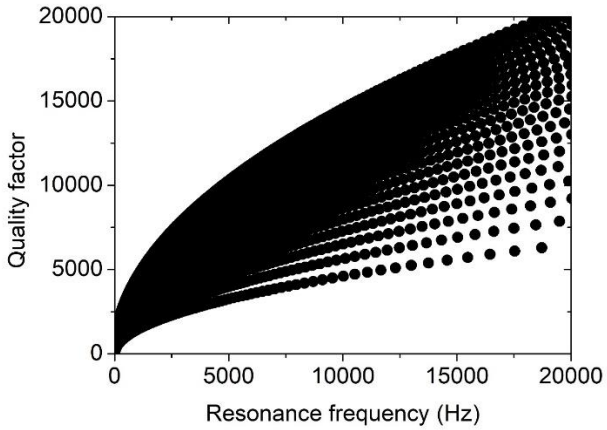

Figure 3.17 Q-factor values plotted as a function of the resonance frequency for different prong lengths and thicknesses of quartz tuning fork of crystal width w = 0.25 mm, at atmospheric pressure.

The graph clearly shows that for a selected resonance frequency, different prong sizes can be chosen, providing quality factors values spanning in a certain range. Moving to low resonance frequencies, this range of possible quality factor values, as well as the Q-factor values itself, is reduced. In particular, QTFs with a resonance frequency lower than 10 kHz cannot ensure a Q-factor higher than 15,000, at atmospheric pressure. For a novel generation of QTFs optimized for QEPAS operation, a resonance frequency of ~16 kHz (a half of the standard 32.7 kHz) was selected. At f = 16 kHz, L and T values (with w = 0.25 mm) maximizing the quality factor (18,000) are 9.4 mm and 2.0 mm, respectively. In a first step, starting with this prong geometry two QTFs differing only in the prong spacing were designed: QTF-S08 having a prong spacing of 0.8 mm, and QTF-S15 with a prong spacing of 1.5 mm. With all other geometrical parameters being identical, a comparison between them in terms of QEPAS performance will allow establishing the influence of the prong spacing on the QTF frequency and Q-factor, as well as on the amount of radiation incident on the prong surface, which typical affects the QEPAS sensor noise level.

Starting from this design, two novel geometries will be proposed: one with T-shaped prongs to optimize the strain field between the prongs and their support and the other one having prongs with grooves carved on the central sides in order to reduce the QTF electrical resistance.

As described in Section 1.2, when QTF prongs are vibrating at a resonance mode frequency, the stress produced along the prong induces a local polarization of quartz and charges appearing on its surface. The polarization depends on the stress field by the quartz piezoelectric tensor, thus an increase of the amplitude of the stress field produces an increase of the piezoelectrically induced charges, and subsequently an enhancement of the QTF current signal. There are no analytical models to predict the intensity distribution of the stress field along QTF prongs when the prong deformation is caused by the fundamental flexural mode. For this reason, commercial finite element software COMSOL Multiphysics was used to simulate the QTF geometry and to estimate the stress field distribution along prong. With QTF prong sizes L = 9.4 mm and T = 2.0 mm (and w = 0.25 mm), the obtained stress field distribution is shown in Fig. 3.18(a).

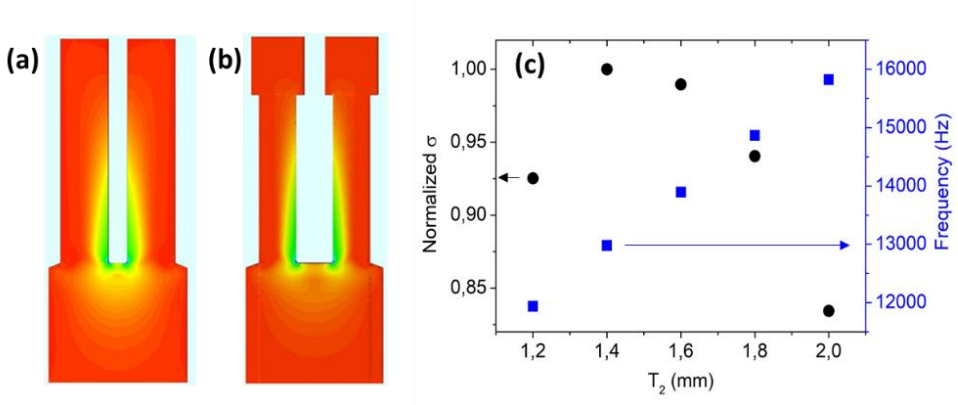

Figure 3.18 Stress field distribution for QTF-S08 (a) and QTF-S08-T (b) simulated by using COMSOL MultiPhysics. (c) Normalized stress field intensity σ (●) and resonance frequency (■) as a function of T2 for QTF-S08-T.

The stress field is mainly localized at the junction between the prong base and the QTF support and extends in the support area. When a QTF operated at the fundamental mode is used in a QEPAS sensor, prong deformation results from a stress field induced by pressure waves hitting close to the prongs top. If the prong mass is lowered to the end of the prong connected to the support, a change of the stress field distribution is expected. Starting from these considerations, a modified geometry for QTF prongs is proposed, in which the prong thickness T is not constant along the prong axis. The thickness function T(z) of the prong is thought out to be a piecewise function that can be written as:

$$T(z) = \begin{cases} T_1 & z \in [0, L_0] \\ T_2 & z \in [L_0, L_1] \end{cases} \tag{3.9}$$

where the origin of the axis is set at the top of the prong and the axis is orient downwards. This prong geometry will be referred as a T-shaped prong. Starting from the prong geometry defined in the previous section (T_1 = 2 mm, L = 9.4 mm and w = 0.25 mm), L_0 was determined by considering the effective mass (which is an estimation of the effective vibrating mass for a prong at the fundamental mode), resulting in about 1/4 of the mass of one of the prongs [1,2], i.e. $L_0 = L/4$ = 2.4 mm. T_2 was determined by using COMSOL Multiphysics, spanning T_2 from 2.0 mm to 1.2 mm as a function of the stress field intensity. The obtained results are reported in Fig. 3.18(c). T_2 = 1.4 mm was found to be the prong thickness value maximizing the stress field intensity. The related stress field distribution is shown in Fig. 3.18(b). The simulation shows that the T-shape results in a better distribution of the stress field associated with the vibration along the internal prong surface, where the generated charges are collected, when performing QEPAS experiments. A decrease of the resonance frequency of the fundamental mode is also predicted, as depicted on the right y-axis in Fig. 3.18(c). The realized modified QTF geometry with T-shaped prong has dimensions of T_1 = 2.0 mm, T_2 = 1.4 mm, L_0 = 2.4 mm and L_1 = 9.4 and will be named hereafter as QTF-S08-T.

As deduced from Fig. 3.17, when the resonance frequency is reduced, the quality factor is also negatively affected. A reduction of the quality factor involves an increase of the electrical resistance [8, 9]. To keep the electrical resistance low, the coupling between the electrodes and the resonance mode must be optimized. This can be achieved by carving rectangular grooves on both surfaces of each prong of QTF-S08. Depositing the central electrodes on the carved surfaces provides an increase of the piezoelectric coupling and at the same time a decrease of the equivalent electrical resistance, representing the loss parameter in the equivalent conventional resonator circuit. All these modifications do not affect the resonator quality factor. The QTF-S08 with grooves applied on both prongs is schematically shown in Fig. 3.19 and will be named hereafter as QTF-S08-G.

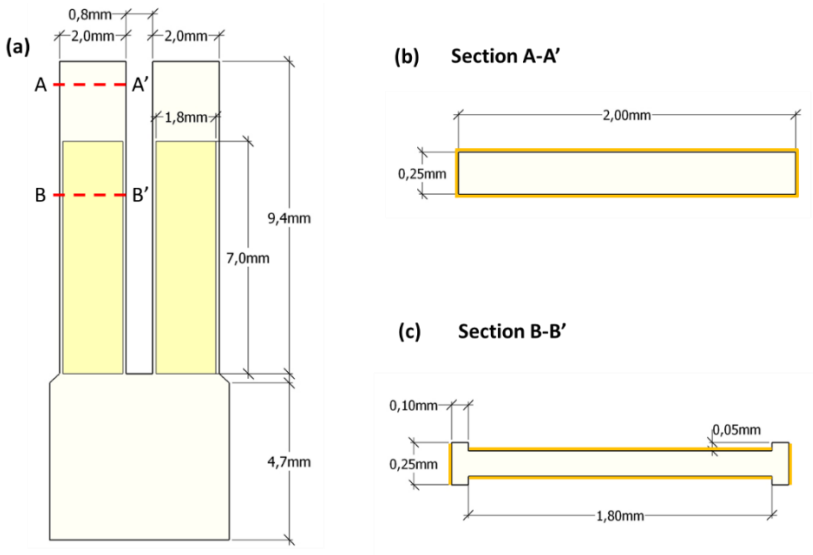

Figure 3.19 (a) Front view with sizes of the QTF-S08-G. Dark yellow areas represents grooves applied on both sides of QTF prongs. (b) Cross-section of QTF-S08-G prongs along AA'. (c) Cross-section of the QTF-S08-G prongs along BB'.

These grooves were realized by carving 50 µm of the upper and lower crystal surfaces and the width of the areas placed between the grooves and the lateral edges of the prong was fixed to 100 µm, so that the resonator maintains a good mechanical resistance and sufficient stiffness. The carved area corresponds to 40% of the total crystal thickness.

The electrical characterization of this new generation of QTFs (QTF-S08, QTF-S08-T, QTF-S08-G and QTF-S15) has been performed by employing a setup similar to the one shown in Fig. 3.6. The spectral responses of the new generation of QTFs, at atmospheric pressure in air, are shown in Fig. 3.20.

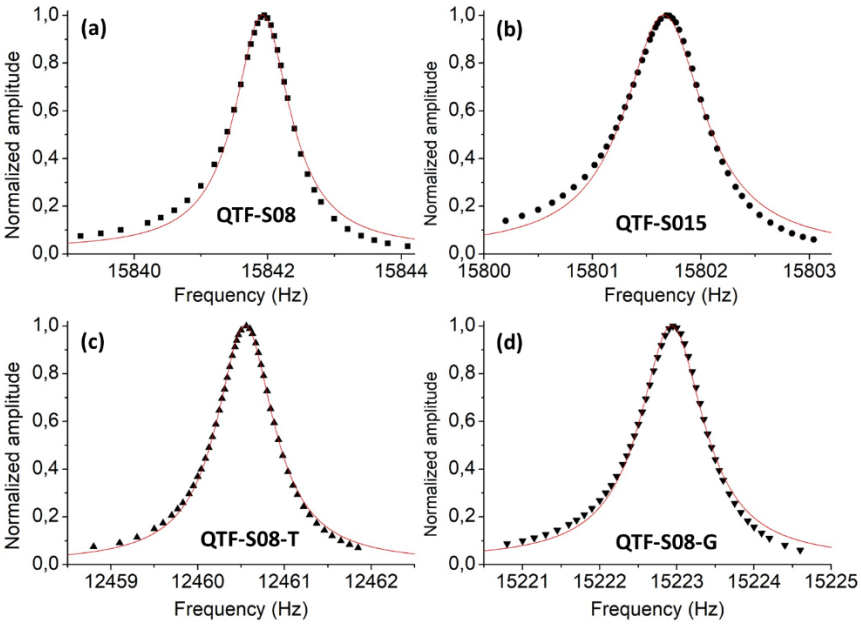

Figure 3.20 Resonance curves of (a) QTF-S08 (■), (b) QTF-S015 (●), (c) QTF-S08-T (▲) and (c) QTF-S08-G (▼) measured at a fixed excitation level V_0= 0.5 mV at atmospheric pressure in standard air near the fundamental oscillation mode. The red solid lines indicate the best Lorentzian fit.

The small left-right asymmetry for in-phase components with respect to the curve peak are due to parasitic currents caused by stray capacitance between the two pins of the QTF, which dominated away from the resonance frequency [14]. In Table 3.5, resonance frequencies, Q-factors and electrical resistance values of the investigated QTFs are compared with the standard 32.7 kHz-QTF values.

Table 3.5 Resonance frequencies (f_0), quality factors (Q) and electrical resistance (R) of QTF-S08, QTF-S08-G, QTF-S08-T, QTF-S15 and standard 32.7 kHz-QTF.

QTF	f_0 (Hz)	Q	R (kΩ)
QTF-S08	15841.92	15710	162.8
QTF-S15	15801.66	15400	141.7
QTF-S08-T	12460.55	15540	157.5
QTF-S08-G	15222.93	15050	104.3
32 kHz-QTF	32760.83	13690	94.6

QTF-S08 and QTF-S15 share the same geometrical characteristics for each prong and differ only in the spacing between the prongs. The small difference in the measured

resonance frequencies implies that the prong spacing does not affect the resonance properties of the QTF and thereby the two prongs can be considered almost uncoupled. QTF-S08 and QTF-S15 also share almost the same Q-factor value (15,710 and 15,400, respectively), about 13% different from the predicted value of ~ 18,000. This means that the combination between the Euler-Bernoulli model and the empirical dependence of the quality factor with prong width/length ratio is an efficient tool for the prediction of the quality factor values. Even if the resonance frequency of both QTF-S08 and QTF-S15 is almost a half of the standard 32.7 kHz-QTF, higher quality factors were measured. QTF-S08-G showed a resonance frequency about 4% lower than QTF-S08. Although the Euler-Bernoulli model does not predict a dependence of the resonance frequency on the crystal thickness w, 50 μm-grooves carving on both surfaces slightly affects the rectangular geometry of the prong and produces a small shift of the resonance frequency. For QTF-S08-T, a lower resonance frequency was measured with respect to QTF-S08 and QTF-S15, as predicted by COMSOL simulations, due to the non-uniformity of the moments of inertia along the prong section. For QTF-S08-T, a quality factor of 15,260 was measured. Although the prong T-geometry leads to a decrease of the prong width from 2 mm to 1.4 mm starting from 2.4 mm far from prong top, the quality factor was not affected. T-shaping the prongs does not affect the electrical resistance, being nearly identical the electrical resistance measured for QTF-S08 and QTF-S08-T. While, a comparison of QTF-S08 and QTF-S08-G, clearly demonstrates that adding grooves on the prongs surfaces reduces the electrical resistance from 162.9 kΩ (QTF-S08) to 104.3 kΩ (QTF-S08-G), while Q-factor and resonance frequency are only slightly affected and thereby an improvement in terms of the QEPAS performance is expected.

To verify all assumptions, we employed all QTFs in the QEPAS setup, depicted in Fig. 3.21.

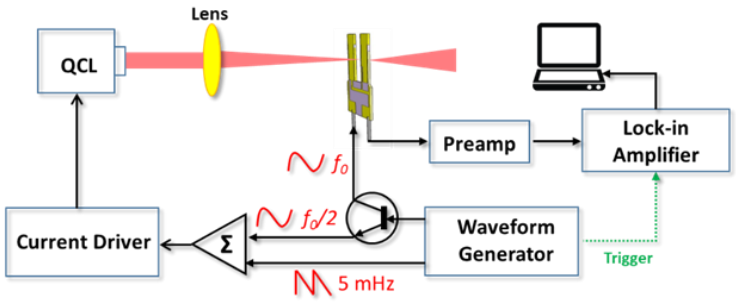

Figure 3.21 Schematic of the QEPAS trace gas sensor system using a quantum cascade laser as the excitation source.

A single-mode continuous-wave quantum cascade laser (QCL) was used as the excitation source to generate photoacoustic signals. The QCL targeted a water vapor absorption line falling at 1297.19 cm^{-1}, having intensity of $3.6 \cdot 10^{-22}$ cm/molecule [15]. The laser beam was focused between the QTF prongs using a ZnSe lens with a focal length of 50 mm. An aluminum enclosure equipped with two mid-IR AR-coated windows was realized in order to accommodate and easily switch the QTFs. The housing was filled by standard air with a fixed 1.7% water vapor concentration at atmospheric pressure. The QEPAS sensor operated with a wavelength modulation and dual-frequency detection approach, i.e. the laser beam is wavelength-modulated at a half of the selected resonance frequency ($f_0/2$) while the lock-in amplifier demodulates the QTF signal at the resonance frequency f_0. The absorption line is acquired by applying a slow ramp to the current driver allowing a linear wavelength-scan. For all QTFs, the laser focus position maximizing the QEPAS signal was experimentally found to be 2 mm far from the QTF top, between the two prongs. The QEPAS spectral scans of the selected water vapor absorption line obtained for the new generation QTFs, all operating at the fundamental mode, are shown in Fig. 3.22.

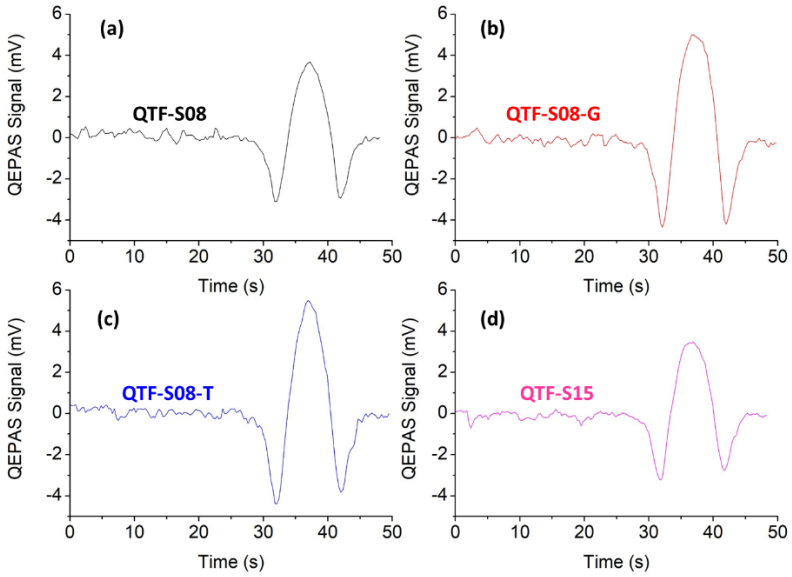

Figure 3.22 QEPAS spectral scans of 1.7% water concentration in air for the fundamental flexural mode of QTF-S08 (a), QTF-S08-G (b), QTF-S08-T (c) and QTF-S15 (d). All scans were recorded with a 100 ms lock-in integration time.

The largest QEPAS signal was measured with the QTF-S08-T (5.48 mV), about 1.5 times higher than that measured with QTF-S08. The T-shaped prong designed starting from a rectangular prong provided two advantages: i) a reduction of the resonance frequency with no influence on the quality factor; ii) an increase of the stress field along the prongs lateral surface, leading to an increase of collected piezoelectric charges. Both advantages are beneficial for QEPAS sensor performance. QTF-S08 provides a QEPAS signal ~ 6% higher than QTF-S15. This means that even if the electro-elastic properties of QTFs are not influenced by the prong spacing, this parameter can influence the acousto-electric transduction efficiency, i.e., the conversion efficiency of the amplitude of the acoustic wave in piezoelectric charge production. The larger is the prong spacing the lower is the sound wave intensity hitting the internal surface of the prong. QTF-S08-G showed a QEPAS signal 1.36 times higher than QTF-S08, demonstrating that even if the grooves on the prong surface slightly affect the resonance frequency and the Q-factor, a decrease of the electrical resistance is more beneficial in terms QEPAS performance. In the graphs shown in Fig. 3.22, the range between 0 s and 24 s is free from absorption features. Hence, this range was used for the estimation of the 1σ noise level for all four QTFs. The 1σ noise level measured for all bare new generation QTFs was ~ 0.26 mV, for both prong spacings of 0.8 mm (QTF-S08, QTF-S08-T, QTF-S08-G) and 1.5 mm (QTF-S15), demonstrating that a prong spacing of 0.8 mm is large enough to ensure that a negligible portion of light hits the internal surface of prongs. A standard 32.7 kHz-QTF was also tested with the same experimental conditions. The laser beam was focused 0.6 mm far from the top for standard 32.7 kHz-QTF. The most important parameter to compare different QEPAS sensors is the signal-to-noise ratio (SNR) defined as the ratio between the QEPAS peak signal and 1σ fluctuations of the signal in a spectral range (i.e. laser current range) where no optical absorptions are detected. In Fig. 3.23, a comparison between the investigated QTFs, together with standard 32.7 kHz-QTF, is shown in terms of the QEPAS SNR.

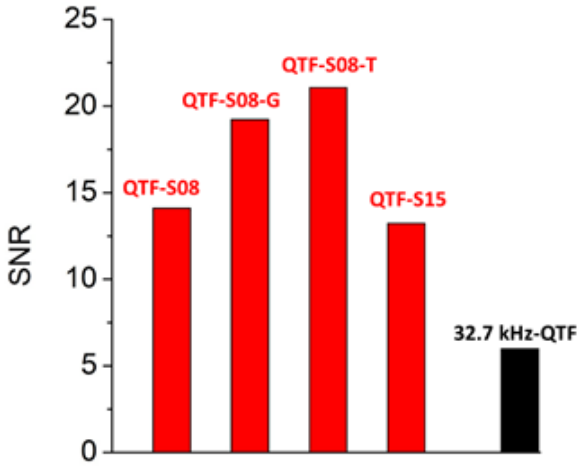

Figure 3.23 SNR of QTF-S08, QTF-S08-G, QTF-S08-T and QTF-S15 (red bars) compared with that acquired for standard 32.7 KHz-QTF (black bar).

All new generation QTFs showed the highest SNR values with respect to the standard 32.7 kHz-QTF, the latter showing also the highest noise level (9.4 times higher than the new generation QTFs) due to its small prong spacing of 0.3 mm. In particular, QTF-S08-T provides the highest QEPAS SNR. Hence, it is an excellent candidate for the realization of a spectrophone for QEPAS sensors.

The geometrical parameters influencing the sensor performance are: the internal diameter and the length of the two tubes, together with the spacing between the tube and the surface of the QTF. The first parameter to be optimized is the distance between the tubes and the internal surface of the prong. Two tubes having a length of 13.3 mm and internal diameter of 1.52 mm were placed at different distances from the prongs, spanning from 70 μm to 2.0 mm. The QEPAS peak signal measured as a function of the tube-QTF distance is plotted in Fig. 3.24.

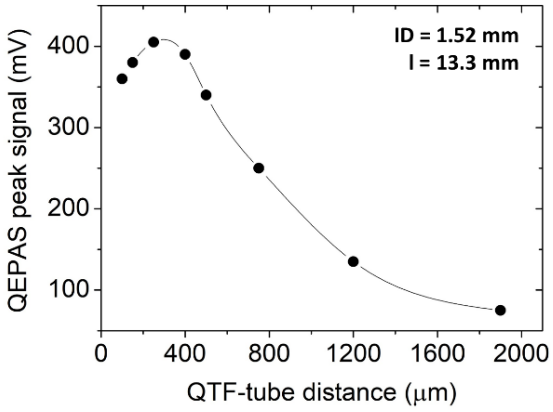

Figure 3.24 QEPAS peak signal as a function of the distance between the tube and the QTF. Solid lines serve as convenient visual guides.

The distance between QTF and tubes maximizing the SNR is 200 µm. However, in the range 150 µm - 300 µm, the QEPAS signal varies by less than 7%. The QEPAS signal approaches asymptotically that achieved with the bare QTF when the distance between the tubes and the QTF becomes larger than 2000 µm and rapidly increases when this distance is reduced, confirming that the shorter the QTF-tube distance the higher is the acoustical coupling between them. When the distance is shorter than 120 µm, the SNR decreases because of damping effects generated by the short distance between the tube and the QTF. The length of two tubes is correlated with the sound wavelength at the QTF resonance frequency (λ = 27.6 mm) [16,17] and has value between $\lambda/4$ (l = 6.9 mm) and $\lambda/2$ (l = 13.8 mm). Hence, tubes having lengths in this range, i.e., 10 mm, 11 mm, 12.4 mm, 13 mm, 14 mm and 15 mm were tested. The choice of the optimal ID is related to the QTF prongs spacing. When the tube diameter is larger than the prongs spacing, the gap between two tubes becomes less important and the tubes are well acoustically coupled with the QTF. When the tube diameter becomes comparable with the prongs spacing, the acoustic coupling between tubes and QTF decreases. In addition, for small tube diameters a photothermal noise contribution to the QEPAS signal can arise, due to portion of the laser beam touching parts of the spectrophone. For this reason, tubes with IDs < 1 mm have not been taken into account. Hence, six different tubes with internal diameters ID = 1.36 mm, 1.41 mm, 1.52 mm, 1.59 mm, 1.83 mm and 2.06 mm have been investigated. As representatives, in Fig. 3.25, the QEPAS peak values are plotted as a function of the tube lengths, for ID = 1.41 mm (Fig. 3.25(a)), 1.59 mm (Fig. 3.25(b)) and 2.06 mm (Fig. 3.25(c)).

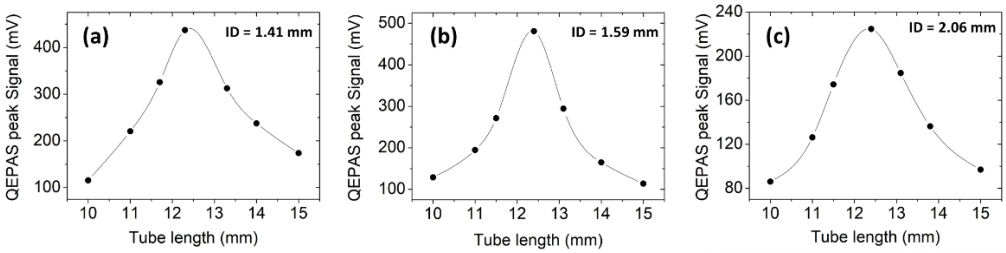

Figure 3.25 QEPAS peak signals measured with three different spectrophones employing acoustic resonator tubes with an ID = 1.41 mm (a), 1.59 mm (b) and 2.06 mm (c) as a function of the tube length. Solid lines serve as convenient visual guides.

For all internal diameters investigated, the QEPAS signal is maximized when the tube length is l = 12.4 mm and rapidly decreases when a shorter or longer length is used.

This result allows to affirm that the optimal tube length is not dependent from its internal diameter. The internal diameter maximizing the QEPAS signal is ID = 1.59 mm. With the optimal tube geometry (ID = 1.59 mm and l = 12.4 mm), the 1σ noise level results in 0.38 mV, ~1.5 times higher than the value measured for the bare QTF-S08-T. This can be attributed to a small fraction of light hitting the internal surface of tubes. The 1σ noise levels were similar for all spectrophone configurations investigated, within a discrepancy below 5 %. The tubes having l = 12.4 mm and ID = 1.59 mm showed the highest SNR of ~1380, as well as the highest QEPAS peak signal (480.8 mV). The QEPAS scan of the water absorption line measured with this spectrophone is shown in Fig. 3.26(a). The SNR values obtained with the spectrophone system have to be compared with the SNR of the bare QTF. SNR Enhancement (SNR_E) was defined as the ratio between the SNR measured for the bare QTF and the SNR measured for the QTF coupled with the micro-resonator. In Fig. 3.26(b), the SNR_E as a function of the internal diameter for tubes having l = 12.4 mm is reported. Starting from the highest value, the SNR_E rapidly decreases when moving to lower inner diameter while the decrease is less pronounced when higher inner diameters are employed.

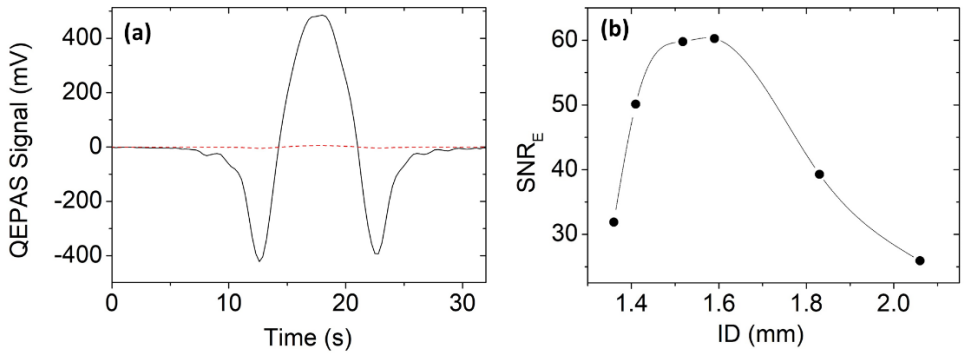

Figure 3.26 (a) QEPAS spectral scan of water absorption line acquired with the bare QTF-S08-T (dashed red line) and with a spectrophone composed by QTF-S08-T and a pair of micro-resonator tubes having a length of 12.4 mm and internal diameter of 1.59 mm, both positioned 200 μm far from the QTF (solid black line). (b) Signal-to-noise ratio enhancement (SNR_E) of the spectrophone with respect to the bare QTF as a function of tubes internal diameter when the tube length is 12.4 mm. The solid line is a visual guide.

With QTF-S08-T a signal-to-noise ratio enhancement of ~60 was obtained, which is a new record for mid-IR QEPAS spectroscopy [18].

3.2 Quartz tuning forks vibrating at in plane third flexural mode

The results shown in the previous sections suggest that QEPAS sensors with improved sensitivity can be developed by employing custom QTFs having increased prong spacing compared to the standard 32 kHz and providing higher signal-to-noise ratio values. Moreover, compared to the standard 32 kHz QTF, custom QTFs can be designed in order to reduce the resonance frequency of the fundamental mode down to a few kHz, thus approaching the typical energy relaxation time of the targeted gases [19]. In Sections 3.1.1, 3.1.2 and 3.1.4 it was demonstrated that lowering the fundamental mode resonance frequency causes a decrease of the related quality factor. Therefore, a trade-off optimization of the above parameters must be found. However, it is worth to notice that lowering the fundamental resonance frequency reduces also the overtone frequencies. These observations led the way to an investigation of QTF higher-order flexural modes for QEPAS trace gas sensing.

As described in Section 1.2, the only vibrational modes employed in QEPAS based sensor systems are the flexural antisymmetric modes, in which the two prongs oscillate in antiphase in the z-x plane (see Fig. 3.2).

A simulation of the deformation of the QTF prongs vibrating at the third flexural mode (usually referred to as first overtone mode) and of the generated stress field along the prong is shown in Fig. 3.27.

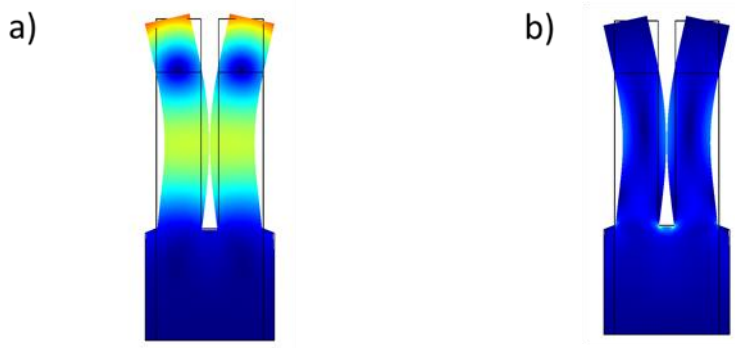

Figure 3.27 COMSOL MultiPhysics simulation of the displacement (a) and the stress field (b) of a QTF vibrating at the first overtone flexural mode.

Based on Eq. (3.1), the third flexural mode is ~ 6.25 times higher than the first flexural mode (usually referred to as fundamental mode), being $\nu_{n=0}$ = 1.194 and $\nu_{n=1}$ = 2.988, respectively. Therefore, lowering the fundamental resonance frequency can allow overtone frequencies $f_{\nu n=1} << 1/2\pi\tau$, where τ is the typical gas non-radiative relaxation time. In particular, QTFs #2, #4, #5 and #6 could satisfy this requirement. These observations lead the way to an investigation of QTF overtone flexural modes for QEPAS trace gas sensing.

In the next sections, a theoretical model for the quality factor of QTFs operated at the first overtone will be presented, followed by an experimental validation of the model. A new gold pattern optimized for the first overtone flexural mode charge collection will be described.

For each QTF mentioned above, an example of QEPAS sensor exploiting the first overtone performance will be showed.

3.2.1 Theoretical model for the quality factor of QTFs operated at the third flexural mode

Two main loss mechanisms, extrinsic and intrinsic contribute to the determination of the quality factor of a resonance mode. The extrinsic losses are due to interactions with the surrounding medium [20-22]. The intrinsic losses include support losses (localized in the junction area between prongs and their support base), surface, volume [23,24] and thermo-elastic losses [25]. Each loss contribution is independent from the others, but all occur simultaneously for a vibrating QTF prong, resulting in an overall Q-factor:

$$Q = \left(\frac{1}{Q_{air}} + \frac{1}{Q_{supp}} + \frac{1}{Q_{tel}}\right)^{-1} \tag{3.10}$$

where Q_{air}, Q_{supp} and Q_{tel} are the quality factors related to fluid damping, support losses and thermo-elastic losses, respectively. The influence of these contributions depends on the prong size and on the vibrational dynamics of the selected resonance mode, since each vibrational mode is characterized by different distributions of its effective mass [26]. In other words, each vibrational mode is expected to exhibit a different quality factor.

The fundamental in-plane flexural mode can be represented by a single point-mass on the prong tip. Therefore, the support losses can be neglected and the overall Q-factor is determined by the quality factor related to fluid damping (Q_{air}), which can be related to the QTF geometrical parameters by Q_{air0}~wT/L, as experimentally demonstrated in details in Section 3.1.2. For the first overtone mode, the quality factor associated with the air damping Q_{air_1} can be assumed proportional to the inverse of the damping ratio β_1 [20] and turns out to depend on the geometrical parameters as [27]:

$$Q_{air_1} \propto \frac{1}{\beta_1} \propto \frac{T^{\frac{3}{2}}}{L} \tag{3.11}$$

The nth-overtone can be considered as a system of n-coupled point-masses subsystems, each located at an antinode. The overtone mode shape presents a uniform distribution of point-masses along the prong, resulting in a high stress on the QTF support. For a single cantilever beam $Q_{supp} \sim A_n (L/T)^3$, with A_n coefficients depending on the resonance mode number and the prong material. Hao et al. estimated A_0 = 2.081 for the fundamental mode and A_1 = 0.173 for the first overtone mode. Hence, larger Q for overtones with respect to the fundamental mode can be obtained by optimizing the QTF dimensions. However, the reduction of the thickness T is limited, since otherwise air-damping losses becomes dominant [28]. Thermo-elastic dissipation can be expressed using a modelling approach proposed by Zener [25]. In a first approximation, Q_{tel} scales with prong size as T^3/L^2.

3.2.2 Electrical characterization and implementation in a QEPAS sensor

Among the six custom QTFs described in Section 3.1.2, three resonators having the same electrode pattern configuration and a low fundamental resonance frequency were selected, QTF #2, QTF #4 and QTF #5, namely, to study and compare their performance when operate at the first and the third flexural mode. In this section, the resonance properties will be investigated in terms of resonance frequency and Q-factor, as well as their performance in a QEPAS-based sensor targeting a water vapour line falling at 7299.43 cm^{-1}, with a line-strength of $1.01 \cdot 10^{-20}$ cm/mol. The QTFs were

electrically characterized by employing an experimental setup similar to the one shown in Fig. 3.6.

In Table 3.6 are reported the calculated resonance frequencies for both the fundamental (n=0) and the first overtone (n=1) mode by using Eq. (3.1), and the correlated node and antinode positions, together with the respective QTFs prong sizes.

Table 3.6 Prong sizes, resonance frequencies, node and antinode points measured starting from the top of the prong, for the three investigated QTFs.

	QTF#2		QTF#4		QTF#5	
L (mm)	10		11		17	
T (mm)	0.9		0.5		1	
w (mm)	0.25		0.25		0.25	
	n =0	**n = 1**	**n =0**	**n = 1**	**n =0**	**n = 1**
f_n (Hz)	7,577.81	47,456.54	3,479.25	21,789.04	2,913.42	18,245.49
node points (mm)	10	2.2 10	11	2.4 11	17	3.7 17
antinode points (mm)	0	0 5.3	0	0 5.8	0	0 9

The QTFs resonance curves in terms of the piezoelectric current are reported in Fig. 3.28, for both the fundamental and the first overtone flexural modes.

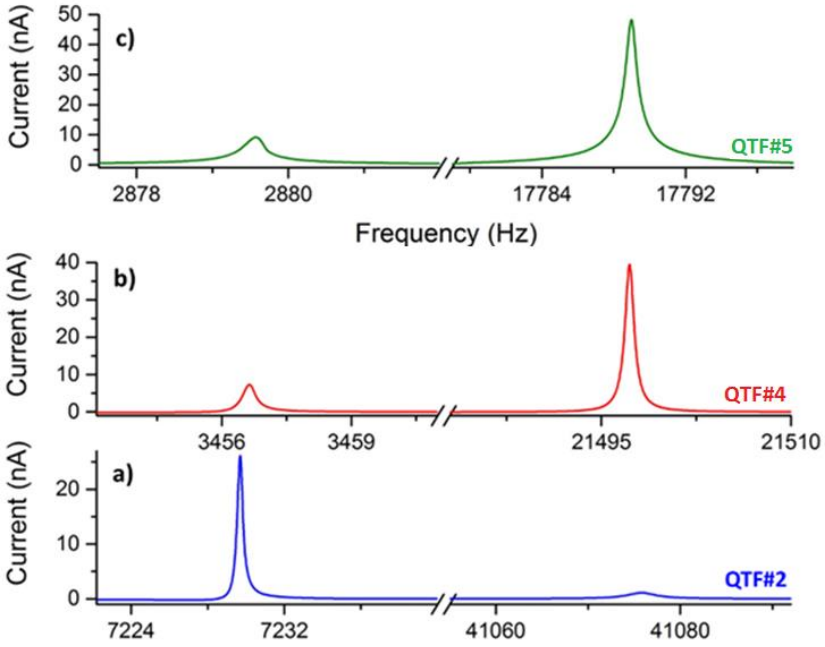

Figure 3.28 QTFs resonance curves measured at a fixed excitation level V = 3.46 mV and at a pressure of 75 Torr in standard air for QTF#2 (a), QTF#4 (b) and QTF#5 (c), for the fundamental and first overtone mode.

For each QTF, the two resonance profiles were separately fitted by using pseudo-Lorentzian functions [7], in order to determine the peak frequencies and the full width at half-maximum. In Fig. 3.29 the calculated quality factors for the fundamental and the overtone mode are reported.

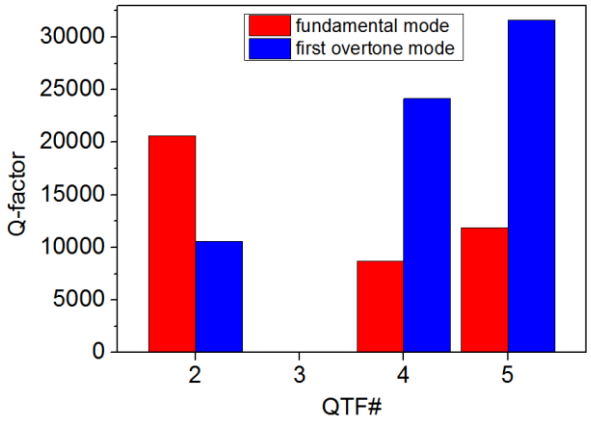

Figure 3.29 Quality factors of the fundamental (red bars) and the first overtone mode (blue bars) measured for QTF#1, QTF#2 and QTF#3 at a pressure of 75 Torr in standard air.

The obtained results show that QTF#4 and QTF#5 exhibit higher quality factors for their first overtone mode, while the QTF#2 presents an opposite behaviour. For the fundamental modes, the overall quality factor dependence on geometrical parameters was phenomenologically found to be Q ~ Tw/L, as reported in Section 3.2.1. For the overtone modes, support losses dominate the energy dissipation processes and indeed the QTF#2, having the lowest $(L/T)^3$ ratio, possesses the smallest overtone mode quality factor. Even though QTF#4 has the highest $(L/T)^3$ ratio, its overtone quality factor results lower than that measured for QTF#5. This can be attributed to two different causes: i) the highest damping ratio β_1 affecting the vibration dynamic of QTF#4, confirming that for thin prongs air damping losses are no longer negligible; ii) the poorest ratio between the gold contacts area and the total surface of the prongs (75 % for QTF#4 vs 90% for QTF#5), results in a lower collection of piezo-generated charges.

3.2.3 Electrode patter enhancing the third flexural mode

In all QEPAS systems demonstrated so far, the electrodes layout of the employed QTFs had a quadrupole pattern, matching the charge distribution generated by the in-plane fundamental mode vibration. Such electrode configuration partially impedes the

excitation of the first overtone flexural mode since it should exhibit a different piezoelectric charge distribution.

In this section, an innovative electrode pattern optimizing the first overtone flexural mode charge collection is proposed, by analyzing the stress field distribution along the QTF prongs. The proposed electrode pattern has an octupole configuration, according to the change of the polarity along the prongs at the zero-stress point occurring for the first overtone flexural mode. To provide a comparison between quadrupole and octupole electrode configurations in terms of QEPAS sensing performance, the performance of two QTFs having the same geometry and size but a different contact pattern configurations are analyzed. Among the QTFs analyzed in Section 3.2.2, the one having the highest Q-factor, QTF #5 (referred hereafter as QTF #5-Q), was selected and designed a new QTF #5 with an octupole configuration gold pattern (referred hereafter as QTF #5-O). Both QTFs were implemented into a sensor system for water vapor trace detection [29].

In Section 1.2, the tensile stress along the prong axis has been derived by using the formulation of the displacement derived by the Euler-Bernoulli equation. The fundamental mode shows the highest stress antinode at the top of the prong, while the first overtone mode shows two stress antinode points, one negative at the top of the prong and one positive at about half of the prong. For the fundamental vibrational mode, the sign of the strain distribution does not change over the entire length of the QTF prong. Whereas, for the first overtone mode the strain direction changes along the length of the prong and consequently also the sign of the piezoelectrically induced charges, reversing at the zero-stress point. Therefore, the electrode patterns deposited on QTF surfaces must be divided into separated zones corresponding to opposite generated electric fields (and charges) areas in order to efficiently retrieve the piezoelectric signal provided by a specific flexural resonance mode.

The separation between electrodes of different polarity is located where the sign of the strain field reverses. For the fundamental flexural mode, the sign of the stress (and thereby of the generated charges) alternates between adjacent lateral prong surfaces but remains the same along the prong length (see Fig. 3.30(a)). Hence, a quadrupole electrode pattern should be employed. For the overtone mode, the sign of the stress is opposite over adjacent surfaces, as for the fundamental, but it changes also along each prong surface when crossing the zero-stress point (see Fig. 3.30(b)). This requires a

dual-quadrupole electrode layout configuration, i.e. an octupole electrode pattern, for optimal charge collection. Based on this analysis, a QTF having the same geometry of QTF #5 implementing an octupole (QTF #5-O) electrode pattern was realized.

For the octupole configuration, a zero-stress point along the prong occurs at 3.8 mm from the support-prong junction. The side electrode of a quadrupole portion is connected with the central electrode of the other portion by means of small electrode stripes. For both quadrupole and octupole configuration, the side electrode length is reduced on the top and wrap around at the end prongs in order to connect the two central (side) electrodes deposited on the opposite QTF #5-Q (QTF #5-O) surface.

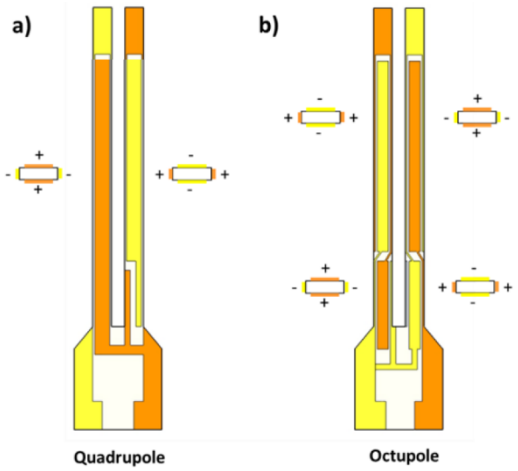

Figure 3.30 (a) Schematic of the QTF #5-Q with a quadrupole electrode pattern. (b) Schematic of the QTF #5-O having an octupole electrode pattern. The pattern configuration is inverted in the QTFs back surfaces. The small rectangles represent sections of the prong with the corresponding charge distributions.

The influence of the electrode layout on the main QTFs characteristics, namely the resonance frequency, the quality factor and the electrical resistance were investigated by using the experimental setup depicted in Fig. 3.31.

The QTF #5-Q and QTF #5-O spectral responses at atmospheric pressure for the fundamental and the overtone modes are shown in Fig. 3.31(a) and 3.31(b), respectively.

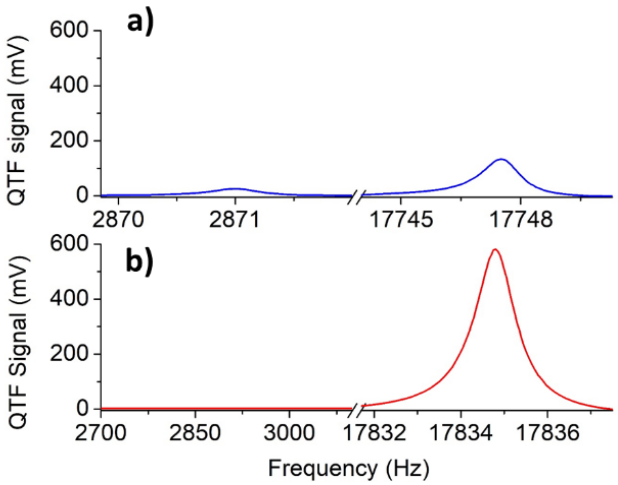

Figure 3.31 Resonance curves measured at a fixed excitation level V = 300 mV and at atmospheric pressure for the QTF #5-Q (a) and QTF #5-O (b).

Each resonance curve was thereby fitted by using a pseudo-Lorentzian function to determine the resonance frequency and its FWHM values, used to calculate the corresponding quality factor Q = f/FWHM. The obtained parameters are listed in Table 3.7.

Table 3.7 Resonance frequency, quality factor and electrical resistance values measured for the QTF-Q when vibrating at the fundamental or the first overtone mode and for the QTF-O when vibrating at the first overtone mode.

	QTF #5-Q	QTF #5-Q	QTF #5-O
	Fund. mode	Overt. mode	Overt. Mode
Frequency (Hz)	2870.99	17747.47	17834.79
Quality factor	5850	14500	15290
Resistance (kΩ)	810.8	157.6	36.1

As previously mentioned, although the quadrupole electrode structure is designed to enhance the excitation of the fundamental mode of the QTF, it is also able to excite the first overtone mode, whereas in QTF #5-O the fundamental mode is completely suppressed. The Q-factor for both QTFs vibrating at the overtone mode remains almost the same. This is to be expected because the quality factor is mainly affected by loss

mechanisms occurring in the vibrating prongs, as explained in Section 3.2.2 and not by the charge collection efficiency.

The implementation of an octupole contact pattern strongly reduces (by a factor of ~ 4.4) the electrical resistance for the first overtone mode, demonstrating that this configuration collects the charges induced in the prongs more efficiently. Indeed, a large electrical conductance provides a high QEPAS signal, which implies that QTF #5-O is expected to offer improved performances in terms of trace gas sensing when operated at the first overtone mode [17,27]. In order to verify this assumption, both QTFs were implemented in the QEPAS setup similar to the one shown in Fig. 3.21. In this case, the QCL targeted a water vapor absorption line falling at 1931.76 cm^{-1}, having a line-strength of $3.2 \cdot 10^{-22}$ cm/molecule, according to HITRAN database [15]. The vertical position of the laser beam focus along the QTF axis was optimized in terms of QEPAS signal. The laser was focused at 2 mm and 9.5 mm from the top of QTFs when vibrating at the fundamental or the first overtone mode, respectively. The QEPAS sensor operates with a wavelength modulation and dual-frequency detection approach. The absorption line is acquired by applying a slow ramp (frequency of 5 mHz) to the current driver. The QEPAS spectral scans of the selected water absorption line obtained for each vibrational mode of the investigated QTFs are shown in Fig. 3.32.

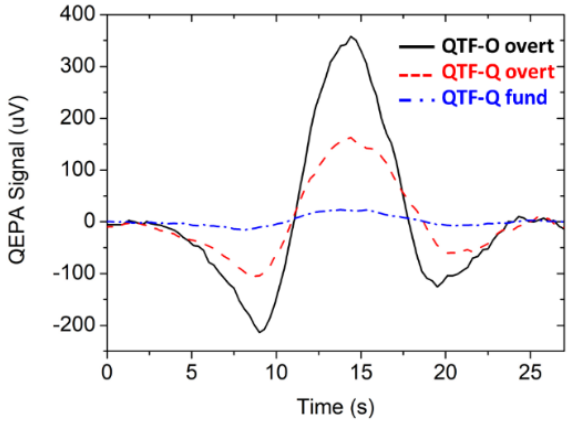

Figure 3.32 QEPAS spectral scans of the water absorption line measured with the QTF #5-O operating at the first overtone mode (solid black curve) and the QTF #5-Q operating at the fundamental (dot-dashed blue curve) or the overtone (dashed red curve) mode.

The QEPAS spectra show that the peak value measured for QTF #5-O operating at the overtone mode is ~2.3 times higher than that obtained with QTF #5-Q operating at the overtone mode and ~15.3 times higher when QTF #5-Q operated at the fundamental

mode. This confirms that to fully exploit the photoacoustic performance of QTFs first overtone mode an octupole contact pattern configuration must be employed.

3.2.4 Single-tube On-beam QEPAS at the overtone mode

In the beginning sections of this chapter the dependence of the QTF parameters and performance on their relevant dimensions was determined. Such a study allows the design of custom QTFs optimized for optoacoustic gas sensing with sizes and geometries selected *ad-hoc* to fulfil the requirements of the specific application. For example, it was demonstrated that the parameters T, L and w can be chosen in order to decrease the first overtone resonance frequency to values $<< 1/2\pi\tau$ and enhance the related quality factor. In Section 1.2.1, the coupling of a QTF with a couple of micro-resonator tubes, resulting in a dual-tube spectrophone, has been presented as a technique to enhance the QEPAS signal while keeping noise at the same level. In this section the geometrical characteristics of QTF #6 are exploited to develop a novel spectrophone composed by a QTF operated at the third flexural mode and coupled with a single-tube resonator accommodated between the prongs. Such a single-tube spectrophone will be implemented in an on-beam QEPAS (SO-QEPAS) setup and its performance will be compared with the one of a dual-tube spectrophone based on the same QTF.

Electrical characterization of QTF #6 was performed by employing the setup shown in Fig. 3.6. At atmospheric pressure, QTF #6 exhibited a third flexural mode resonance frequency of 25,413 Hz, with a Q-factor of 28,942, ~ 2.8 times higher than the one measured for the first flexural mode.

The architecture of the QEPAS sensor used to study the photoacoustic performances of both resonance modes is similar to that reported in Fig. 3.21. As excitation source, a single-mode quantum cascade laser (QCL) was employed, emitting at 7.7 μm, targeting a water vapor line at 1296.49 cm^{-1} with a line strength of $1.70 \cdot 10^{-22}$ cm/mol, as reported in the HITRAN database [15]. A fixed concentration of 1.7% of water vapor at atmospheric pressure was measured.

The QEPAS spectral scans obtained for the fundamental and overtone modes are shown in Figure 3.33.

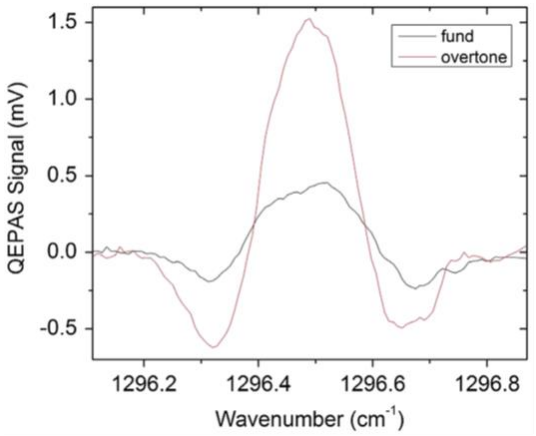

Figure 3.33 QEPAS spectral scans of the 1.7% water absorption line acquired for the fundamental mode (black solid line) and for the first overtone one (red solid line). Both scans were acquired with a 100 ms lock-in integration time.

The two QEPAS spectra show the same noise level (~13 μV), while the peak value measured for the first overtone mode is ~ 3.1 times higher than that obtained using the fundamental one. This result confirms that the mode showing the higher Q-factor gives also the higher QEPAS signal.

The QTF was coupled with a pair of micro-resonator tubes acting as amplifiers for the sound wave. As described in Section 1.2.1, the geometrical parameters influencing the sensor performance are the internal diameter and the length of the two tubes together with the spacing between the tube and the surface of the QTF. The best QTF-tube distance, tube length and tube internal diameter were found to measure 140 μm, 5.3 mm and 1.52 mm, respectively. Compared to the bare QTF, a signal-to-noise ratio enhancement (SNR_E) of 15 times was obtained [17].

The SO-QEPAS configuration was obtained by locating a single-tube acting as one-dimensional acoustic resonator between the prongs of the QTF. For tubes having an outer diameter (OD) larger than the prong spacing, the OD was reduced by polishing the waist of the tube thickness. A pair of slits was opened on each side of the tube waist, symmetrically in the middle of the tube as shown in Fig. 3.34.

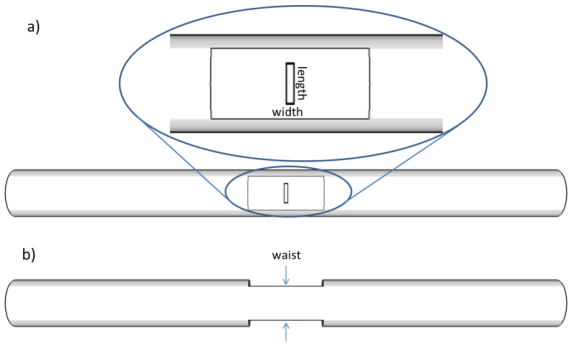

Figure 3.34 Front (a) and top (b) view of the single micro-resonator tube.

The micro-resonator tube was positioned between the prongs of the QTF at 12 mm from the top of the QTF in order to allow the sound wave exiting from the two slits to impact on the internal surface of the two prongs. A complete investigation of the impact of the tubes geometry, namely the internal diameter (ID), the length and the size of the slit, on the SO-QEPAS sensor performance was carried out for the QTF overtone mode.

In order to determine the optimum internal diameter maximizing the SO-QEPAS signal a set of 4 tubes having different internal diameters (0.67 mm, 0.80 mm, 0.88 mm and 0.96 mm) with the same length l = 10.8 mm was prepared. The slit length was 0.5 mm for ID = 0.67 mm and 0.80 mm, and 0.9 mm for ID = 0.88 mm and 0.96 mm. The slit width was 0.1 mm for all micro-resonator tubes. The QEPAS peak signal as a function of the tube ID is shown in Fig. 3.35.

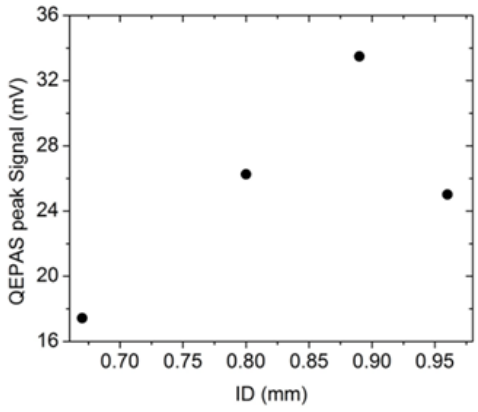

Figure 3.35 QEPAS peak signals plotted as a function of the internal diameter of the micro-resonator tube. The length of the tube was fixed to 10.8 mm.

The highest QEPAS signal (33.5 mV) was obtained with tube having ID = 0.88 mm. The QEPAS noise level is influenced by the size of the internal diameter as the radiation touching the internal surface of resonator tubes can drastically increase the QEPAS

background noise level. In Fig. 3.36(a) the 1σ noise values recorded at different IDs were plotted and in Fig. 3.36(b) the related optical coupling efficiencies, defined as the percentage of the laser power coupled with the SO-QEPAS spectrophone are depicted.

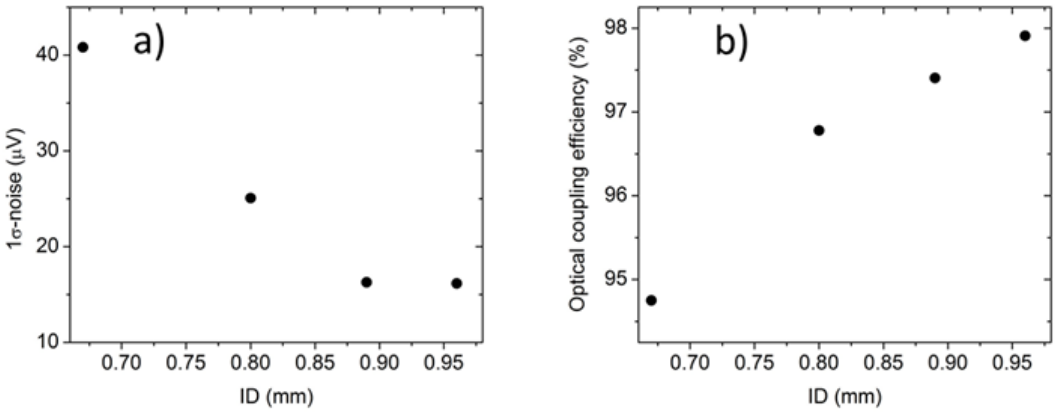

Figure 3.36 1σ background noise values (a) of the QEPAS signal and the optical coupling efficiency (b) plotted as a function of the internal diameter of the micro-resonator tube. The length of the tube was fixed to 10.8 mm in all cases.

It was observed that for an ID = 0.88 mm and l = 10.8mm the background noise level is 16.3μV, 20% higher than that measured for the bare QTF (13.0 μV). This was due to a small amount of laser power touching the tube. This was also confirmed by a reduction of the laser power coupling efficiency to 97.4 % (99.5% for the bare QTF). For the smallest ID, the noise level increases up to 40.8μV and the coupling efficiency decreases to 94.8%.

For an ID = 0.88 mm, the QEPAS performance at different tube lengths (slit sizes were not changed), ranging from 13.3 mm (~λ) to 7 mm (~λ/2) was investigated. The results are shown in Fig. 3.37.

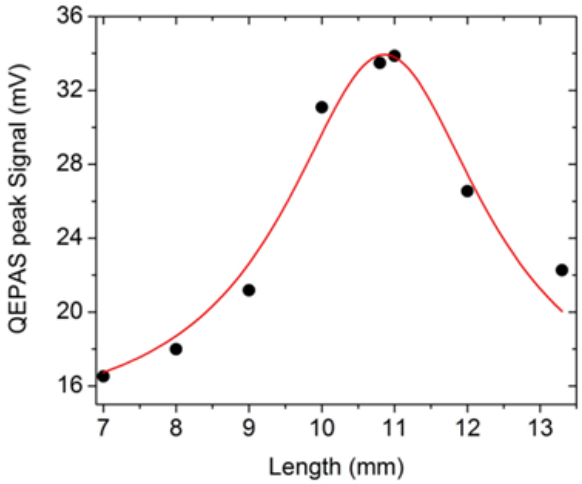

Figure 3.37 QEPAS peak signals (dots) plotted as a function of the micro-resonator tube length. The tube internal diameter was 0.88 mm in all cases. The solid line is the Lorentzian fit of the experimental data.

The maximum QEPAS signal of 33.9 mV was obtained for an optimal tube length of 11.0 mm. The observation of an optimal tube length > λ/2 is a clear evidence that the 1st harmonic acoustic standing waves in the tube were partially distorted by the two slits present in the acoustic resonator, as observed in previous SO-QEPAS experiments [30,31]. In Fig. 3.38 the 1σ background noise values and the related coupling efficiency are depicted as a function of the micro-resonator tube length.

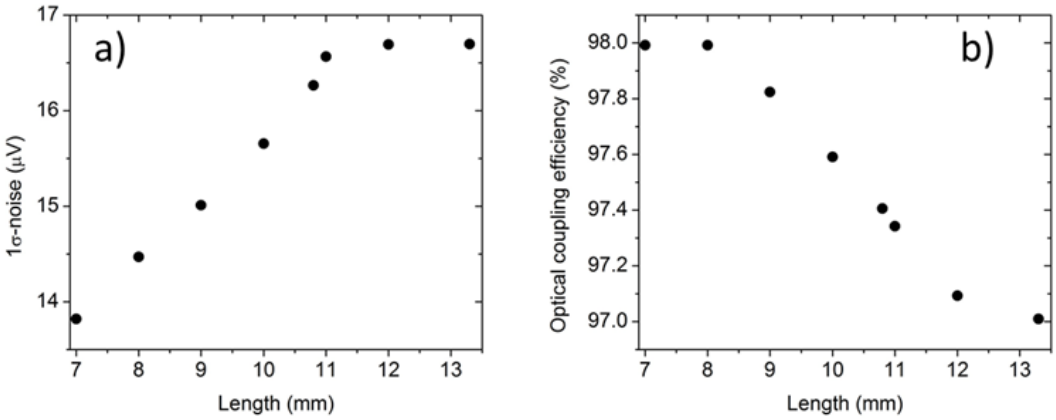

Figure 3.38 1σ background noise values (a) of the QEPAS signal and optical coupling efficiency (b) plotted as a function of the micro-resonator tube length. The tube internal diameter was 0.88 mm in all cases.

The optical coupling reaches 98% and the noise level is 13.8 μV, which is almost identical to that measured with the bare QTF when the length of the micro-resonator tube is reduced to 7mm. For a tube length l = 11 mm, the noise level is 16.6 μV.

The last geometrical parameter to be investigated was the slit size. For the ID = 0.88 mm and an l = 10.8 mm the slit width was enlarged without changing its length. The results are shown in Fig. 3.39.

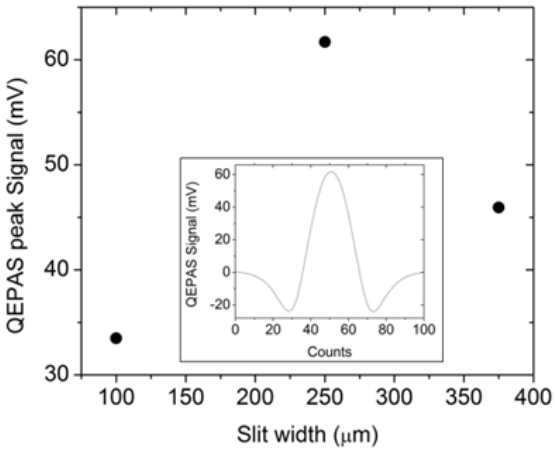

Figure 3.39 QEPAS peak signal recorded for three different slit widths. In all three cases, the tubes were 10.8 mm long, with the ID of 0.88 mm and the slit length of 0.9 mm. Inset: SO-QEPAS spectral scan of the selected water line with the QTF operating with the overtone mode with the tube ID of 0.88 mm, length of 11.0 mm and a slit width of 250μm. The integration time of the lock-in amplifier was set to 100 ms.

The QEPAS signal increases up to 61.7 mV when the slit width is 250 μm, almost twice with respect to a slit width of 100 μm. The quality factor was ~ 10% lower than that of the bare QTF. The QEPAS signal decreases to 45.9 mV when the slit width is enlarged to 370 μm.

The optimum geometrical parameters of the tube maximizing the QEPAS signal, i.e internal diameter of 0.88 mm, length of 11.0 mm and a slit width of 250μm, allowed an SNR_E of ~ 34 times respect to the bare QTF.

3.3 *QTF#4*- and *QTF-S08-T*-based spectrophones for Ethylene QEPAS detection

Ethylene (C_2H_4) is a colourless, flammable alkene with a sweet odour [32]. Among the hydrocarbons, ethylene is one of the most basic building blocks in chemistry: processing chemical plants turn it into polyethylene, polyester, PVC, polystyrene and

ethyline glycole. Ethylene crackers are spreading over the U.S. territory [33] to increase the feedstock capacity, making C_2H_4 detection fundamental for its even rising demand.

As a plant hormone, ethylene has a key role in fruit ripening mechanism definition [34]. Fruits like Cantaloupe melon, avocado, banana and apple, characterized by a cellular respiration-related ripening stage accompanied by a burst of ethylene, are named climacteric fruits and are distinguished from non-climacteric fruits, like strawberry, grape and citrus, whose cellular respiration does not involve ethylene production [35,36]. In climacteric fruits an increase in the level of endogenous ethylene is a ripening trigger. Exogenous ethylene in the part-per-million range has identical ripening effects with those which occur naturally [37]. For this reason, C_2H_4 detection with part-per-million sensitivity is crucial in food industry to monitor both storage and transportation environment and avoid early fruit epinasty.

Finally, although animals lack ethylene biosynthetic enzymes similar to the one in plants, there is evidence that mammals can form ethylene upon oxidative damage. Moreover, ethylene has been demonstrated to be produced during systemic inflammation in humans and, as part of endogenous lipid peroxidation caused by the respiratory burst, to be released in exhaled breath [38]. Ethylene is thus a promising and novel biomarker for early onset of infection in the clinic.

In this section, the QEPAS technique is exploited for the detection and the quantification of ethylene. With the aim of achieving the highest sensitivity as possible, the performance of two dual-tubes spectrophones, employing QTF #4 and QTF-S08-T, respectively, were compared. The two spectrophones were implemented in the same QEPAS-based sensor, whose architecture is depicted in Fig. 3.40.

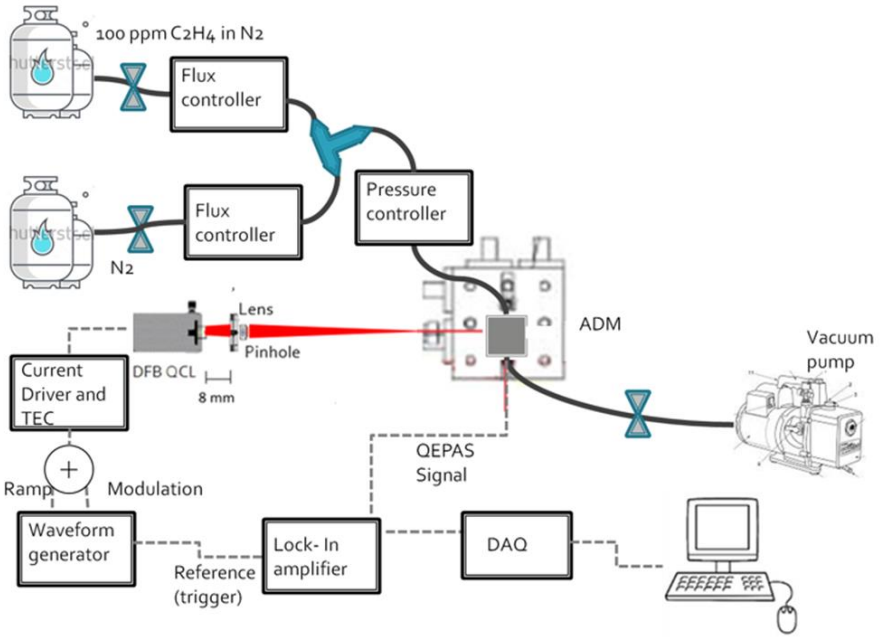

Figure 3.40 Schematic of the QEPAS experimental setup employed for the detection of ethylene. DFB QCL – Distributed Feedback Quantum Cascade Laser. ADM – Acoustic Detection Module. DAQ – Data Acquisition card

A distributed feedback quantum cascade laser emitting at ~ 10.35 μm was used as the laser source exciting the ethylene molecules within a compact Acoustic Detection Module (ADM), consisting in a 5 cm^3 volume gas cell containing the spectrophone and a transimpedance amplifier. A pinhole, set between the lens and the ADM, removes beam tails that could hit the QTF prongs generating a non-zero background, thus worsening the sensor detection sensitivity. The far field spatial intensity distribution of the laser beam in the focal plane of the focusing lens has been acquired using a mid-infrared pyrocamera (pixel size 100μm x 100μm) and is shown in Fig. 3.41.

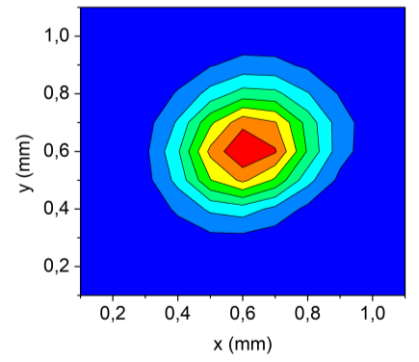

Figure 3.41 Two-dimensional beam profile filtered by the pinhole, acquired by means of a mid-infrared pyrocamera in the focal plane of the focusing lens.

The beam exhibits a quasi-circular-symmetric Gaussian-like profile with a diameter 0.29 mm. The use of the pinhole causes an optical power reduction of 7.2%, resulting in a focalized optical power P=66 mW. The modulated laser radiation focused between the QTF prongs in the ADM generates sound waves that excite the QTF flexural modes. The resulting piezoelectric current signal is transduced into a voltage signal by a transimpedance amplifier (with a 10 ΩM feedback resistor). A wavelength modulation (WM) and 2f detection technique was implemented: a sinusoidal dither was applied to the laser current at half of the QTF resonance frequency and the QTF response was detected at the resonance frequency using a lock-in amplifier. QEPAS spectral scans were performed by scanning the laser wavelength adding a slow ramp to the QCL current driver. The QTF signal demodulated by the lock in amplifier was converted to a digital signal using a National Instrument DAQ card connected to a personal computer. The target gas flowed through the gas line with a rate of 20 sccm and a pressure optimizing the QEPAS signal, as set by two controllers. The lock-in integration time was set at 100 ms and a signal acquisition time of 300 ms was selected.

Two different spectrophones were implemented in the ADM. The first one, S_1, employed a first generation QTF, operated at the third flexural mode. In order to keep compact the dimension of the spectrophone, among the QTFs described in Section 3.1.2 having a first overtone resonance frequency suitable for QEPAS purposes with a high Q-factor, QTF #4 was selected. The QTF was coupled with two micro-resonator tubes having inner diameter of 0.84 mm and a length of 4 mm, set at a distance of 50 μm from the QTF. The second spectrophone, S_2, employs a second generation QTF operated at the fundamental mode and is composed by QTF-S08-T coupled with two micro-resonator tubes 12.4 mm long, with 1.59 mm inner diameter, set 200 μm from the QTF (see Section 3.1.4). The electrical properties of the two spectrophones have been studied by using an experimental setup having the same scheme of the one shown in Fig. 3.6. The spectral responses of the S_1 first overtone mode and S_2 fundamental mode are shown in Fig. 3.42.

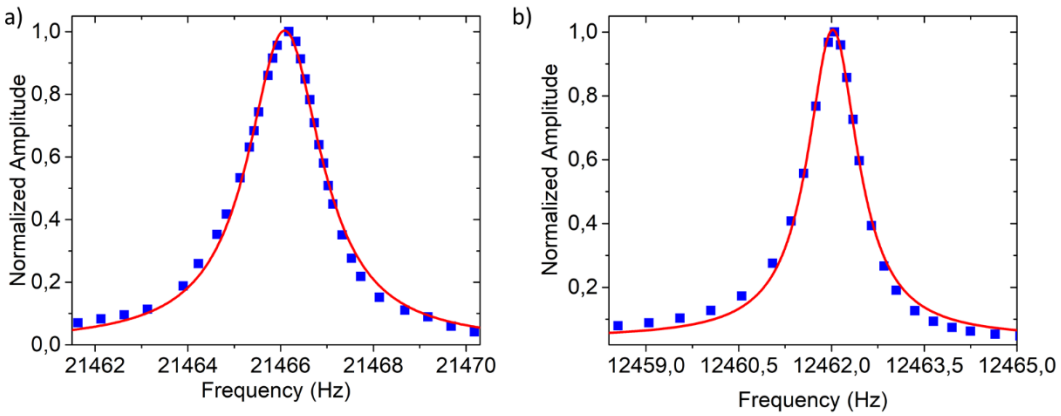

Figure 3.42 Normalized resonance curves of the spectrophone S_1 employing QTF #4 (a) and S_2 employing QTF-S08-T (b) at atmospheric pressure. The red solid lines indicate the best Lorentzian fit.

For each spectrophone, the resonance frequency and Q-factor were determined by fitting the resonance spectra with a Lorentian curve. The obtained results are summarized in Table 3.8.

Table 3.8 S_1 first overtone mode and S_2 fundamental mode resonance frequency and Q-factor .

Spectrophone	Resonance frequency	Q-factor
S_1	21466.12 Hz	20880
S_2	12462.02 Hz	12540

A wide-range spectral scan of a certified concentration of 100 ppm of C_2H_4:N_2 was performed, within the tunability range of the employed QCL, to identify the strongest absorption line to be targeted. In Fig. 3.43 a comparison between the absorption cross section simulated by using HITRAN database and the scan obtained by employing the spectrophone S_1 is shown.

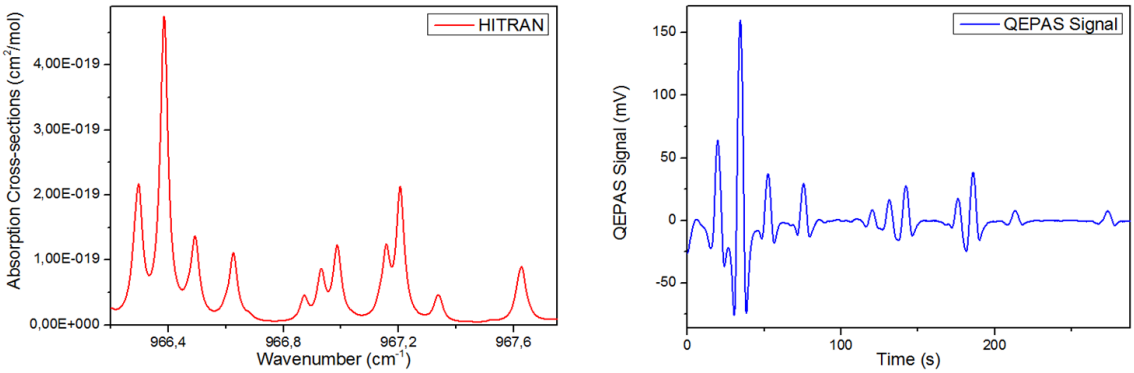

Figure 3.43 100 ppm C_2H_4:N_2 absorption spectrum simulated by using HITRAN database (a) and QEPAS spectral scan over the QCL tunability range (b).

The comparison between the two graphs in Fig. 3.43 shows a perfect match between the simulated data and the acquired QEPAS spectral scan and identifies the line falling at 966.38 cm^{-1} as the strongest absorption feature, with a line-strength of $2.21 \cdot 10^{-20}$ cm/mol.

Figure 3.44 shows the QEPAS spectral scans of the 966.38 cm^{-1} absorption peak of 100 ppm of C_2H_4:N_2 acquired by employing S_1 and S_2, obtained by applying a ramp with amplitude 300 mV and frequency 7 mHz to the QCL current driver. Operating pressure and dither amplitude maximizing the QEPAS signal were identified. The optimum amplitude modulation was 23 mV while optimum operating pressure was 120 Torr for S_1 and 105 Torr for S_2, respectively.

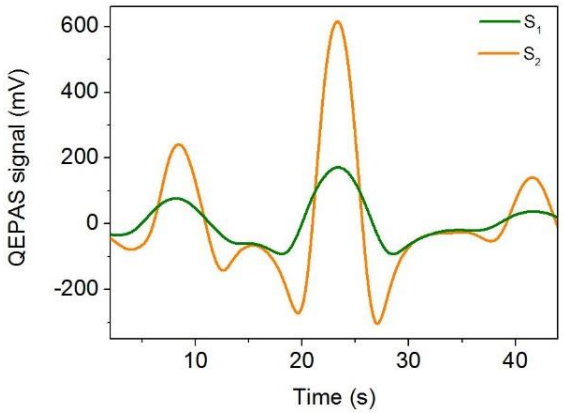

Figure 3.44 QEPAS signal of 100 ppm C_2H_4:N_2 966.38 cm^{-1} absorption peak implementing S_1 (orange solid line) and S_2 (olive solid line)

Ethylene peak signal, measured by implementing the spectrophone S_1 in the ADM, was 171.79 mV, with a 1σ noise of 0.172 mV, leading to a signal-to-noise ratio (SNR) of ~ 1000. When implementing the spectrophone S_2, a signal of 615.82 mV, with a 1σ noise

of 0.180 mV, was obtained. The slightly higher noise is due to longer micro-resonator tubes employed in spectrophone S_2 compared with S_1, causing beam tails lightly hitting the tubes internal surface. However, the corresponding SNR is 3420, ~ 3.4 times higher than the one obtained by employing the spectrophone S_1. This result confirms that by combining the model described in Section 3.1.1, the simulations performed by COMSOL Multiphysics (see Section 3.1.4), and the studies on the signal amplification by micro-resonator tubes acoustic coupling, a spectrophone optimized for QEPAS sensing can be designed. By employing S_2, an SNR=1 minimum detection limit (MDL) of 29 part-per-billion (ppb) is obtained.

A QEPAS sensor calibration implementing spectrophone S_2 was performed. Figure 3.45(a) shows the spectral scans of 40 ppm, 30 ppm, 20 ppm, 10 ppm and 5 ppm C_2H_4:N_2 obtained by diluting ethylene with nitrogen, as well as the signal acquired in pure N_2. The peak values have been plotted as a function of the concentration in Fig. 3.45(b) and a calibration curve has been obtained.

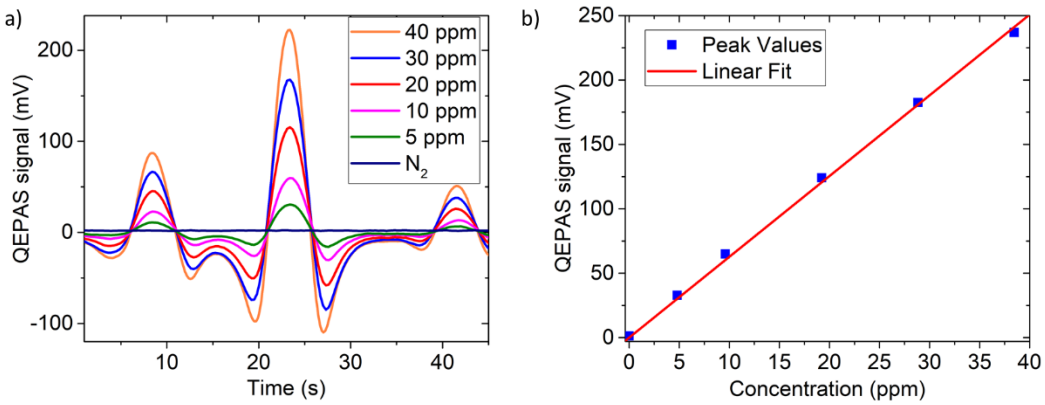

Figure 3.45 QEPAS spectral scan (a) of 40 ppm, 30 ppm, 20 ppm, 10 ppm and 5 ppm C_2H_4:N_2 and pure N_2 and peak values (b) measured for each ethylene concentration (blue squares) with the corresponding best linear fit (red line).

The linear fit of the measured peak values yields a slope of 6.27 mV/ppm, with a calculated R-squared value equal to 0.999.

The 1σ noise can be lowered by further averaging the signal over a longer time (see Appendix). An Allan-Werle deviation analysis was performed with the aim of predicting the 1σ noise and thus the achievable minimum detection limit as a function of the lock-in integration time. The obtained Allan-Werle deviation plot is reported in Fig. 3.46.

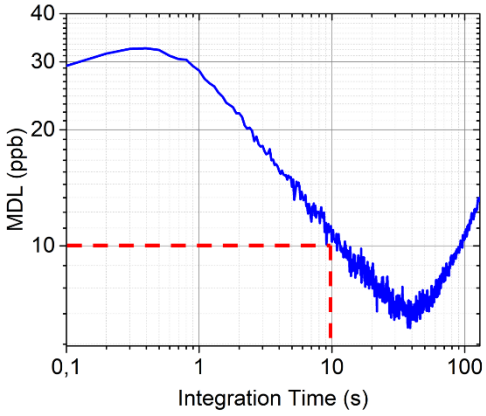

Figure 3.46 Allan-Werle deviation plot of the QEPAS signal in ppb units as a function of the lock-in integration time. For a 10 s integration time, a minimum detection limit of ~10 ppb was achieved (red dashed line).

For a lock-in integration time of 10 s a minimum detection limit as low as 10 ppb can be reached, corresponding to a Normalized Noise Equivalent Absorption (NNEA) of $9.6 \cdot 10^{-10}$ W· $cm^{-1} \cdot Hz^{-1/2}$.

The sensitivity achieved with the S_2–based QEPAS sensor fulfils the requirements for ethylene detection in chemical industry, quality control in food industry and breath sensing in medicine.

References

[1] K. Karrai and R.D. Grobe, Piezoelectric tip-sample distance control for near field optical microscopes, Appl. Phys. Let. 66.14 (1995) 1842-1844.

[2] D. Sarid,. Scanning force microscopy: with applications to electric, magnetic, and atomic forces, Vol. 5. Oxford University Press on Demand, 1994.

[3] P. Patimisco, S. Borri, A. Sampaolo, H. E. Beere, D. A. Ritchie, M. S. Vitiello, G. Scamarcio, and V. Spagnolo, A quartz enhanced photo-acoustic gas sensor based on a custom tuning fork and a terahertz quantum cascade laser, Analyst 139 (2014) 2079.

[4] K. Karrai and R. D. Grober, Piezoelectric tipsample distance control for near field optical microscopes, Appl. Phys. Lett. 66 (1995) 1842.

[5] J. Liu, A. Callegari, M. Stark, and M. Chergui, A simple and accurate method for calibrating the oscillation amplitude of tuning-fork based AFM sensors, Ultramicroscopy 109 (2008) 81.

[6] F. J. Giessibl, F. Pielmeier, T. Eguchi, T. An, and Y. Hasegawa, Comparison of force sensors for atomic force microscopy based on quartz tuning forks and length-extensional resonators, Phys. Rev. B 84 (2011) 125409.

[7] D. I. Bradley, M. J. Fear, S. N. Fisher, A. M. Guénault, R. P. Haley, C. R. Lawson, G. R. Pickett, R. Schanen, V. Tsepelin, and L. A. Wheatland, Stability of flow and the transition to turbulence around a quartz tuning fork in superfluid 4He at very low temperatures, Phys. Rev. B 89 (2014) 214503.

[8] P. Patimisco, A. Sampaolo, L. Dong, M. Giglio, G. Scamarcio, F. K. Tittel, and V. Spagnolo, Analysis of the electro-elastic properties of custom quartz tuning forks for optoacoustic gas sensing, Sens. Actuators B Chem 227 (2016) 539-546.

[9] M. Hirata, K. Kokubun, M. Ono, and K. Nakayama, Size effect of a quartz oscillator on its characteristics as a friction vacuum gauge, J. Vac. Sci. Technol. A 3 (1985) 1742.

[10] Z. Hao, A. Erbil, and F. Ayazi, An analytical model for support loss in micromachined beam resonators with in-plane flexural vibrations, Sensors and Actuators A-Physical 109 (2003) 156.

[11] S. L. Ahlstrom, D. I. Bradley, M. Clovecko, S. N. Fisher, A. M. Guénault, E. A. Guise, R. P. Haley, O. Kolosov, P. V. E. McClintock, G. R. Pickett, M. Poole, V. Tsepelin, and A. J. Woods, Frequency-dependent drag from quantum turbulence produced by quartz tuning forks in superfluid 4He, Phys. Rev. B 89 (2014) 014515.

[12] P. Patimisco, G. Scamarcio, F.K. Tittel, V. Spagnolo, Quartz-Enhanced Photoacoustic Spectroscopy: A Review, Sensors 14 (2014) 6165-6205.

[13] P. Patimisco, A. Sampaolo, V. Mackowiak, H. Rossmadl, A. Cable, F.K. Tittel, and V. Spagnolo, Loss Mechanisms Determining the Quality Factors in Quartz Tuning Forks Vibrating at the Fundamental and First Overtone Mode, IEEE T. Ultrason. Ferr. 10.1109 (2018) 2853404.

[14] Y. Qin and R. Reifenberger, Calibration a tuning fork for use as a scanning probe microscope force sensor, Rev. Sci. Instrum. 78 (2007) 063704.

[15] See http://www.hitran.org/

[16] L. Dong, A.A. Kosterev, D. Thomazy, and F.K. Tittel, QEPAS spectrophones: Design, optimization, and performance, Appl. Phys. B 100 (2010) 627–635.

[17] P. Patimisco, A. Sampaolo, H. Zheng, L. Dong, F.K. Tittel, and V. Spagnolo, Quartz enhanced photoacoustic spectrophones exploiting custom tuning forks: a review, Adv. Phys. X 2 (2016) 169-187.

[18] P. Patimisco, A. Sampaolo, M. Giglio, S. Dello Russo, V. . Mackowiak, H. Rossmadl, A. Cable, F.K. Tittel, and V. Spagnolo, Tuning forks with optimized geometries for quartz-enhanced photoacoustic spectroscopy, Opt. Express (2018), in press

[19] W. H. Flygare, Molecular relaxation, Acc. Chem. Res. 1 (1968) 121-127.

[20] H. Hosaka , K. Itao, S. Kuroda, Damping characteristics of beam-shaped micro-oscillators, Sensor. Actuat. A-Phys. 49 (1995) 87-95.

[21] K. Kokubun, H. Murakami, Y. Toda, M. Ono, A bending and stretching mode crystal oscillator as a friction vacuum gauge, Vacuum 34 (1984) 731-735.

[22] F.R. Blom, S. Bouwstra, M. Elwenspoek, J.H.J. Fluitman, Dependence of the quality factor of micromachined silicon beam resonators on pressure and geometry, J. Vac. Sci. Technol. B 10 (1992) 19-26.

[23] Y. Jimbo, K. Itao, Energy loss of a cantilever vibrator, J. Horological Inst. Jpn 47 (1968) 1-15.

[24] D.M. Photiadisa, J.A. Judge, Attachment losses of high Q oscillators, Appl. Phys. Lett. 85 (2005) 482-484.

[25] C. Zener, Internal Friction in Solids II. General Theory of Thermoelastic Internal Friction, Phys. Rev. 53 (1938). 90-99.
[26] R. R. Archer, N. H. Cook, S. H. Crandall, N. C. Dahl, F. A. McClintock, E. Rabinowicz, and G. S. Reichenbach, An introduction to the mechanics of solids, New York: McGraw-Hill, 1959.
[27] F.K. Tittel, A. Sampaolo, P. Patimisco, L. Dong, A. Geras, T. Starecki, and V. Spagnolo, Analysis of overtone flexural modes operation in quartz-enhanced photoacoustic spectroscopy, Opt. Express 24, 6 (2016) A682-A692.
[28] A. Sampaolo, P. Patimisco, L. Dong, A. Geras, S, G. Scamarcio, T. Starecki, F. K. Tittel, and V. Spagnolo, Quartz-Enhanced Photoacoustic Spectroscopy exploiting tuning fork overtone modes, Appl. Phys. Lett. 107 (2015) 231102-231102-4.
[29] P. Patimisco, A. Sampaolo, M. Giglio, V. Mackowiak, H. Rossmadl, B. Gross, A. Cable, F. K. Tittel, and V. Spagnolo, Octupole electrode pattern for tuning forks vibrating at the first overtone mode in quartz-enhanced photoacoustic spectroscopy, Opt. letters 43, 8 (2018) 1854-1857.
[30] Zheng, H., Dong, L., Sampaolo, A., Wu, H., Patimisco, P., Yin, X., Ma, W., Zhang, L., Yin, W., Spagnolo, V., Jia, S., and Tittel, F. K., Single-tube on-beam quartz-enhanced photoacoustic spectroscopy, Opt. Lett. 41 (2016) 978-981.
[31] Zheng, H., Dong, L., Sampaolo, A., Wu, H., Patimisco, P., Ma, W., Zhang, L., Yin, W., Xiao, L., Spagnolo, V., Jia, S., and Tittel, F. K., Overtone resonance enhanced single-tube on-beam quartz enhanced photoacoustic spectrophone, Appl. Phys. Lett. 109 (2016), 111103.
[32] H. Zimmermann, H. and R. Walzl, Ethylene, Ullmann's Encyclopedia of Industrial Chemistry, Wiley-VCH (2009).
[33] A. Tullo, Petrochemicals: Market will remain tight despite new capacity, Chemical and Engineering News 96, 2, 8 (2018) 29.
[34] S. P. Burg, and E. A. Burg, Role of ethylene in fruit ripening, Plant Physiology 37, 2 (1962) 179.
[35] J.C. Pech, M. Bouzayen, A. Latché, Climacteric fruit ripening: Ethylene-dependent and independent regulation of ripening pathways in melon fruit, Plant Science 175, 1-2 (2008) 114-120.
[36] L. Alexander, D. Grierson, Ethylene biosynthesis and action in tomato: A model for climacteric fruit ripening, J. Exp. Bot., 53, 377 (2002) 2039-2055.
[37] E.J. McMurchie, W. B. McGlasson, and I. L. Eaks, Treatment of fruit with propylene gives information about the biogenesis of ethylene, Nature 237, 5352 (1972) 235.
[38] L.M. Paardekooper, G. Bogaart, M.s Kox, I. Dingjan, A.H. Neerincx, M.B. Bendix, M. Ter Beest, F.J. Harren, T. Risby, P. Pickkers, and N. Marczin, Ethylene, an early marker of systemic inflammation in humans, Sci. Rep. 7, 1 (2017) 6889.

Chapter 4
Broadband absorbers detection in mid-infrared spectral range

Many chemical compounds that play a key-role in fields of interest such as environmental monitoring, early diagnosis of cancer and metabolic diseases, hydrocarbon monitoring in petrochemical industry, and homeland security, belong to the class of broadband absorbers. Mid-infrared spectral range is particularly interesting for these kinds of applications, due to the abundance of absorption bands of many broadband absorber chemical species.

The spectral features of broadband absorber gases vary for different species, ranging from spectral lines slightly merged over few cm^{-1} to broad bands spreading over 100-200 cm^{-1}.

In this chapter, two QEPAS-based sensors for broadband gases detection are reported. The first one targets three hydrocarbons, namely methane, ethane and propane, by exploiting the dynamic range of a single interband cascade laser source. The second one detects the P- and R- branches of nitrous oxide and several features of methane by employing a novel source, consisting in a monolithic array of 32 individually addressable distributed-feedback quantum cascade lasers.

4.1 Mid-Infrared broadband absorbers

Vibrational spectra of many atoms-molecules can be so dense that Doppler and pressure broadening make them unresolved at room temperature and atmospheric pressure. These molecules are referred to as broadband absorbers and their infrared absorption spectra can vary from a series of slightly merged lines to quasi-unstructured bands, spread over a spectral range $100 - 200\ cm^{-1}$ wide [1]. These spectra are the results of roto-vibrational transitions governed by selection rules which allow a variation in the rotational quantum number $\Delta J = -1$ (P-branch), 0 (Q-

branch), +1 (R-branch). These structures are typical in absorption spectra of hydrocarbons, pollutants, harmful gases and volatile organic compounds (VOCs). Figure 4.1 shows the absorption spectra of gases of major interest in mid-IR spectral range, simulated using HITRAN database [2].

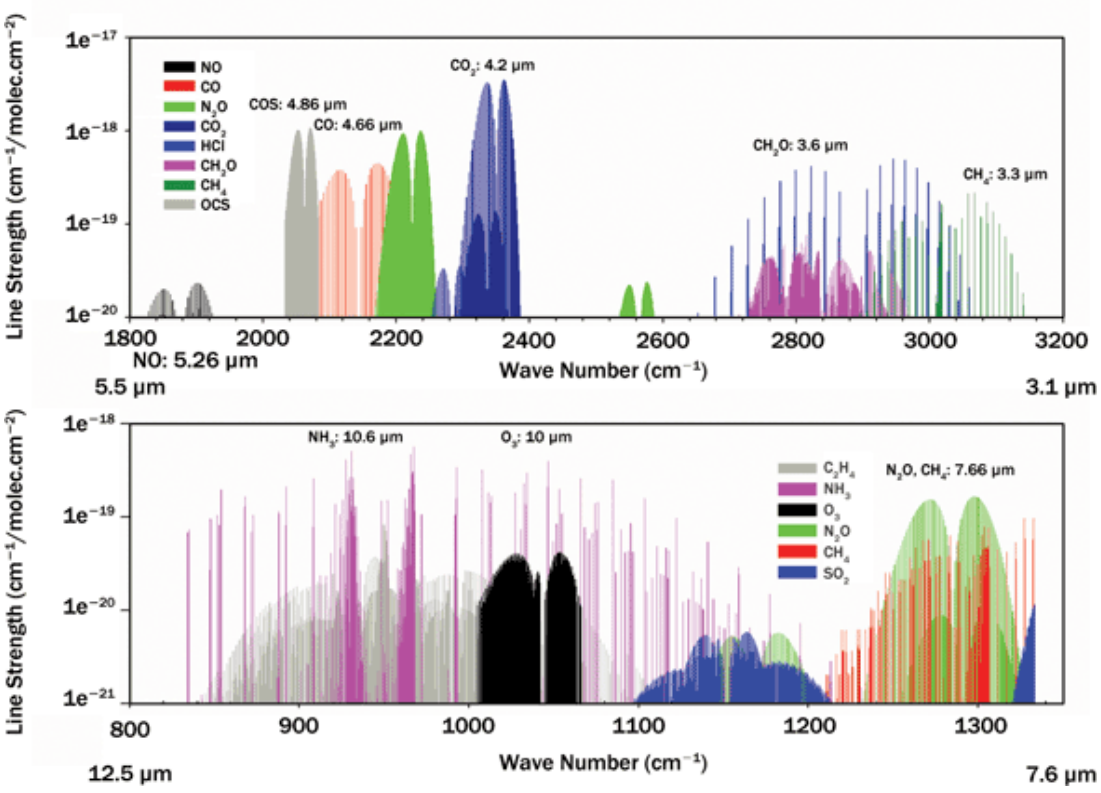

Figure 4.1 Simulation of absorption spectra of Nitric Oxide (NO), Carbon Monoxide (CO), Nitrous Oxide (N_2O), Carbon Dioxide (CO_2), Hydrogen Chloride (HCl), Formaldehyde (CH_2O), Methane (CH_4), Carbonyl Sulphide (OCS), Ethylene (C_2H_4), Ammonia (NH_3), Ozone (O_3), Sulphur Dioxide (SO_2) in the 3.1µm - 12.5µm spectral range by using HITRAN database.

In the investigated spectral range, Fig. 4.1 shows a strong overlap between the lines of the same molecule and between bands of different molecules. Nevertheless, the fingerprints of the compounds are clearly recognizable, allowing a selective detection.

Among the broadband mid-IR absorbers, a rising interest on volatile organic compounds (VOCs), greenhouse gases (GHGs) and explosives has developed in the last years.

Hydrocarbons methane (CH_4, also named hereafter C1), ethane (C_2H_6, C2), propane (C_3H_8, C3) and buthane (C_4H_{10}, C4) are VOCs playing a key role in petrochemical and oil&gas industry. Their monitoring represents one of the most efficient way to predict

production outputs, estimate reserves, assess raw material quality of source rocks and reservoirs [3]. The ratio between C1, C2, C3 and C4 hydrocarbons in the gas samples extracted by drilling shells strongly depends on their production process. When decomposition is biologically mediated, C1 is the dominant product (biogenic gas), and the other hydrocarbons are present only at trace levels [4]. When gas production is due to thermal decomposition (thermogenic gas) C2–C4 are more abundant, frequently comprising 10% or more of the gas. The mixing ratios of C2–C4 are as much as three orders of magnitude lower than C1 in unpolluted air. Leakage of C2 from subsurface reservoirs due to natural gas loss during gas and oil drilling, coal mining, gas venting, gas transmission, and transportation is substantial and has been estimated at 2.6–11 Tg/yr with a best estimate of 6 Tg/yr. Sources of C3 and C4 alkanes are not as well constrained but generally correspond with those of C2 and include biomass burning, oceans, and natural gas leakage [5,6].

Methane is also listed as a GHG gas. Pollutants and greenhouse gasses have a direct and indirect influence on climate changing, air quality and public health [7,8]. Most chemical agents worldwide known for causing ozone depletion, such as chlorofluorocarbons and hydrofluorocarbons, have been laid out in the Montreal Protocol on Substances that Deplete the Ozone Layer (MP), agreed in 1987 under the Vienna Convention [9]. Besides these chemicals, there are also gases primarily considered as natural atmospheric constituents which can also influence the ozone concentration. For example, although unregulated by the MP, nitrous oxide (N_2O), whose atmospheric concentration is of about 330 part-per-billion, releases active chemicals in the stratosphere that destroy stratospheric ozone through nitrogen oxide–catalyzed processes.

In the next sections, QEPAS-based sensors detecting C1, C2, C3 in a narrow spectral range and C1 and N_2O in a broad spectral range are described.

4.2 Hydrocarbons detection using a single interband cascade laser

Hydrocarbons are characterized by the C-H bond. The fundamental bands of the vibrational levels due to C-H bond stretching lie in the 3-4 μm spectral window [10], while the energy of the bond bending varies in the range 7-8 μm [11]. The exact values of transition energies and linewidths are determined by the boundary conditions related to the chemical structure of a specific hydrocarbon compound. The highest absorption cross-sections for both methane and ethane correspond to the C-H stretching and the most efficient light sources operating in the related wavelength range are ICLs. As a first step, we identified the spectral region that can be covered with a single ICL source, containing well resolved C1 and C2 absorption features and characterized by absorption cross-sections in the 10^{-18} (cm^2/mol) range.

In Fig. 4.2(a) and 4.2(b) C1 and C2 absorption cross-sections and related line-strengths are plotted in the range 2984-2992 cm^{-1} using data from the HITRAN database [2].

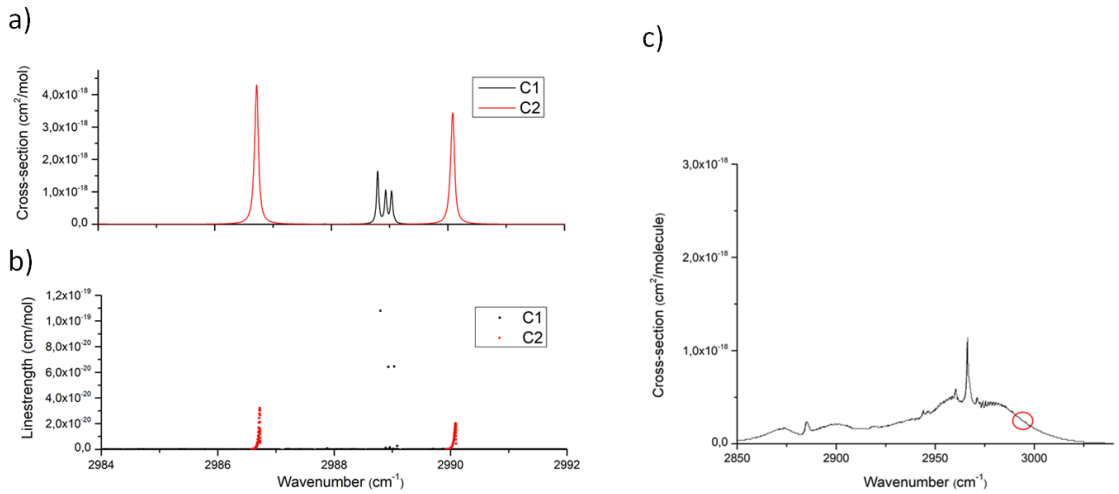

Figure 4.2 Absorption cross-sections (a) and corresponding linestrenghts (b) of methane (black curve – black dots) and ethane (red curve – red dots) at 50 Torr pressure in the range 2984-2992 cm^{-1} simulated using the Hitran database. Absorption cross-section of propane (c) in the range 2850 nm - 3100 nm, using PNNL database. The red circle highlights a spectral range around the one selected in Figs. 4.2(a) and 4.2(b).

These spectra were simulated for pure C1 and C2 at 50 Torr. At this pressure, the absorption line broadening due to collisions is low enough to allow distinguishing the fine structures of the absorption bands. Within a spectral range of 3.5 cm^{-1} there are two Lorentzian-like absorption lines of C2 (red dots in Fig. 4.2(b)) and in the middle three partially merged lines of C1 (black dots in Fig. 4.2(b)). Even though the line strength of a single C1 transition is higher with respect to the two C2 transitions, the collisional broadening at pressure of 50 Torr or higher gives rise to two isolated C2 absorption

features with a cross-section larger than the three-fold C1 structures. The spectral separation between the C1 three-lines structure and the two C2 lines guarantees a non-interfering detection between both species.

For the analysis of downhole gas mixture compositions, spectroscopic measurements are usually not performed on single gas component samples but on multi-component mixtures. As demonstrated in the Figs. 4.2(a) and 4.2(b), relatively small molecules such as C1 or C2 present well defined Lorentzian-like absorption features which can be easily detected by employing a wavelength modulation detection scheme. However, mixtures of larger molecules like C3 often result in strongly overlapping and broadened spectra. In this case, a selective identification of distinct components and the determination of their concentrations are difficult due to wavelengths interference effects. In Fig. 4.2(c) propane absorption cross-section of a dry mixture of 1000 ppm of C3 in pure N_2 are shown in the 2.85 µm - 3.1 µm range. Since C3 absorption features in the selected spectral range are not listed in the HITRAN database, PNNL database was taken as reference. The propane absorption cross-sections in a spectral range around the one selected for C1 and C2 detection (see the red circle in Fig. 4.2(c)) are almost five times lower in linestrength than ν_2^{C2} ($1.26 \cdot 10^{-18}$ cm^2/mol) at atmospheric pressure. Nevertheless, the lack of sharp Lorentzian-like features like ν_2^{C2} or ν_3^{C1} leads to a photoacoustic excitation intensity in wavelength modulation configuration sensibly low. In order to increase the C3 QEPAS signal, all the measurements on C2 and C3 mixtures need to be carried out at atmospheric pressure, where multiple absorption lines merge to build a spectrum composed of well-separated bands.

The identification of target lines represented in Fig. 4.2 led to a specific ICL design commercialized by Nanoplus, with a central emission wavelength of 3345 nm (2989 cm^{-1}). The ICL current dynamic range is I = 15-70 mA and the optimal operating temperatures range is from T = 5°C to T = 15°C. The ICL is mounted in a standard TO66 package equipped with a collimating lens (see Fig. 4.3). The beam emerging from the lens has a nearly perfect Gaussian power distribution, a diameter of 3 mm. The maximum power of ~11 mW has been measured at T = 5°C and I = 70 mA, with an electric power consumption of 0.273 W. A schematic of the sensor system is shown in Fig. 4.3.

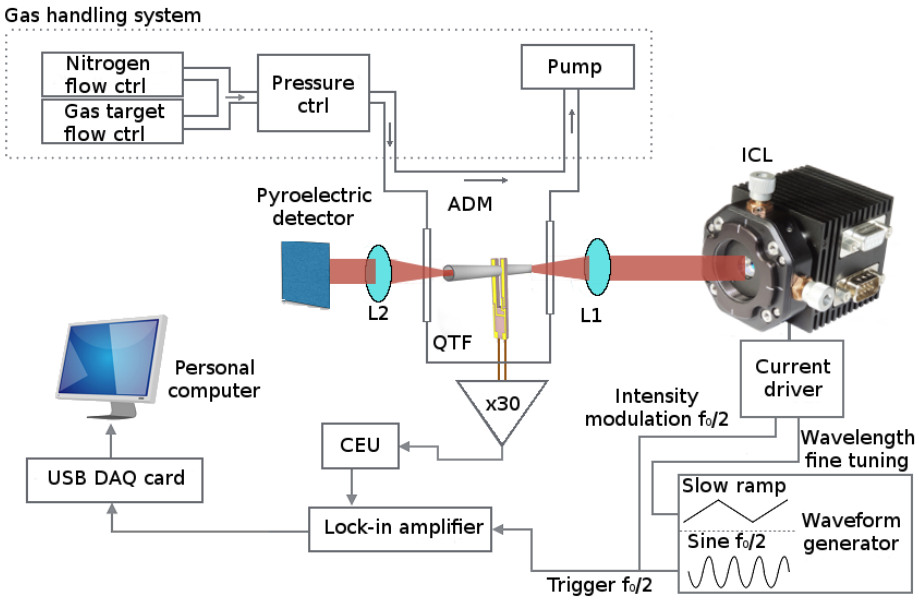

Figure 4.3 Schematic of the experimental apparatus. CEU - control-electronic-unit; ADM - acoustic detection module; L1, L2 –ZnSe lenses; ICL – intercascade laser.

The high quality of the laser beam allowed operation with a standard 32 kHz QTF (prong spacing of 0.3 mm and length of 3 mm) mounted in an on-beam double tube spectrophone configuration, constituting the spectrophone of the QEPAS sensor system. The acoustic detection module (ADM) consists of a stainless steel, cylindrical chamber with one inlet and one outlet connector to the gas line and it is equipped with two ZnSe windows having a 3-12 μm anti-reflection coating with a transmissivity of 93% at the laser wavelength. The spectrophone is positioned inside the ADM. The employed spectrophone shows a quality factor of Q = 2100 at atmospheric pressure and a resonance frequency for the QTF fundamental flexural in-plane mode of f_0 = 32741.5 Hz. The collimated light exiting the ICL is focused by means of a ZnSe lens (L1) into the ADM and passed through the spectrophone; L1 has a focal length of 7.5 cm and a transmittivity of 95% at 3345 nm. A gas line connects the ADM to the pump on the outlet side and to a pressure controller located at the inlet side. The pressure controller keeps fixed the downstream pressure of the targeted gas mixture into the ADM. The mixtures are generated by flow controllers and a constant water concentration of 1.7 % was guaranteed by a Nafion humidifier inserted on one of the gas lines. The light exiting from the ADM is re-collimated using a ZnSe lens (L2) and collected by a pyroelectric detector used for continuous monitoring of the laser power. The piezoelectric current

generated by the photoacoustic excitation is converted into a voltage signal and amplified by a factor 30 using a transimpedance amplifier (with a feedback resistor of 10 MΩ) and then sent to the Control Electronics Unit (CEU). The CEU is used to determine the main QTF parameters: the electrical resistance R, the quality factor Q, and the resonance frequency f_0. It is also used to transfer the signal coming from the transimpedance amplifier to the lock-in amplifier. The output analog signal from the lock-in amplifier is then digitalized by a National Instruments DAQ card (USB 6008) connected to a personal computer. A LabVIEW-based software acquires the temporal evolution of the QEPAS signal and the response of the pyroelectric detector.

4.2.1 Methane and ethane detection

To optimize the QEPAS detection scheme, we investigated the full ICL dynamic range to retrieve the most convenient experimental conditions for C1-C2 detection in current scan mode. A mixture of 1000 ppm of C1 in pure N_2 and a mixture of 1000 ppm of C2 in pure N2 were analyzed. 2f-wavelength modulation (WM) was employed as detection scheme since it is characterized by a background-free signal [12]. The ICL injected current I was modulated at half of the resonance frequency $f_0/2$ and the QEPAS signal was demodulated at the resonance frequency f_0 (2f-signal). Usually, the current sinusoidal excitation and the QEPAS signal are out of phase. For this reason, the demodulation of the QEPAS signal occurs at a detection phase φ_i maximizing the demodulated signal amplitude. The main results from this investigation showed that by operating at an ICL temperature of 15 °C, the laser emission wavelength is resonant with the C2 absorption line falling at 2986.25 cm^{-1} (ν_2^{C2}) at a laser current of I = 65.5 mA, while to target the strongest C1 absorption line peak at 2988.8 cm^{-1} (ν_3^{C1}) and the C2 line falling at 2990.1 cm^{-1} (ν_1^{C2}) the injected current have to be set at I = 48 mA and I = 35 mA, respectively. Thus, all three transitions ν_1^{C2}, ν_3^{C1}, ν_2^{C2} can be excited by keeping the laser operating temperature fixed at 15°C, exploiting the ICL current dynamic range. Once identified the ICL operating conditions to target the selected C1 and C2 absorption lines, the full sensor calibration procedure was performed.

The QEPAS response to the excitation of ν_3^{C1} at different pressures was firstly recorded. The data reported in Fig. 4.4(a) correspond to the 2f-QEPAS peak signals obtained

operating in wavelength modulation configuration and optimizing the modulation depth for each different operating pressure. For methane the strongest response to the photoacoustic excitation was achieved at a gas pressure of 200 Torr and a modulation amplitude of 130 mV peak-to-peak (Vp-p). The detection phase φ_1 maximizing the QEPAS signal related to ν_3^{C1} excitation was 99.91°. These operating parameters were used for all the following C1 measurements.

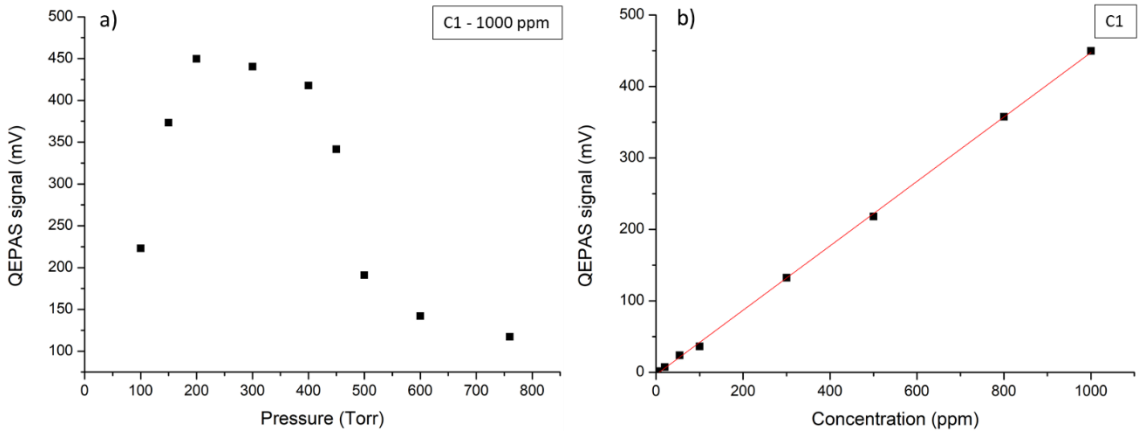

Figure 4.4 a) 2f-signal peak values related to ν_3^{C1} at their optimum modulation depth for different pressures ranging from 100 Torr to atmospheric pressure; b) linearity of the 2f-signal peak values obtained at 200 Torr over a range of C1 concentrations from 4 ppm to 1000 ppm in pure N_2.

Once determined the best operating conditions in terms of gas pressure and modulation depth, the 2f-signal peak signals at different C1 concentrations were recorded. The data reported in Fig. 4.4(b) demonstrate a very good linearity for the C1 sensor over a range of concentrations from 4ppm to 1000 ppm. A linearity coefficient of 0.46 mV/ppm was extracted from the linear fit and a negligible intercept, with a 1-σ noise fluctuations of 0.073 mV.

In Fig. 4.5(a) and 4.4(b) two representative acquisitions of C1 signal for 1000 ppm and 4 ppm respectively are shown.

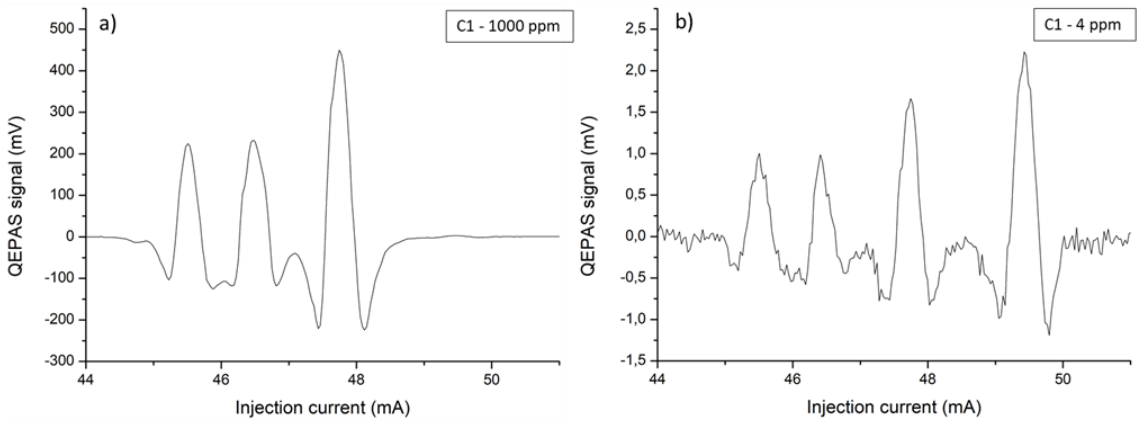

Figure 4.5 a) 2f-signal corresponding to a wet mixture of 1000 ppm-C1 in pure N_2; b) 2f-signal corresponding to a wet mixture of 4 ppm-C1 in pure N_2.

In Fig. 4.5(b) it is clearly visible the presence of a water absorption line falling at 2988.61 cm^{-1} [2], corresponding to at a laser injected current I= 49.5 mA, with a line strength of $1.1 \cdot 10^{-22}$ cm/mol, giving rise to a 2f-signal with a peak value of 2.25 mV. This signal is barely visible in Fig. 4.5(a) due to the much higher C1 concentration. A very good correspondence between the absorption features listed in the HITRAN database and the 2f QEPAS-signal structures due to methane absorption was found. The background signal not involving gas absorption lines has comparable 1-σ noise fluctuations at different C1 concentrations.

For ethane detection calibration, line ν_2^{C2} was targeted for determining the sensitivity of the sensor with respect to C2. The calibration procedure for C2 is similar to the one illustrated for C1. The QEPAS response at different working pressures was firstly investigated at C2 concentration of 100 ppm. The first evidence is that the optimum gas mixture pressure, found at 300 Torr, provides a QEPAS signal only ~1.3 times higher with respect to the value recorded at the atmospheric pressure (Fig 4.6(a)), differently from methane where at 1 atm the QEPAS signal drops down by ~70% with respect of the maximum signal recorded at 200 Torr. This means that the C2 sensor works efficiently also at atmospheric pressure which is advantageous for in situ applications.

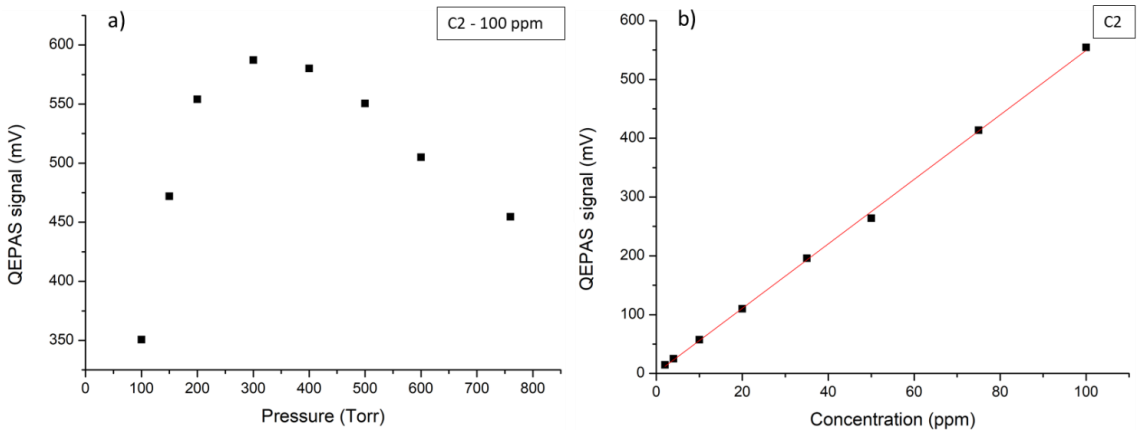

Figure 4.6 a) 2f-signal peak values related to ν_2^{C2} at the related optimum modulation depths for different pressures, from 100 Torr to atmospheric pressure; b) linearity of the 2f-signal peak values obtained at 200 Torr over a range of C2 concentrations from 2 ppm to 100 ppm in pure N_2.

If 200 Torr is the optimum working pressure for methane, the pressure controller has proven to have the smallest fluctuations at this pressure and the QEPAS signal from ν_2^{C2} is ~4% smaller with respect to the highest signal recorded at 300 Torr (see Fig. 4.6(a)). Hence a pressure of 200 Torr was chosen for performing the measurements for both C1 and C2. For C2 the optimum modulation depth results Vp-p = 130 mV and detection phase φ_2 =166.15°. The C2-calibration curve is shown in Fig. 4.6(b) and the linearity of the QEPAS response was demonstrated from 100 ppm down to 2 ppm, with a linearity coefficient of 5.54 mV/ppm and a negligible intercept. Different from methane, ethane shows a broadband background absorption signal due to the presence of several absorption features with a small linestrength in the ICL operation spectral range, which can be compared to the signal at 1000 ppm for methane (see Fig. 4.5(a)) with the signal at 100 ppm for ethane (see Fig. 4.7(a)).

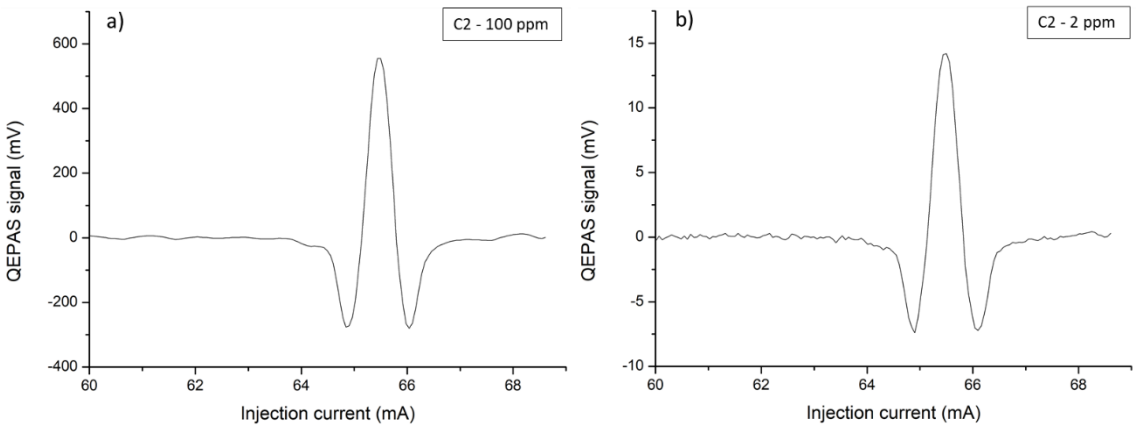

Figure 4.7 a) 2f-signal corresponding to a wet mixture of 100 ppm-C2 in pure N_2; b) 2f-signal corresponding to a wet mixture of 2 ppm-C2 in pure N_2.

By comparing Figs. 4.7(a) and 4.7(b), it can be noticed that the broadband background absorption levels off as the ethane concentration decreases. At 200 Torr and 2 ppm ethane concentration, the 1-σ signal value calculated far from the ν_2^{C2} 2f-peak is 0.14 mV, only about two times the noise level measured for a 1000 ppm C1/N_2 mixture.

In order to evaluate the ultimate detection limit and the long-term stability of the QEPAS sensor for independent detection of C1 and C2, an Allan-Werle deviation analysis was performed (see Appendix). Two different measurements of the QEPAS signal in pure N_2 were acquired and averaged by setting the injected current at 48 mA and 65.5 mA, which correspond to a laser emission resonant with ν_3^{C1} and ν_2^{C2} absorption peaks, respectively.

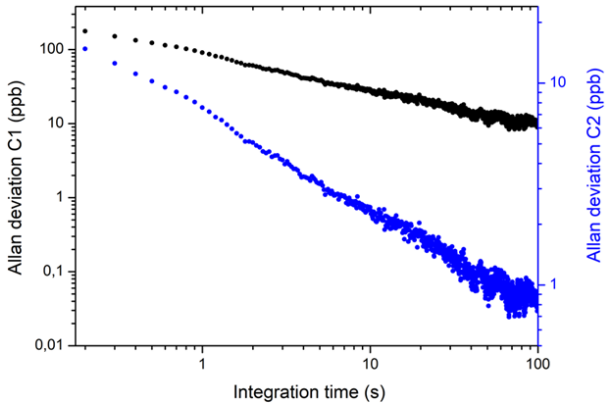

Figure 4.8 Allan-Werle Deviation Analysis (in ppb) for methane (black dots) and ethane (blue dots).

In Fig. 4.8 Allan-Werle deviation analysis for C1 (black dots) and C2 (blue dots) are displayed for lock-in integration times up to 100 s. Both trends closely follow a $1/\sqrt{t}$ dependence over the entire duration of the measurement series, which indicates that thermal noise of the QTF remains the dominant noise source and the sensor allows data averaging without base line or sensitivity drift up to 100 s time scale.

For a 1 s integration time for on-line measurements, the detection limit for methane is ~ 90 ppb. This is a value well below the sensitivity needed for a sensor aimed at hydrocarbon detection at a well site, where C1 concentrations are expected to be generally well above the ppm scale. On the other hand, a detection sensitivity of 7 ppb at 1 sec of integration time was achieved for C2 and this represents a record for the

QEPAS technique and opens the way to the implementation of QEPAS sensors for exploring and identifications of ethane reservoirs, an application of strong interest by petrochemical and plastic industries. Considering these aspects, an unbalanced wet mixture containing 990 ppm C1, 10 ppm C2 in pure N_2 was used to perform the first test of a fast C1/C2 detection scan.

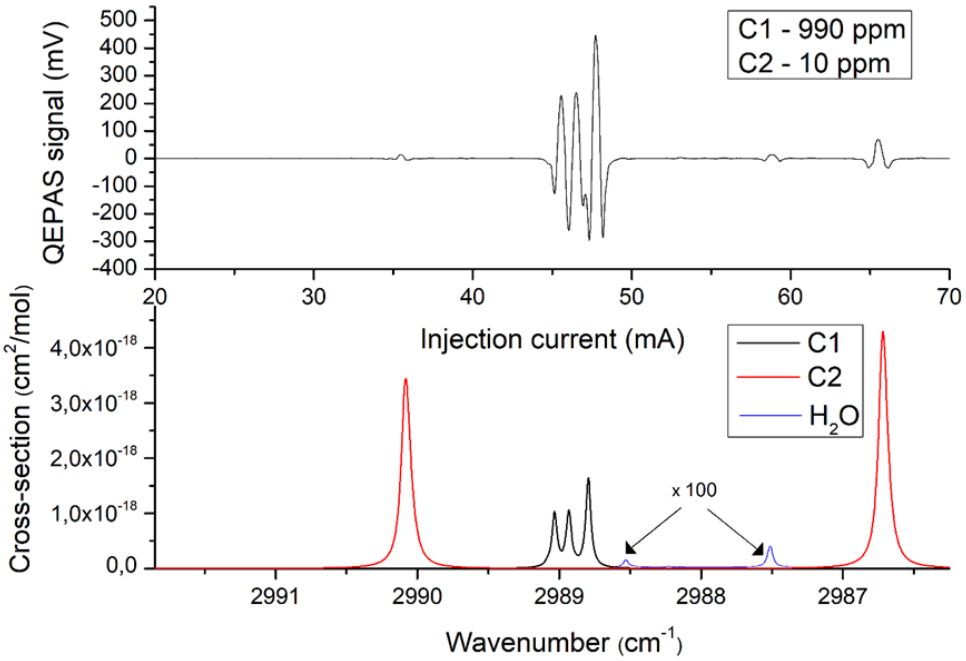

Figure 4.9 Top panel: QEPAS 2f-signal for a wet mixture of 990 ppm-C1 and 10 ppm-C2 in pure N_2 with adjusted detection phase in correspondence of ν_3^{C1} (φ_1) and ν_2^{C2} (φ_2). Bottom panel: absorption cross-section for C1 and C2 obtained using the HITRAN database. Two weak H_2O are also shown (blue curve), by multiplying the related cross-sections by a factor of 100.

In the upper panel of Fig. 4.9, the QEPAS signal acquired for an ICL current span from 20 mA to 70 mA at T = 15°C is displayed. The working pressure was fixed at 200 Torr and the modulation amplitude at 130 mVp-p. The second derivative profile of ethane absorption features ν_1^{C2}, ν_2^{C2} and the second derivative shape of the three-lines structure from methane are clearly visible and the spectral separation is coherent with the absorption cross-section graph for both C1 and C2 simulated using the HITRAN database and shown in the lower panel of Fig. 4.9. In order to maximize the QEPAS response of the C1 and C2 lines, the optimal detection phases identified for each gas were used during the current scan in the proximity of the related absorption features. A ν_3^{C1} 2f-signal peak of 455 mV and a ν_2^{C2} 2f-signal peak of 63 mV were obtained as

expected from the sensor calibration. Furthermore, the full spectral scan over the ICL dynamic range showed the presence of barely visible water line at I = 59 mA, different from the one previously observed at I = 49.5 mA.

The detection scheme is versatile, because in one single current scan C1 and C2 can be independently detected at sub-ppm scale and can also deal with unbalanced mixtures in which the methane concentration is two orders of magnitude or even higher in concentration with respect to ethane.

More interesting is a comparison between two or more broadband absorber molecules, like C2 and C3, that can be found in downhole mixture compositions.

4.2.2 Propane detection and analysis of broadband absorbers spectra

In this section a detailed study of the next in line hydrocarbon, the propane (C3), will be presented. In particular, the attention will be focused on how its broadband spectrum interacts with the C2 background signal.

The lock-in phase maximizing the C3 QEPAS signal was φ_3 =107.25°. In Fig. 4.10 the QEPAS spectra related to the C3 broadband spectra measured at atmospheric pressure and for different C3 dry concentrations, ranging from 1000 ppm to 200 ppm in pure N_2, are plotted.

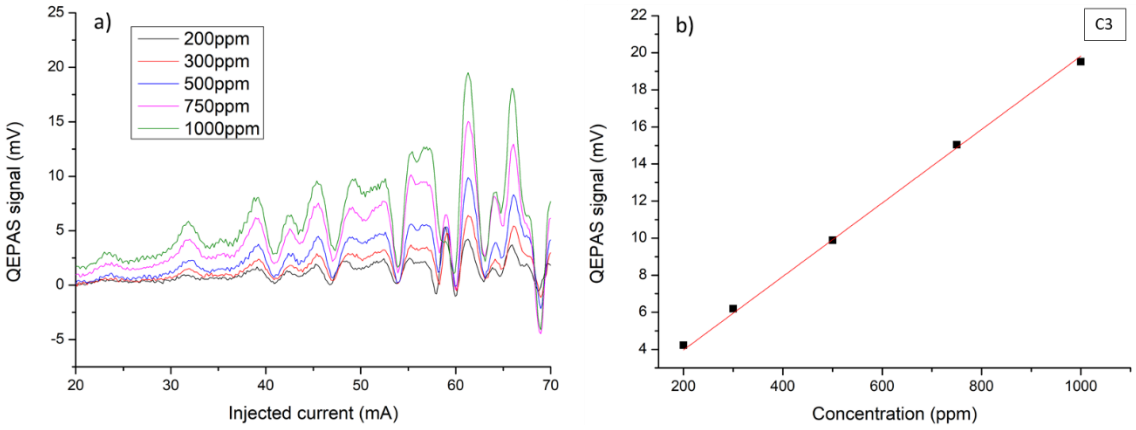

Figure 4.10 2f-QEPAS spectra (a) measured for different C3 concentrations from 1000 ppm to 200 ppm in pure N_2, at the atmospheric pressure, in the laser current range 20-70 mA. 2f-signal peak values (black

square dots) related to the absorption feature falling at I =61.3 m (b) over a range of C3 concentrations from 1000 ppm to 200 ppm and linear fit (red solid line).

These spectra were obtained by scanning the laser injected current from 20 mA to 70 mA at T=15°C and employing a modulation depth of 300 mVp-p. Fig. 4.10(b) demonstrates the linearity of photoacoustic response as a function of the C3 concentration, extracted for the peak of the QEPAS spectrum ν_4^{C3} located at I = 61.3 mA. The linearity coefficient is 0.0191 mV/ppm. The detection limit extracted by comparing the QEPAS ν_4^{C3} peak signals with a 1σ noise level results in < 3 ppm for a1s integration time. It was verified that each peak of the C3 spectrum exhibits a linear QEPAS response with C3 concentrations, as observed in Fig. 4.10(a). The QEPAS signal measured for a pure N_2 mixture is flat within the ICL current dynamic range and comparable with the noise level. A flat background noise and QEPAS signal scaling linearly with the gas target concentration are mandatory requirements to compare C2 and C3 backgrounds. The QEPAS signal *Y(λ)* acquired for a mixture of n gases (C2 and C3) for a given wavelength spectrum can be assumed to be the sum of the QEPAS signals related to the individual gases:

$$Y(\lambda) = \sum_{i=0}^{n} A_i \, X(\lambda)_i \; = A_2 \, X(\lambda)_{C2} + A_3 \, X(\lambda)_{C3} \tag{4.1}$$

where *Y(λ)* is the acquired QEPAS signal (in mV), A_i is the concentration of the *i*-th gas (in ppm) and X_i the related QEPAS spectrum, in mV/ppm unit [13]. If the operating temperature is set to 15°C, the laser emission wavelength is related to the drive current. In order to discriminate both contributions in C2-C3 mixtures, an injected current range from 35 to 60 mA was selected, in which range no strong C2 features are present and both C2 and C3 absorption broadband backgrounds can be easily compared (see Fig. 4.11(a)).

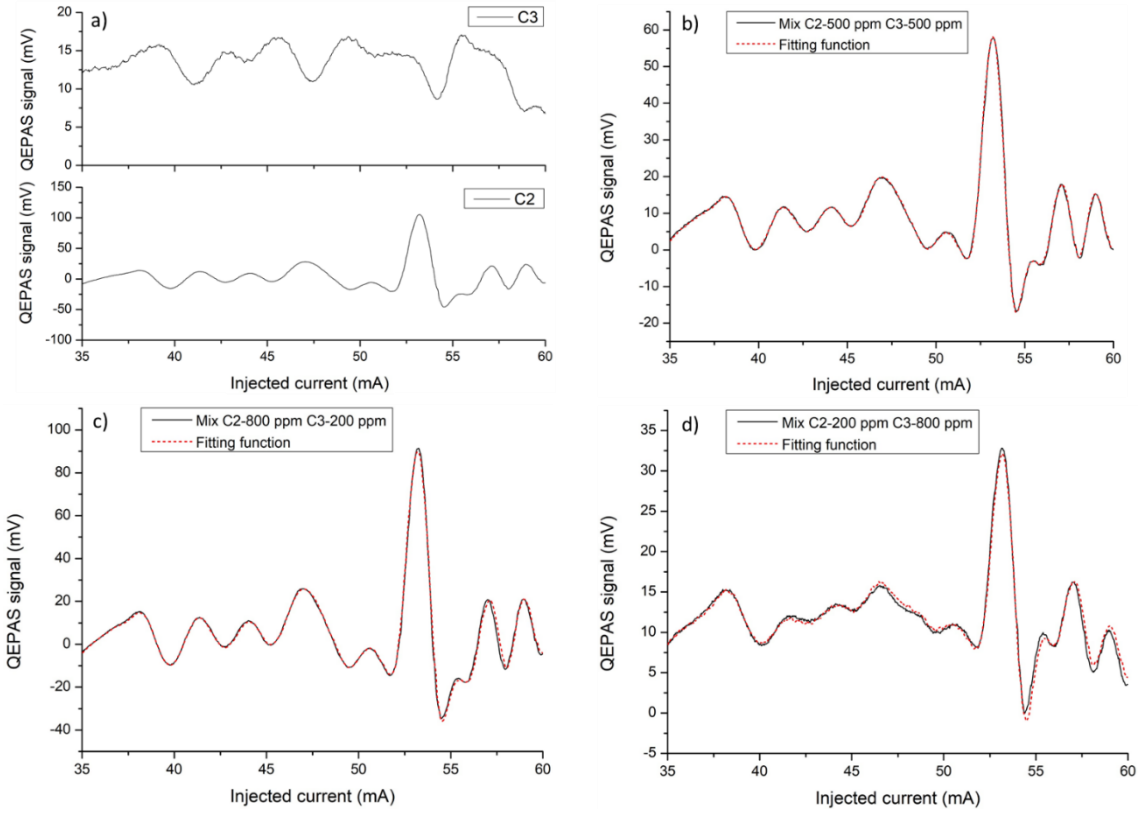

Figure 4.11 (a) Top panel: 2f-signal for 1000 ppm-C3:N_2 acquired in the laser injected current range 35-60 mA. Bottom panel: 2f-signal for 1000 ppm-C2:N_2; (b) 2f-signal for a dry mixture containing 500 ppm of C2 and 500 ppm of C3, in pure N_2; (c) 2f-signal for a dry mixture containing 800 ppm of C2 and 200 ppm of C3 in pure N_2; (d) 2f-signal for a dry mixture containing 200 ppm of C2 and 800 ppm of C3 in pure N_2.

The detection phase used for these measurements is the one maximizing the C3 QEPAS signal, i.e., φ_3 =107.25°: in this way we also slightly reduced the intensity of the C2 background signal. However, it was verified that the C2 background signal detected at φ_3 is still linear as function of C2 concentrations. The reference QEPAS spectra used for the fitting procedure using Eq. (4.1) are the C2 and C3 signals recorded at 1000 ppm in pure N_2 concentration, therefore Eq. (4.1) becomes:

$$Y = a\, X_{1‰}^{C2} + b\, X_{1‰}^{C3} \tag{4.2}$$

where a and b are the fraction of 1000 ppm of the reference spectra. The first validation test of this multi-gas detection approach was made using dry mixtures composed of: i) C2-500 ppm, C3-500 ppm in pure N_2 (mix#1); ii) C2-800 ppm, C3-200 ppm in pure N_2 (mix#2); iii) C2-200 ppm, C3-800 ppm in pure N_2 (mix#3). By fitting the measured QEPAS signals with Eq. (4.2), using the algorithm of the linear least squares it is

possible to extract the C2 and C3 concentration values. In Figs. 4.11(b), 4.11(c), and 4.11(d) the QEPAS spectra and the related fits for all the three gas mixtures are shown. The calculated concentration values are listed in Table 4.1. In brackets the 95% confidence interval uncertainties are reported.

Table 4.1: Actual and calculated C2 and C3 concentration for the investigated gas mixtures.

Mixt.	C_2 conc. (ppm)	C_3 conc. (ppm)	Calculated C_2 conc. (ppm)	Calculated C_3 conc. (ppm)
1	500	500	487.02 (±1.4)	520.00 (±2.5)
2	800	200	828.98 (±3.8)	208.01 (±6.8)
3	200	800	199.98 (±1.7)	831.47 (±2.9)

The differences between the fitting parameters, i.e. the calculated C2 and C3 concentrations and the nominal concentrations expected, remain below 5% and are mainly due to uncertainties in the certified gases flows used for producing the mixtures (especially for flows as low as 8 sccm, as used in our experiments). The obtained results successfully demonstrate the feasibility to perform photoacoustic C2/C3 gas detection by fitting the QEPAS spectra measured for the gas mixtures. Among different valid approaches such as multivariate analysis or machine learning, a fitting procedure based on a linear combination of reference spectra still represents the most straightforward strategy. Since in the investigated spectral range C1 is characterized by well isolated absorption peaks and no background, we successfully determined C1, C2 and C3 concentrations in humidified and dry gas mixtures respectively, using pure nitrogen as gas carrier. The next step would be a detailed investigation of C1/C2/C3 mixtures in a large dynamic range of concentration from several % to few ppb. Successively, butane (C4) could be added to the gas mixture in order to analyze gas samples as similar as possible to the natural gas composition. All these tasks aim to monitor natural gas sample compositions in situ and in real time for petrochemical applications.

4.3 Wide-spectral range QEPAS employing a monolithic DFB-QCL array

In Section 4.2 quartz-enhanced photoacoustic detection of methane and ethane in the ppb range and propane in the ppm range has been performed by employing a single

interband cascade laser emitting at 3345 nm. However, there are many cases where the tuning range of a single interband or quantum cascade laser is inadequate. As shown in Fig. 4.1, many-atoms molecules exhibit broad spectral structures which cannot be identified by targeting a single absorption line with a single laser. The detection of such molecules requires an investigation over a spectral region wider than the typical tunability range of a single ICL or distributed feedback-QCL (DFB-QCL). This is also the case of the detection of contaminants altering the shape of the spectrum of the primary broadband absorber gas and the relative intensity of the QEPAS signals composing the total spectrum. Finally, in fields ranging from atmospheric science to process control, it is often the quantitative assessment and/or the ratios of various components in multi-gas mixtures that are critical. One notable example is mapping the concurrent atmospheric changes in climate forcing species such as H_2O, CO_2, CH_4 and N_2O.

For high resolution spectroscopy of broadband absorbers, the commonly employed laser sources tunable in a wide spectral range are external cavity QCLs (EC-QCLs) or ICLs (EC-ICLs) [14,15]. The external cavity incorporates typically a separate grating for wavelength selectivity [16]. Nevertheless, mechanical instability of moving parts leads to beam displacement and poor spatial beam quality [17].

In this section a QEPAS sensor based on a monolithic DFB-QCL array composed of 32 individual lasers fabricated on a single QCL chip is described, aimed to detect N_2O and CH_4 gas traces in the 1190-1340 μm spectral range.

In contrast to EC-QCLs which tend to be limited in a full broadband tuning speed to only a few scans per second, the speed and stability advantages of a monolithic array of distributed-feedback quantum cascade laser (DFB-QCLs) has been demonstrated. In DFB-QCL arrays, each laser is individually addressable to allow for fast purely electrical switching from wavelength to wavelength [18]. The unique combination of fast tuning speed, large tuning range and stability in QCL arrays is a key enabler for fast broadband absorber detection. A single array contains 32 individually addressable QCLs; each QCL emits at a slightly different wavelength by design. Several arrays can be further beam-combined into a source with broader coverage [19]. As shown in Fig. 4.12, all lasers in an array are fabricated on the same semiconductor chip and do not require any external feedback for lasing or wavelength selection. The emitted

wavelength is selected by electrically addressing different lasers, making the process of wavelength tuning inherently fast and reproducible.

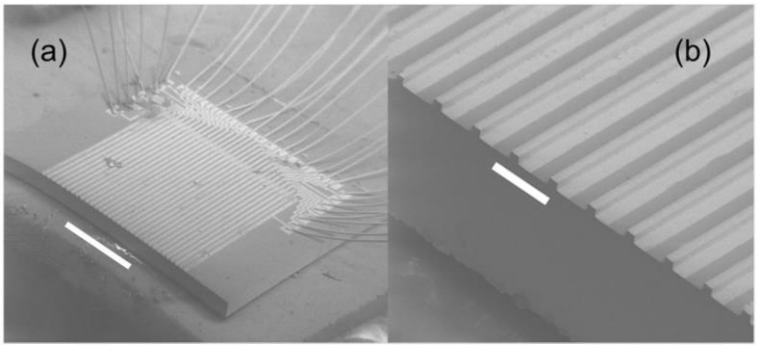

Figure 4.12 (a) SEM image of an array with 32 lasers. The diagonal stripes are individual laser ridges, and there are wirebonds connected to bonding pads in the upper right portion of the image. The white bar corresponds to 1mm. (b) Magnified view of the laser ridges with the front facet of each laser visible. The white bar corresponds to 100μm [20].

The output from individual QCLs are overlapped by using spectral beam combining optics [20] integrated into the laser array package. The laser package, including the QCL chip, a thermo-electric cooler (TEC) for temperature regulation of the array and the optical elements necessary for beam combining, measures 1”x2”x0.5”. A custom laser driver allows the individual control of the different lasers within the array, enabling purely electrical tuning of the source by selecting which laser emits at any time. It consists of a single electronic board that measures 6”x4” containing an array of 32 gate drivers controlled by a Field-Programmable Gate Array (FPGA). The lasers are operated in a pulsed mode. Pulsed operation allows for low power consumption and requires no external laser cooling. The lasers can be turned on and off in arbitrary sequences, as long as the duty cycle per laser remains < 1% and the overall array duty cycle is kept below 30%. For each QCL, the drive voltage was set to a value ensuring the highest optical power output. The emission spectra of each QCL acquired with a Fourier-transform interferometer in a rapid-scan mode, with a resolution of 0.125 cm^{-1}, are shown in Fig. 4.13(a).

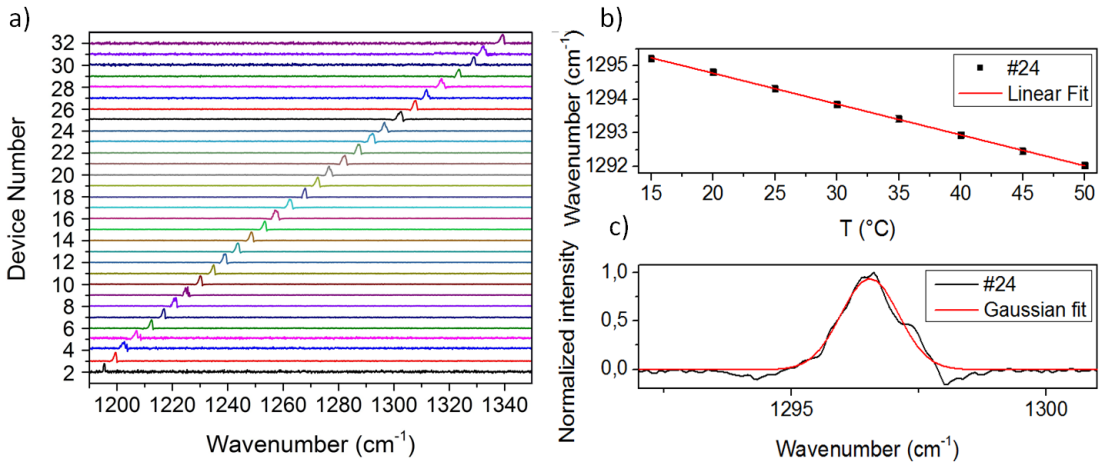

Figure 4.13 (a) Normalized intensity spectra of the QCLs composing the array; (b) example of temperature tuning of the peak wavelength emission of one QCL of the array (device #24) and (c) Gaussian fit of its normalized emission spectrum at 25°C operating temperature.

The QCL array emission covers a spectral range from 1190 cm^{-1} to 1340 cm^{-1}, with steps of < 5 cm^{-1} between adjacent laser devices. With 300 ns-wide pulses, all devices exhibit a spectral linewidth of about 1.5 cm^{-1} (see Fig. 4.13(c)) due to the intra-pulse frequency chirp of the laser during the pulse duration as well as the potential presence of two longitudinal modes corresponding to the two possible DFB band-edge modes. QCL chip temperature is set by a TEC controller (2"x2" electronic board) and can be used to tune the laser center wavelength. As shown in Fig. 4.13(b), by linearly fitting the wavenumber corresponding to the spectrum peak as a function of the operating temperature, a rate of ~0.09 cm^{-1}/°C was measured. Laser driver and TEC controller are operated by LabVIEW-based software that enables programming of the QCL array sequence and control of temperature tuning. The QEPAS sensor is schematically depicted in Fig. 4.14.

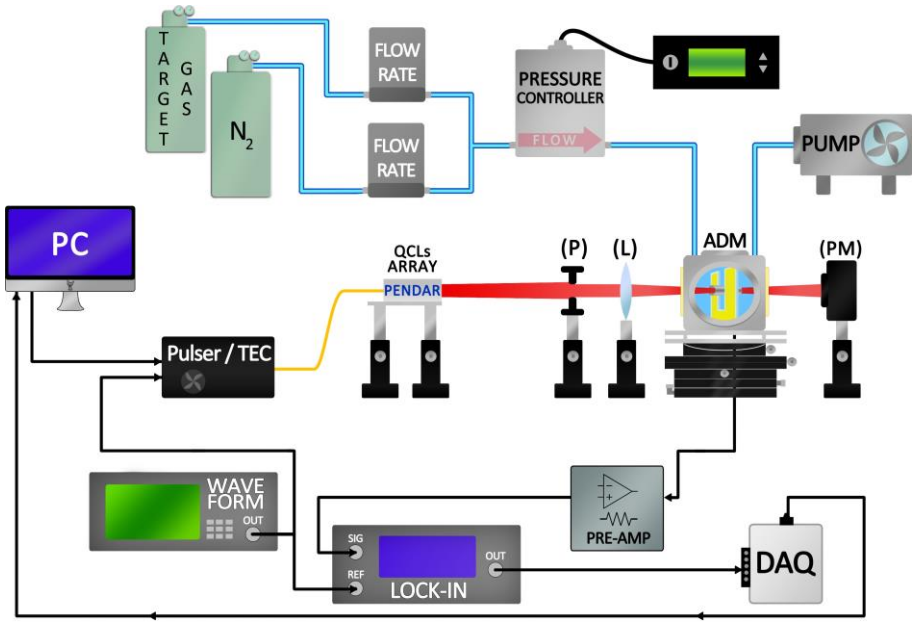

Figure 4.14 Schematic of QEPAS sensor for N2O detection. P – pinhole; L – lens; ADM - acoustic detection module; PM – power meter; TEC – temperature controller; DAQ – data acquisition board; PC – personal computer. The QCL array was provided by Pendar Technologies.

The laser beam exiting the array enclosure was spatially filtered by a pinhole and focused between the prongs of a custom quartz tuning fork by means of an AR-coated ZnSe lens with a 50mm focal length. A pyroelectric camera (mod. Spiricon Pyrocam III-C) with a spatial resolution of 100 μm was placed in the focal plane of the ZnSe lens to acquire and measure the beam profiles of the focused laser spots. As an example, the positions of the center of the beam of 5 devices and the corresponding diameters are reported in Fig. 4.15.

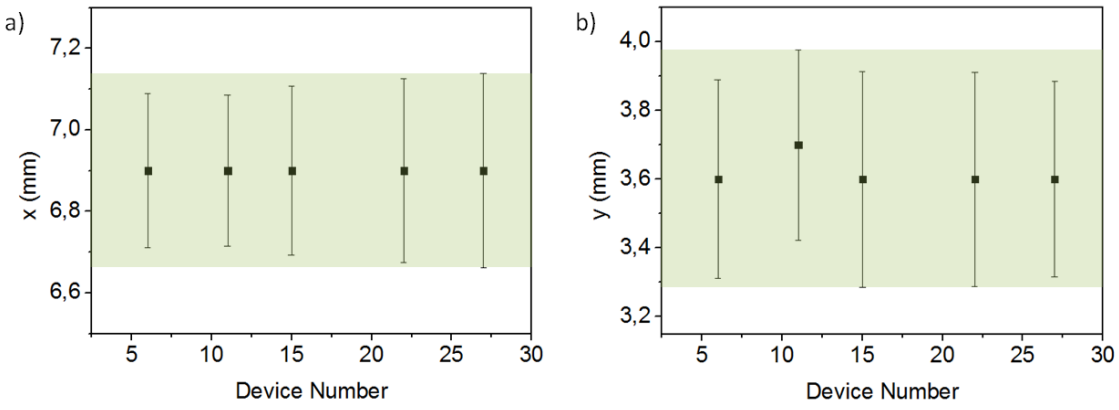

Figure 4.15 Beam center position (squares) and corresponding beam diameter (bars) along x- (a) and y-direction (b) for a sample of 5 devices, in the focal plane of the ZnSe lens. The shaded areas represent the x- and y-dimension of the overall focused beam

Switching between different devices, shifts of the spot center positions of ~ 100 μm along y-direction were observed and an overall focused beam diameter of~ 460 μm in x-direction and 690 μm y-direction. These measurements determine the prong spacing of the tuning fork to be selected. The laser light must not hit the QTF prongs while switching from one QCL to another, otherwise a background signal unrelated to the gas absorption will be generated. For this reason, custom QTF #6 (see Section 3.1.2), having a prong spacing of 1 mm, was selected. Such a QTF showed its best performance when operated at the first overtone flexural mode falling at 25,391.2 Hz at atmospheric pressure with a quality factor of 20,900. The QTF was acoustically coupled with two micro-resonator tubes for pressure wave amplification. The micro-resonator tubes providing the highest signal-to-noise ratio (SNR) enhancement have an internal diameter of 1.52 mm and a length of 5.30 mm and were positioned on-beam, located 200 μm from the QTF. The QEPAS spectrophone composed of a QTF and micro-resonator tubes was enclosed in a gas cell, through which the gas flowed at a controlled rate and pressure of 30 sccm and 760 Torr, respectively. The QTF piezocurrent signal was transduced and amplified by a transimpedance amplifier (feedback resistance R_{fb}=10MΩ) and demodulated by a lock-in amplifier. An external waveform generator was employed to trigger both the laser pulses and the lock-in demodulation at the QTF resonance frequency. The width of the QCL pulses was set at 300 ns which, combined with the operating repetition rate of 25,391.2 Hz, corresponds to a duty cycle of 0.75% and the lock-in amplifier integration time was set at 100 ms for all measurements.

4.3.1 Nitrous oxide P-branch and R-branch detection

The described QEPAS sensor was employed as a first step to detect the P-branch and the R-branch of nitrous oxide, falling in the 1225-1330 cm^{-1} spectral range [21]. Each branch consists of a series of absorption lines spectrally separated by ~ 1 cm^{-1}. No Q-branch appears due to selection rules [1], as shown in the simulation obtained by using HITRAN database in Fig. 4.16 (red solid line) [2]. QEPAS measurements were performed by tuning the operating temperature of each QCL from 15°C to 50°C in 3°C steps and switching the lasers in sequence, in order to sweep the overall array spectral range with a resolution of 0.27 cm^{-1}, while a certified concentration of 1000 part-per-

million (ppm) N_2O:N_2 is flowing in the gas cell. For each operating temperature, the QCLs optical power focused between the QTF prongs was preliminary measured to generate a QCL array normalized optical power curve. The acquired QEPAS signals scaled to this normalized curve are plotted in Fig. 4.16 (black dots) and compared with the simulated absorption spectrum.

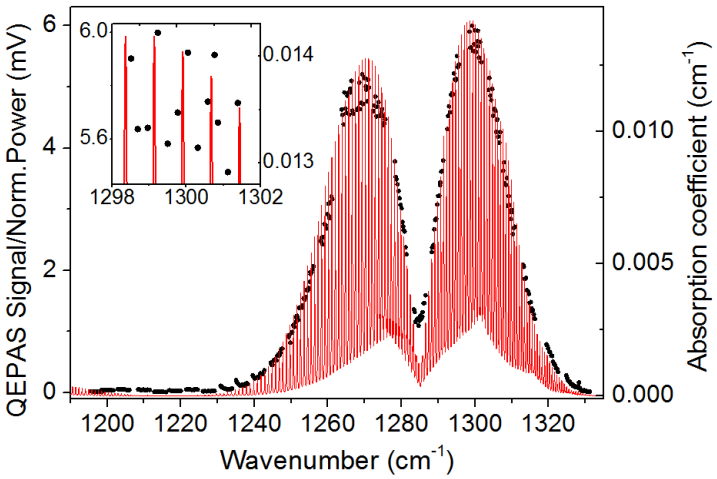

Figure 4.16 Comparison between the normalized QEPAS signals scaled to the normalized optical power, measured for a concentration of 1000ppm N_2O:N_2 while tuning the operating temperature of the QCL array (black dots, left y-axis) and the spectrum simulated at the same N_2O concentration by using the HITRAN database (red solid line, right y-axis). Inset: zoom on a narrow spectral range centered at 1300 cm^{-1}.

QEPAS measurements exhibit an excellent match with the simulated absorption spectrum in the investigated spectral range, accurately reconstructing the N_2O P- and R-branches centered at 1270 cm^{-1} and 1298 cm^{-1}, with a minimum at 1287 cm^{-1} corresponding to the forbidden Q-branch. The collected data mimic single absorption lines separated by ≈1 cm^{-1}, as highlighted in the inset of Fig. 4.16. Scanning the QCLs and tuning their temperature we measured comparable signal fluctuations due to photo-thermal induced noise confirming that the beam alignment is preserved while the array is scanned across its wavelength range by turning on of different lasers and tuning of the array temperature. This comes as a result of the use of a beam-combined QCL-array in conjunction with the external pinhole-lens system and the use of a custom QTF with a 1 mm prong spacing. The time required to produce the spectrum reported in Fig. 4.16 was 120 min.

Gases with broad absorption features justify the implementation of a rapid scan detection scheme even with a lower resolution in recovering the gas spectrum. To demonstrate this capability, a fast QCL switching mode was tested. In this mode, QEPAS measurements were performed by operating all devices at a fixed temperature set at 25°C. The nitrous oxide absorption spectrum was acquired by switching the individual laser composing the array sequentially. The acquired QEPAS signals have been scaled by the corresponding measured QCL array normalized optical power curve and are plotted in Fig. 4.17 (black squares). In this case, the fine structure of the absorption spectrum is no longer distinguishable, but the data obtained reproduce well the envelope of the simulated absorption bands shown in Fig. 4.16. A trace gas standard generator was used to produce different N_2O concentration levels, using N_2 as the diluting gas and starting from a certified 1000 ppm N_2O in N_2 mixture. In Fig. 4.17 the measurements corresponding to 400ppm, 600ppm, 800ppm and 1000ppm N_2O:N_2 are plotted, as well as the signal acquired for pure N_2.

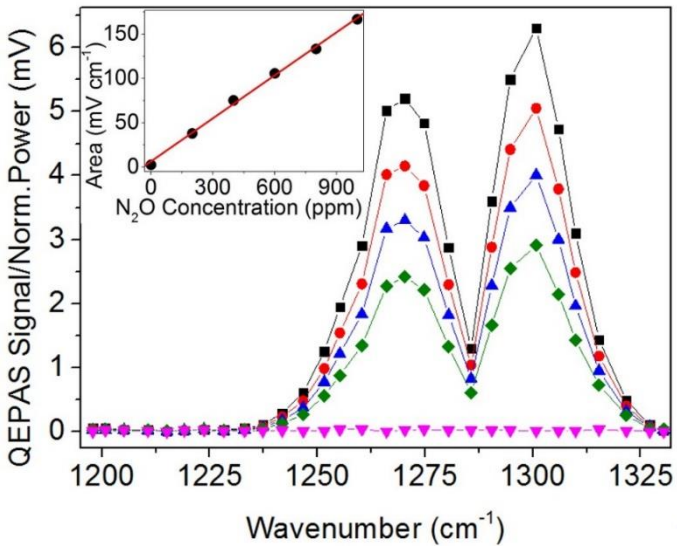

Figure 4.17 1000ppm (black squares), 800ppm (red dots), 600ppm (blue triangles) and 400ppm (green diamonds) N_2O QEPAS signal normalized by the laser optical power, plotted as a function of the laser peak wavenumber. The operating temperature of the QCL array was fixed at 25°C. The QEPAS signal measured for pure N_2 (pink triangles) is also reported. Solid lines are visual guides. Inset: Area underneath the QEPAS spectrum in $mV \cdot cm^{-1}$ units measured for each N_2O concentration (black dots) and the corresponding best linear fit (red line).

The shape of the QEPAS signal is preserved as the N_2O concentration is varied, while its intensity scales linearly with concentration. For each N_2O concentration, the total

measurement time was 8 min, obtained considering ~15s of QEPAS signal measurements for each QCL.

A calibration curve can be obtained by linearly fitting the area underneath the QEPAS signal curve, as a function of the N_2O:N_2 concentration. When targeting 200 ppm N_2O:N_2 a total area A of 31.1 mV·cm^{-1} was measured. Comparable 1-σ QEPAS signal fluctuations of ~2μV were measured for each QCL. By using the law of the propagation uncertainty, the standard deviation of A results in a σ_A= 0.05 mV·cm^{-1} and turns out to be proportional to the 1-σ noise of QEPAS signal. The resulting signal-to-noise ratio SNR is A/σ_A=622, corresponding to a SNR=1 minimum detection limit MDL = 0.32 ppm. The linear fit between area underneath the QEPAS signal versus N_2O concentration yields a slope of 0.16 mV·cm^{-1}/ppm and an intercept of 5.8 mV·cm^{-1}, as shown in the inset in Fig. 4.17, consistent with the area of 2.6 mV·cm^{-1} measured underneath the curve of the QEPAS background noise level in pure N_2. The calculated R-squared value equals 0.998.

The QEPAS sensor MDL can be further improved by increasing the lock-in integration time. An Allan-Werle deviation analysis was performed (see Appendix), predicting the trend of the 1-σ QEPAS signal fluctuations as a function of the lock-in integration time. Based on the proportionality between σ_A and the 1-σ noise, a plot of the MDL as a function of the lock-in integration time was obtained, as shown in Fig. 4.18.

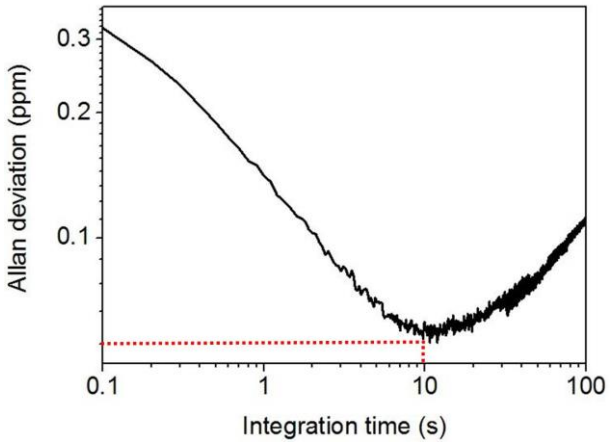

Figure 4.18 Allan-Werle deviation plot of the QEPAS signal in ppm units as a function of the lock-in integration time. For a 10 s integration time, a minimum detection limit of ~60 ppb was achieved (red dashed line).

By averaging the QEPAS signal over longer times, the detection sensitivity decreases to ~60 part-per-billion (ppb) for an integration time of 10 s, thus allowing detection of atmospheric levels (>300 ppb) of N_2O [22].

4.3.2 Methane C-H bonds bending vibrations detection

In section 4.3.1 an accurate reconstruction of the P- and R-branches of nitrous oxide was demonstrated by employing a monolithic array of QCLs as the light source of the QEPAS sensor. Compared to N_2O, methane exhibits a more complex spectrum in the 1190 cm^{-1} - 1340 cm^{-1} spectral range, consisting in an absorption band composed by many overlapping peaks, not equally separated, due to the C-H bonds bending vibrations. The simulation of the methane absorption spectrum obtained by using HITRAN database is shown in Fig. 4.19.

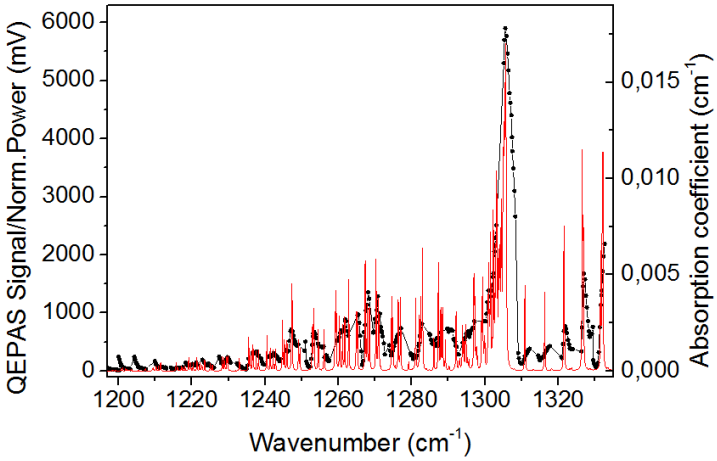

Figure 4.19 Comparison between the normalized QEPAS signals scaled to the normalized optical power, measured for a concentration of 1000ppm CH_4:N_2 while tuning the operating temperature of the QCL array (black dots, left y-axis) and the spectrum simulated at the same CH_4 concentration by using the HITRAN database (red solid line, right y-axis).

The procedure for methane detection is similar to the one illustrated for nitrous oxide. The QEPAS signal of 1000 ppm CH_4:N_2 was measured while tuning the operating temperature of each QCL from 15°C to 50°C in 3°C steps and switching the lasers in sequence. The acquired QEPAS signals, scaled to the QCL array normalized optical power curve, are plotted in Fig. 4.19 (black dots) and compared with the simulated

absorption spectrum. The fine wavelength tuning shows a smooth reconstruction of the peak appearing at 1305.6 cm^{-1} as well as the merging of absorption lines in clustered bands. In the 1260-1280 cm^{-1} and in the 1310-1330 cm^{-1} range, the QEPAS spectrum matches the trend of the simulated one, with peaks and drops corresponding to the irregularly jagged spectrum simulated by using HITRAN database. Compared with the simulation, lower intensity peaks are measured, due to a QEPAS scan resolution (0.27 cm^{-1}, as resulting from the 3°C operating temperature tuning) lower than the separation between adjacent absorption lines, not allowing a perfect match between the laser emission and the methane absorption wavelengths. However, the acquired signal, as the convolution between the gas absorption spectrum and laser emission spectrum, well reproduces the shape of the spectrum shown in Fig. 4.19.

A fast QCL switching mode was successively performed, by operating all devices at a fixed temperature set at 25°C and switching the lasers in sequence. The acquired QEPAS signals have been scaled by the corresponding measured QCL array normalized optical power curve and are plotted in Fig. 4.20 (black squares). As expected, the spectrum does not exhibit a fine structure, but it follows well the envelope of the simulated absorption features shown in Fig. 4.20. The spectrum envelope shape is thus preserved, making methane absorption features recognizable by the described QEPAS-based sensor employing a QCL array operated in fast switching mode.

A sensor calibration was performed by diluting methane with pure nitrogen and calculating the area underneath the QEPAS signal curve as a function of the CH_4:N_2 concentration. Methane QEPAS spectra acquired for 400ppm, 600ppm, 800ppm and 1000ppm CH_4:N_2 in fast switching mode are plotted in Fig. 4.20.

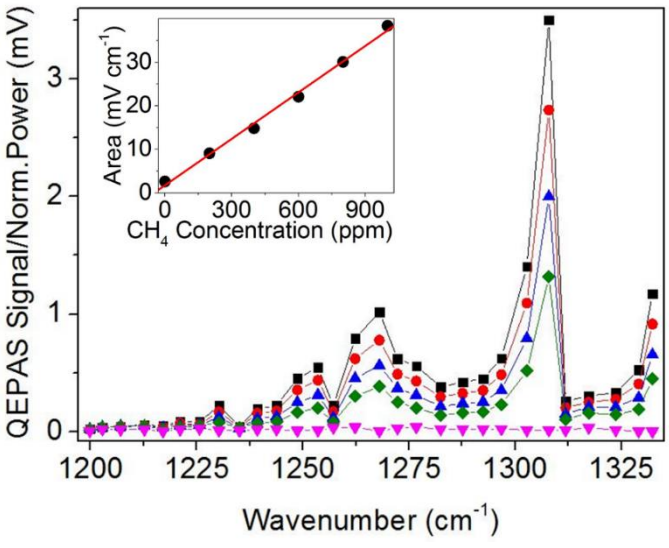

Figure 4.20 1000ppm (black squares), 800ppm (red dots), 600ppm (blue triangles) and 400ppm (green diamonds) CH_4 QEPAS signal normalized by the laser optical power, plotted as a function of the laser peak wavenumber. The operating temperature of the QCL array was fixed at 25°C. The QEPAS signal measured for pure N_2 (pink triangles) is also reported. Solid lines are visual guides. Inset: Area underneath the QEPAS spectrum in $mV \cdot cm^{-1}$ units measured for each CH_4 concentration (black dots) and the corresponding best linear fit (red line).

The linear fit of the area under the QEPAS spectrum as a function of the methane concentration is shown in Fig. 4.20, with a slope of 0.036 $mV \cdot cm^{-1}$/ppm, an intercept of 1.74 $mV \cdot cm^{-1}$ and a R-squared value equal to 0.998.

For a methane concentration of 200 ppm in nitrogen, a total area A of 7.84 $mV \cdot cm^{-1}$ was measured, resulting in an A/σ_A=156.8, where σ_A= 0.05 $mV \cdot cm^{-1}$ was calculated in Section 4.3.1. The methane minimum detection limit is thus 1.27 ppm. Allan-Werle deviation analysis performed in Section 4.3.1, predicting the trend of the 1-σ QEPAS signal fluctuations as a function of the lock-in integration time, estimates a methane MDL of 220 ppb, for a lock-in integration time of 10 s.

References

[1] G. Herzberg, Molecular spectra and molecular structure, Read Books Ltd., vol. 1, 2016.

[2] See http://www.hitran.org/

[3] J.G. Speight, The Chemistry and Technology of Petroleum, CRC Press, Boca Raton, 2014.

[4] M. Schoell, Multiple origins of methane in the Earth, Chem. Geol. 71, 1-3 (1988) 1-10.

[5] M.H. Saberi, and A.R. Rabbani, Origin of natural gases in the Permo-Triassic reservoirs of the Coastal Fars and Iranian sector of the Persian Gulf, J. Nat. Gas Sci. Eng. 26 (2015) 558-569.

[6] F.S. Kinnaman, D.L. Valentine, and S.C. Tyler, Carbon and hydrogen isotope fractionation associated with the aerobic microbial oxidation of methane, ethane, propane and butane, Geochimica et Cosmochimica acta 71, 2 (2007) 271-283.

[7] P. Daukantas, Air-quality monitoring in the mid-infrared, Op. Photonics News 26 (2015) 26.

[8] G. Myhre, D. Shindell, F.M., Bréon, W. Collins, J. Fuglestvedt, J. Huang, D. Koch, J.F. Lamarque, D. Lee, B. Mendoza, and T. Nakajima, Anthropogenic and natural radiative forcing, Climate change 423 (2013) 658.

[9] Ozone Secretariat, The Montreal protocol on substances that deplete the ozone layer (United Nations Environment Programme, Nairobi, Kenya) (2000).

[10] L. Dong, F.K. Tittel, C. Li, N.P. Sanchez, H. Wu, C. Zheng, Y. Yu, A. Sampaolo, R.J. Griffin, Compact TDLAS based sensor design using interband cascade lasers for mid-IR trace gas sensing, Opt. Exp. 24 (2016) A528.

[11] M. Jahjah, W. Kiang, N.P. Sanchez, W. Ren, P. Patimisco, V. Spagnolo, S.C. Herndon, R.J. Griffin, F.K. Tittel, Atmospheric CH_4 and N_2O measurements near Greater Houston area landfills using QCL-based QEPAS sensor system during DISCOVERY-AQ 2013, Opt. Lett. 39 (2014) 957.

[12] P. Patimisco, A. Sampaolo, Y. Bidaux, A. Bismuto, M. Schott, J. Jiang, A. Muller, J. Faist, F.K. Tittel, V. Spagnolo, Purely wavelength- and amplitude-modulated quartz-enhanced photoacoustic spectroscopy, Op. Exp. 24 (2016) 25943.

[13] I.T. Sorokina, K.L. Vodopyanov, Solid-State Mid-Infrared Laser Sources, Springer-Verlag, Berlin Heidelberg, 2003.

[14] A. Hugi, R. Maulini, J.Faist, External cavity quantum cascade laser, Semicond Sci Tech 25, 083001 (2010).

[15] A. Hugi, R. Terazzi, Y. Bonetti, A. Wittmann, M. Fischer, M. Beck, J. Faist and E. Gini, External cavity quantum cascade laser tunable from 7.6 to 11.4 μm, Appl. Phys. Lett. 95 (2009) 061103.

[16] D. Caffey, T. Day, C.S. Kim, M. Kim, I. Vurgaftman, W.W. Bewley, J.R. Lindle, C.L. Canedy, J. Abell, J.R. Meyer, Performance characteristics of a continuous-wave compact widely tunable external cavity interband cascade lasers, Opt. Express 18 (2010)15691.

[17] T. Tsai and G. Wysocki, External-cavity quantum cascade lasers with fast wavelength scanning, Appl. Phys. B 100 (2010) 243.

[18] B. G. Lee, M.A. Belkin, R. Audet, J. MacArthur, L. Diehl, C. Pflügl, F. Capasso, D.C. Oakley, D. Chapman, A. Napoleone, D. Bour, S. Corzine, G. Höfler and J., Faist, Widely tunable single-mode quantum cascade laser source for mid-infrared spectroscopy, Appl. Phys. Lett. 91 (2007) 231101.

[19] M.F. Witinski, R. Blanchard, C. Pfluegl, L. Diehl, B. Li, K. Krishnamurthy, B.C. Pein, M. Azimi, P. Chen, G. Ulu, G. Vander Rhodes, C.R. Howle, L. Lee, R.J. Clewes, B. Williams, and D. Vakhshoori, Portable standoff spectrometer for hazard identification using integrated quantum cascade laser arrays from 6.5 to 11 μm, Opt. Express 26 (2018) 12159.

[20] B.G. Lee, M.A. Belkin, C. Pflugl, L. Diehl, H.A. Zhang, R.M. Audet, J. MacArthur, D.P. Bour, S.W. Corzine, G.E. Hofler, and F. Capasso, DFB quantum cascade laser arrays, IEEE J. Quantum Electron. 45, 5 (2009) 554-565.

[21] M. Giglio, P. Patimisco, A. Sampaolo, A. Zifarelli, R. Blanchard, C. Pfluegl, M.F. Witinski, D. Vakhshoori, F.K. Tittel, and V. Spagnolo, Nitrous oxide quartz-enhanced photoacoustic detection

employing a broadband distributed-feedback quantum cascade laser array, Appl. Phys. Lett. 113, 17 (2018) 171101.

[22] See https://www.epa.gov/climate-indicators/climate-change-indicators-atmospheric-concentrations-greenhouse-gases

Conclusions and further perspectives

In this thesis, novel developments to the state-of-the-art of quartz-enhanced photoacoustic spectroscopy (QEPAS) have been described.

The low spatial quality of commercial lasers beam can dramatically compromise the sensitivity of a QEPAS sensor. Cylindrical and tapered hollow-core waveguides (HCWs) have been demonstrated to provide single-mode delivery in the mid-infrared spectral range with low propagation losses, by properly selecting the dielectric layer thickness, the bore radius, the fiber length and the focal length of the lens optically coupling the laser with the employed HCW. The beam filtering provided by an HCW with 300 μm bore diameter was exploited in a QEPAS-based leak sensor, enabling high-performance detection of sulphur hexafluoride gas traces, with concentrations down to a few parts-per-trillion in volume.

Since its first demonstration for over than ten years, QEPAS employed as acoustic waves detector the commercial 32 kHz quartz tuning fork (QTF), devoted to timing applications. A study on the dependence of the QTF resonance frequency, quality factor and electrical resistance on the prongs geometrical parameters allowed the design of custom QTFs optimized for gas sensing implementation. The large prong spacing (700 μm) and low fundamental mode resonance frequency (<5 kHz) of one of the realized QTFs, namely QTF#5, allowed the extension of QEPAS to THz spectral range, where a methanol absorption line was detected with a NNEA=$3.75 \cdot 10^{-11}$ $cm^{-1}W/Hz^{½}$, which represents a record value for QEPAS trace gas sensing. The design of QTFs with a large prong spacing also paved the way to a novel QEPAS configuration. A spectrophone obtained by acoustically coupling QTF#6 (1mm prong spacing) with a single tube set between the QTF prongs was implemented in the so-called single-tube on-beam QEPAS (SO-QEPAS) configuration. Compared to the dual-tube configuration, the SO-QEPAS allowed the reduction of the spectrophone dimension. The design of QTFs with geometries optimized for gas sensing lead to the development of a T-shaped prongs QTF, namely QTF-S08-T. This QTF was implemented in a sensor for ethylene detection, increasing the signal-to-noise ratio of more than 3 times, respect to a custom QTF with standard-geometry prongs.

The even rising interest on broadband absorbers detection lead to the development of two QEPAS-based sensors, for hydrocarbons and greenhouse gases detection,

respectively. The hydrocarbons sensor employed a single interband cascade laser as light source emitting in the spectral range 3.342-3.349 μm, where absorption lines of methane, ethane and propane fall, exhibiting both resolved and merged spectral features. Detection levels in the part-per billion concentration range for methane and ethane and a few parts per million for propane were achieved. Measurements at both low and atmospheric pressures were carried out for mixtures simulating typical downhole hydrocarbon concentrations. The obtained results pave the way to the development of a prototype to guide oil exploration and production in petrochemical industry. The greenhouse gases detector employed a monolithic distributed feedback-quantum cascade laser array, emitting in the 1190-1340 cm^{-1} spectral range. The QEPAS signals of P- and R-branches of nitrous oxide and several broad features of methane were acquired by tuning the operating temperature of the QCLs and switching of individual devices in sequence. This study showed the capability and the versatility of QEPAS technique for the detection of broadband absorbers. The employment of the monolithic array of QCLs made QEPAS a powerful tool to detect absorbers characterized by broad structures, to examine multiple gases and the ratios of various components in a mixture with a single system and to recognize the presence of contaminant gases altering the spectrum shape and intensity of the primary broadband absorber gas.

Appendix
Allan-Werle deviation analysis for long term stability investigation of QEPAS sensors

Sensitivity represents a crucial figure of merit in any sensor system, and for QEPAS corresponds to the gas concentration providing a signal equivalent to the noise (signal-to-noise ratio SNR=1).

The sensitivity of a QEPAS sensor can be improved by further averaging its signal. From a theoretical point of view, the signal from a perfectly stable system could be infinitely averaged, thus leading to extremely sensitive measurements. However, an optical sensor operating in the field is a limited stable system. There exists an optimum integration time at which the detection limit reaches a minimum value. At longer averaging time, drift effects emerge and the sensor performance deteriorates. The optimum integration time is both application– and installation– specific for a given sensor instrument. The Allan-Werle variance analysis allows the determination of how long optical sensor signals can be averaged in order to increase the detection sensitivity, and before noise sources like laser instability, temperature and mechanical drifts, as well as when moving fringes begin to dominate. This technique was initially developed by Allan in 1966 to study the frequency stability of precision oscillators [1]. In 1993, Werle applied the Allan variance to signal averaging in tunable laser absorption spectroscopy (TDLAS) instrumentation [2].

To determine the long-term stability of a sensor system an Allan-Werle variance analysis is mandatory. This analysis allows investigating drifts and establishing the sensor signal averaging limits. Given a set of M time-series data acquired with an integration time τ, its Allan-Werle variance $\sigma_y^2(\tau)$ is defined as:

$$\sigma_y^2(\tau) = \frac{1}{M}\sum_{k=1}^{M}\frac{1}{2}\left(y_{k+1} - y_k\right)^2 \qquad \text{(A.1)}$$

where y_k is the kth-data averaged over an integration time τ, y_{k+1}-y_k is the difference between adjacent values of y_k, and M is the total number of data, usually of the order of

10^3-10^4. To estimate how $\sigma_y^2(\tau)$ changes with the integration time, a LabView-based code was implemented. Starting from the set of M data acquired at an integration time τ_0 and assuming that there is no dead time between adjacent measurements, the software averages the values for y_1 and y_2 and obtains a new y_1 value averaged over $2\tau_0$. Subsequently, this routine averages values for y_3 and y_4 and changes them as a new value y_2 averaged over $2\tau_0$ and finally applies Eq. (A.1) to determine $\sigma_y^2(2\tau_0)$. The software repeats this process for other integer multiples m of τ_0 and at the end of the processing, it generates values for $\sigma_y^2(m\tau_0)$ as a function of $m\tau_0$. Thus, to perform an Allan-Werle variance σ_y^2 analysis, all the data subsets have to be stacked together and treated as a single uninterrupted time sequence. Usually the Allan-Werle deviation σ_y is shown instead of the variance and expressed in terms of absorption coefficient or absorbing gas concentration, thus determining the minimum detectable concentration as a function of the integration time.

As discussed in Section 3.1.1, a QTF can be modeled as an RLC circuit [3]. The electrical response of the QTF is measured by means of a trans-impedance amplifier with a gain resistor R_g = 10 MΩ. The root mean square of the QTF thermal (Johnson) noise, is expressed as:

$$\sigma_{thermal} = R_g \sqrt{\frac{2k_B T}{\pi R \tau}}, \tag{A.2}$$

where k_B is the Boltzmann constant, T = 298 K is the QTF temperature and τ is the integration time. R_g also introduces noise, which is several times lower than the thermal QTF noise and can be neglected for typical values of R in the range 10-100 kΩ, as in QEPAS case. Thermal noise determines the minimum detection limit of the QEPAS sensor. If the QTF thermal noise is the dominant noise source, the Allan-Werle deviation closely follows a $1/\sqrt{t}$ dependence (see Eq. (A.2)), for the entire duration of the concentration measurements. Usually the Allan-Werle plot of the QTF signal follows the dark-noise trend till a turnover point at an optimum integration time τ_{opt} and increases for longer integration times. Such a drift is ascribed to long-term laser instabilities [4]. Therefore, at $\tau=\tau_{opt}$ the signal standard deviation reaches a minimum value, corresponding to the minimum detection value. For $\tau>\tau_{opt}$ the QEPAS sensitivity starts to deteriorate, as the laser source-related power fluctuations dominate the QTF noise signal.

References

[1] D. W. Allan, Statistics of atomic frequency standards, Proc. IEEE, 54, 2 (1966) 221–230.

[2] P. Werle, R. Miicke, and F. Slemr, The limits of signal averaging in atmospheric trace-gas monitoring by tunable diode-laser absorption spectroscopy (TDLAS), Appl. Phys. B, 57 (1993) 131–139.

[3] P. Patimisco, G. Scamarcio, F. K. Tittel, and V. Spagnolo, Quartz-enhanced photoacoustic spectroscopy: A Review, Sensors, 14 (2014) 6165–6206.

[4] M. Giglio, P. Patimisco, A. Sampaolo, G. Scamarcio, F. K. Tittel, and V. Spagnolo, Allan Deviation Plot as a Tool for Quartz-Enhanced Photoacoustic Sensors Noise Analysis, 63, 4 (2016) 555.